

**METAL-INSULATOR-METAL DIODES FOR AMBIENT  
HEAT HARVESTING WITH RECTENNAS**

by

**AMINA BELKADI DOSTART**

B.S., Khalifa University, 2014

M.S., University of Colorado Boulder, 2017

A thesis submitted to the  
Faculty of the Graduate School of the  
University of Colorado in partial fulfillment  
of the requirements for the degree of  
Doctor of Philosophy  
Department of Electrical, Computer, and Energy Engineering

2020

This thesis entitled:  
Metal-Insulator-Metal Diodes for Ambient Heat Harvesting with Rectennas  
written by Amina Belkadi Dostart  
has been approved for the Department of Electrical, Computer, and Energy Engineering

---

Prof. Garret Moddel

---

Prof. Wounjhang Park

Date \_\_\_\_\_

The final copy of this thesis has been examined by the signatories, and we find that both the content and the form meet acceptable presentation standards of scholarly work in the above mentioned discipline.

Belkadi Dostart, Amina (Ph.D., Electrical, Computer, and Energy Engineering)

Metal-Insulator-Metal Diodes for Ambient Heat Harvesting with Rectennas

Thesis directed by Prof. Garret Moddel

Metal-insulator-metal (MIM) diodes are high-speed, tunneling-based devices used to generate DC current from optical frequency electromagnetic radiation coupled to them through an antenna. An attractive application for these antenna-coupled diodes, known as rectennas, is ambient heat harvesting via radiative cooling. The blackbody radiation spectrum of objects at room temperature peaks in mid-terahertz frequencies (10 - 15 THz), far above the cutoff frequency of traditional diodes, making MIM-based rectennas good candidates for ambient heat harvesting. Efficient thermal-to-electrical energy conversion using MIM diodes is limited by low rectification efficiency (resulting from low asymmetry) at low voltages where they self-bias under illumination, as well as poor coupling efficiency to the antenna due to their capacitive nature.

This work focuses on designing, fabricating, and characterizing ultra-high-speed double-insulator MIM (MI<sup>2</sup>M) diodes optimized for incoming signals with low power density, such as ambient heat. It begins by using the semi-classical theory of photon-assisted tunneling to calculate the thermal noise rectification efficiency of a fabricated MI<sup>2</sup>M diode. It then discusses an erroneous method used to calculate voltage division across oxides of multi-insulator MIM diodes and proposes an improved method. The drastic change between DC and high frequency voltage division has resulted in large differences between predicted and measured MI<sup>2</sup>M diode characteristics. These differences are avoided by the technique introduced here, enabling better diode designs with higher rectification efficiencies.

Two methods to increase coupling efficiency are analyzed and experimentally demonstrated: resonant tunneling in MI<sup>2</sup>M diodes and an antenna transmission line compensation structure. With resonant tunneling, a reduction in resistance is observed with an increase in asymmetry, enabling high coupling and rectification efficiencies. Simulations and experimental measurements of resonant

tunneling effects in MI<sup>2</sup>M diodes are presented. Similarly, the addition of a transmission line compensation structure modifies the antenna impedance seen by the diode at terahertz frequencies to enhance coupling efficiency by over an order of magnitude.

The improvements to coupling efficiency are used to experimentally demonstrate the basic principle of thermal-to-electrical energy conversion using an MI<sup>2</sup>M diode-based optical rectenna. Under practical operating conditions, this technology has the potential to exceed similar diode technologies for harvesting ambient heat via radiative cooling. The results of this work open a path towards ambient nighttime heat harvesting as a companion technology to solar cells, leading to battery-less green energy.

## DEDICATION

Dedicated to my grandmothers, Yamina and Kheira, and my parents, Amel and Bedredine, who taught me the power of patience and education, and to my daughter Talia, who I hope to teach the same lessons to.

## ACKNOWLEDGEMENTS

A PhD is a challenging and life-changing experience that would not be possible without the support and guidance of many people. First, I would like to thank my thesis advisor, Garret Moddel, for his guidance, enthusiasm and immense knowledge. He has taught me, both consciously and unconsciously, how good scientific research is done. I am thankful for the excellent example he has provided as a successful researcher, professor, and parent. I am also very grateful to the members of my PhD committee, Professors Chuck Rogers, Sean Shaheen, Taylor Barton, and Won Park for their brilliant comments and suggestions.

The members of the quantum engineering lab have contributed immensely to my personal and professional time at Boulder. Dave Doroski, Brad Pelz, Ayendra Weerakkody and John Stearns have been a source of friendship as well as good advice and collaboration. Other past and present group members that I have had the pleasure to work with or alongside are Micheal Cromar, Brad Herner, Saumil Joshi, Kavan Ganapathy and Kaitlin Coleman. I gratefully acknowledge the funding sources that made my PhD work possible. I was funded by Redwave Energy Inc., KAUST University and Lockheed Martin for my first four years and was honored to be a GAANN Graduate Fellow for the last year.

A special thanks goes to my family and friends. Words cannot express how grateful I am to my mother and father, Amel and Bedredine, for all the sacrifices they've made to get me here. I thank my siblings, Roumaissa, Dhyaa and Inas, for constantly making me laugh. I thank my parents-in-law, Pam and David, for their continuous love and endless support. I thank my undergraduate advisor, Professor Abdel Isakovic, for encouraging me to pursue a doctoral degree and sparking my interest in research. Special thanks to Simeng, Stephanie, Maisam, Tasneem, Amany, Tamador and Namareq for making this journey fun and being there every step of the way. And most of all, I thank my loving, supportive, encouraging and patient husband, Nathan, without whom I would not have been able to do this, and our little Talia, who brightens our lives.

# CONTENTS

CHAPTER	
<b>1</b>	<b>INTRODUCTION</b> <span style="float: right;"><b>1</b></span>
1.1	Waste heat harvesting . . . . . 1
1.2	Rectennas . . . . . 3
1.3	Metal-insulator-metal diodes . . . . . 3
1.3.1	Diode challenges for high frequency operation . . . . . 5
1.4	Thesis organization . . . . . 7
<b>2</b>	<b>THERMAL-TO-ELECTRICAL ENERGY CONVERSION WITH DIODES</b> <span style="float: right;"><b>9</b></span>
2.1	Resistor thermal noise rectification . . . . . 10
2.2	Rectenna efficiency under broadband illumination . . . . . 13
2.2.1	Photon-assisted tunneling . . . . . 16
2.3	Thermal noise rectifier equivalent circuit . . . . . 18
2.4	Thermal noise rectification efficiency with MI <sup>2</sup> M diodes . . . . . 21
2.5	Conclusion . . . . . 22
<b>3</b>	<b>EXPERIMENTAL METHODS</b> <span style="float: right;"><b>24</b></span>
3.1	Germanium shadow mask process . . . . . 25
3.2	Material deposition . . . . . 25
3.3	Diode characterization . . . . . 27
3.3.1	DC measurements . . . . . 27

3.3.2	Optical measurements . . . . .	28
3.4	Conclusion . . . . .	30
<b>4</b>	<b>MI<sup>2</sup>M DIODE ANALYSIS: RESISTIVE AND CAPACITIVE VOLTAGE DIVISION</b>	<b>31</b>
4.1	Introduction . . . . .	31
4.2	Diode fabrication: MIM-1 and MI <sup>2</sup> M-1 . . . . .	33
4.3	DC and high frequency resistance . . . . .	35
4.4	Band diagrams computation . . . . .	38
4.5	Efficiency Calculations . . . . .	40
4.6	High Frequency $I(V)$ . . . . .	42
4.7	Conclusions . . . . .	44
<b>5</b>	<b>DEMONSTRATION OF RESONANT TUNNELING EFFECTS IN METAL-DOUBLE-INSULATOR-METAL (MI<sup>2</sup>M) DIODES</b>	<b>45</b>
5.1	Introduction . . . . .	45
5.2	Breaking the responsivity/resistance trend using resonant tunneling . . . . .	46
5.3	Simulation-based resonant tunneling analysis . . . . .	51
5.3.1	Maintaining the correct thickness ratio . . . . .	53
5.3.2	Transmittance analysis . . . . .	54
5.3.3	Negative differential resistance near zero-bias . . . . .	56
5.4	Rectification enhancement at a wavelength of 10.6 $\mu\text{m}$ . . . . .	56
5.5	Conclusions . . . . .	58
<b>6</b>	<b>COMPENSATION STRUCTURE FOR HIGH RESISTANCE MI<sup>2</sup>M DIODES</b>	<b>60</b>
6.1	Impedance matching with an MIM diode . . . . .	60
6.2	Antenna modeling with HFSS . . . . .	62
6.3	Variable impedance bowtie antenna . . . . .	65
6.4	Expected efficiency enhancement with transmission line . . . . .	67

6.5	MIM diode fabrication . . . . .	70
6.5.1	Diode array design . . . . .	73
6.6	Diode array optical measurements . . . . .	74
6.6.1	Open-circuit voltage polarization dependence . . . . .	74
6.7	MIM diode fabrication - extending transmission line lengths . . . . .	78
6.8	Conclusion . . . . .	83
<b>7</b>	<b>DEMONSTRATION OF AMBIENT HEAT HARVESTING USING OPTICAL RECTEN-</b>	
	<b>NAS</b>	<b>84</b>
7.1	Rectification through radiation . . . . .	84
7.2	Nighttime radiative cooling . . . . .	86
7.3	MIM-based rectenna for rectification through radiation . . . . .	88
7.3.1	Diode staggered array design . . . . .	89
7.3.2	Fabrication process . . . . .	91
7.4	Experimental Setup . . . . .	94
7.5	Results . . . . .	95
7.6	Conclusion . . . . .	98
<b>8</b>	<b>CONCLUSIONS AND FUTURE WORK</b>	<b>99</b>
	<b>BIBLIOGRAPHY</b>	<b>102</b>
	<b>APPENDIX</b>	
<b>A</b>	<b>EXPONENTIAL FITTING AND SIMULATION PARAMETERS</b>	<b>110</b>
A.1	MIM-1 Diode . . . . .	110
A.2	MI <sup>2</sup> M-1 Diode . . . . .	110
A.3	MI <sup>2</sup> M-2 Diode . . . . .	111

A.4 MI <sup>2</sup> M-3 Diode . . . . .	111
A.5 MI <sup>2</sup> M-4 Diode . . . . .	111
A.6 Cosine squared fitting parameters . . . . .	111
<b>B PUBLICATIONS</b>	<b>112</b>

## TABLES

### Table

4.1	MIM-1 and MI <sup>2</sup> M-1 diode properties . . . . .	35
4.2	MIM-1 and MI <sup>2</sup> M-1 optical response values . . . . .	36
4.3	MIM-1 and MI <sup>2</sup> M-1 coupling efficiency calculations . . . . .	41
4.4	MIM-1 and MI <sup>2</sup> M-1 efficiency calculations using power waterfall diagram analysis . .	42
4.5	MIM-1 and MI <sup>2</sup> M-1 efficiency calculations from experimental results . . . . .	42
5.1	MI <sup>2</sup> M-2, MI <sup>2</sup> M-3 and MI <sup>2</sup> M-4 efficiency calculation . . . . .	57
6.1	Antenna impedance simulation results . . . . .	64
6.2	Antenna impedance with varying transmission line length . . . . .	65
6.3	MIM-2 and MI <sup>2</sup> M-5 series equivalent impedance calculations . . . . .	67
6.4	Material deposition conditions . . . . .	71
6.5	Areas of diodes with transmission lines from SEM images . . . . .	71
6.6	Parameters used to calculate total efficiency of fabricated diodes due to thickness variation. . . . .	80
6.7	Measured optical characteristics and calculated efficiency of Ni/NiO/Cr/Au diodes .	81
6.8	Measured optical characteristics and calculated efficiency of Ni/NiO/Al <sub>2</sub> O <sub>3</sub> /Cr/Au diodes . . . . .	82
7.1	Literature survey of radiative cooling energy harvesting with diodes . . . . .	89
7.2	Responsivity and resistance of diode in a staggered design . . . . .	92

A.1	MIM-1 DC $I(V)$ simulation parameters . . . . .	110
A.2	MI <sup>2</sup> M-1 DC $I(V)$ simulation parameters . . . . .	110
A.3	MI <sup>2</sup> M-2 DC $I(V)$ simulation parameters . . . . .	111
A.4	Cosine squared fitting parameters . . . . .	111

## FIGURES

### Figure

1.1 Thermoelectrics figure of merit $ZT$ versus temperature . . . . .	2
1.2 Rectenna diagram . . . . .	4
1.3 MIM diode energy-band profile . . . . .	4
1.4 MIM diode energy-band profile under applied voltage . . . . .	5
1.5 Equivalent-circuit model of the rectenna . . . . .	6
2.1 Blackbody radiation and thermal noise rectifier circuits . . . . .	9
2.2 Classical diode-resistor generator circuit configurations . . . . .	12
2.3 Rectenna detailed balance . . . . .	13
2.4 Rectenna equivalent circuit . . . . .	14
2.5 Broadband illuminated $I(V)$ and conversion efficiency calculation . . . . .	15
2.6 Photon-assisted tunneling in a diode . . . . .	17
2.7 Thermal noise rectifier equivalent circuit . . . . .	19
2.8 Rectification at thermal equilibrium . . . . .	19
2.9 Modified Thermal noise rectifier circuit . . . . .	20
2.10 Thermal noise voltage signal . . . . .	22
2.11 Power conversion efficiency as a function of resistor temperature . . . . .	22
3.1 Device fabrication process . . . . .	24
3.2 Diode fabrication with GSM . . . . .	26

3.3	SEM images of fabricated diodes . . . . .	26
3.4	Current-voltage characteristics and differential resistance and responsivity curves. . .	28
3.5	Optical illumination measurement setup . . . . .	29
4.1	Circuit and band diagrams for voltage division . . . . .	32
4.2	MIM-1 and MI <sup>2</sup> M-1 diode $I(V)$ characteristics and $\beta$ , R and $V_{oc}$ curves . . . . .	34
4.3	MIM and MI <sup>2</sup> M diode simulations . . . . .	37
4.4	DC resistive voltage division . . . . .	38
4.5	Capacitive voltage division . . . . .	39
4.6	Power waterfall diagram analysis . . . . .	40
4.7	MI <sup>2</sup> M-1 diode simulated 28 THz $I(V)$ characteristics . . . . .	43
5.1	Breaking the responsivity/resistance trade-off . . . . .	47
5.2	Measured $\beta_0$ vs. $R_0$ plot of thickness study . . . . .	48
5.3	Measured $\beta_0$ vs. $R_0$ plot of thickness study . . . . .	50
5.4	MI <sup>2</sup> M-2 diode simulation analysis . . . . .	51
5.5	Diode simulation analysis with thickness variations . . . . .	52
5.6	Thickness ratio for resonant tunneling . . . . .	54
5.7	Tunneling probability and band diagrams of MI <sup>2</sup> M diodes . . . . .	55
5.8	MI <sup>2</sup> M-2, MI <sup>2</sup> M-3 and MI <sup>2</sup> M-4 $V_{oc}$ curves . . . . .	57
6.1	Impedance of 200 $\Omega$ MIM diode versus capacitance and RC time constant . . . . .	61
6.2	Simulated GSM antenna . . . . .	62
6.3	Impedance and radiation pattern of simulated bowtie antenna with 24° angle . . . .	63
6.4	Bowtie antenna DC arms . . . . .	64
6.5	Transmission line compensation structure with 24° antenna . . . . .	66
6.6	Transmission line compensation structure with 15° antenna . . . . .	66
6.7	Modified power waterfall diagram . . . . .	67

6.8	Effects of transmission line length on diode characteristics and coupling efficiency . .	69
6.9	Effects of transmission line length on Eq. 6.3 . . . . .	69
6.10	Expected rectenna conversion efficiency enhancement with transmission line length .	70
6.11	Transmission line length SEM Images . . . . .	72
6.12	SEM image of different array designs . . . . .	73
6.13	Antenna area . . . . .	75
6.14	0 and 0.5 $\mu\text{m}$ transmission line array measured open-circuit voltage ( $V_{oc}$ ) . . . . .	76
6.15	The 0 and 2 $\mu\text{m}$ transmission line array measured open circuit voltage ( $V_{oc}$ ). . . . .	76
6.16	Efficiency versus transmission line lengths between 0 and 2.5 $\mu\text{m}$ . . . . .	77
6.17	Efficiency versus transmission line length for Ni/NiO/Cr/Au diode . . . . .	78
6.18	Transmission line length SEM Images . . . . .	79
6.19	Efficiency versus length for different Ni/NiO/Cr/Au diode resistances . . . . .	81
6.20	Efficiency versus length for different Ni/NiO/Al <sub>2</sub> O <sub>3</sub> /Cr/Au diode resistances . . . . .	82
7.1	Radiation transmitted by the atmosphere . . . . .	85
7.2	Radiating power converter . . . . .	85
7.3	Photodiode under negative illumination condition . . . . .	86
7.4	Experimental demonstration of power from negative illumination . . . . .	87
7.5	Staggered array design . . . . .	90
7.6	Staggered diode arrays with 4 $\times$ 4 and 6 $\times$ 6 devices . . . . .	92
7.7	$I(V)$ characteristics and $\beta$ , R curves for staggered array . . . . .	93
7.8	Diagram of the experimental setup . . . . .	94
7.9	Open-circuit voltage and power versus temperature for $T_{rectenna} = 290$ and 300 K .	96
7.10	Radiating rectenna power waterfall diagram . . . . .	97

## CHAPTER 1

### INTRODUCTION

#### 1.1 Waste heat harvesting

A clean energy revolution is taking place across the world. Environmentally clean and renewable energy sources, such as wind and solar, are continuously researched to reduce cost and increase efficiency to one day replace coal and oil (Chu and Majumdar, 2012). Waste heat, defined as heat generated as a by-product of a process, has been explored to a lesser extent compared to other sources. According to the US Environment Protection Agency (EPA), around 30-40 % of energy generated from primary sources in the United States is wasted as heat (Rattner and Garimella, 2011). The difficulty in harvesting waste heat stems from its low-temperature grade ( $< 100^\circ \text{C}$ ) that inhibits exploiting it with common technologies (Aranguren et al., 2017, Pandya et al., 2019). One popular solution for waste heat harvesting is thermoelectrics. Thermoelectrics present an attractive technology due to their ability to produce energy from any temperature difference (Rosi, 1968, DiSalvo, 1999, Bell, 2008, Poudel et al., 2008, Aranguren et al., 2017).

Night harvesting, where waste heat is harvested at night using the temperature difference with outer space, presents an attractive application for thermoelectrics. The power radiated at night to space falls between 150 and to 350  $\text{W/m}^2$  (NASA, 2010). For such an application, the efficiency of thermoelectrics is limited by the relatively low figure-of-merit and the low-temperature differential. Efficiency of a thermoelectric device (Sherman et al., 1960) is calculated as

$$\eta_{TE} = \frac{\Delta T}{T_h} \cdot \frac{\sqrt{1 + ZT} - 1}{\sqrt{1 + ZT} + (T_c/T_h)} \quad (1.1)$$

The figure of merit,  $ZT$ , presents the efficiency of the p-type and n-type materials of the thermoelectric (Bell, 2008). The parameter  $Z$  is the product of electrical conductivity and the square of the Seebeck voltage per unit of temperature, divided by thermal conductivity, and  $T$  is the absolute temperature. To maximize efficiency, it is necessary to have the highest  $ZT$  possible and the highest temperature gradient ( $\Delta T$ ) possible. Because temperature-dependent material properties determine the value of  $Z$ , it is difficult to find materials in nature able to provide the desired  $Z$  over a wide range of temperatures. To increase the total thermoelectric conversion efficiency, two or three different materials are usually combined to produce a high  $Z$  over a wide range of temperatures. Each of the individual materials used to make the combined thermoelectric is chosen to have excellent performance over its temperature exposure range (Bell, 2008). For night harvesting, the hot side ( $T_h$ ) is room temperature (300 K) and the cold side ( $T_c$ ) is the temperature of outer space seen from earth (200 K), resulting in  $\Delta T_{max} = 100$  K. A figure of merit  $ZT = 1$  would result in  $\eta_{TE}$  equal to 6.6%. Materials with figure of merits above 1.5 for temperature gradients of  $100^\circ$  C are difficult to fabricate (Ma et al., 2008, Poudel et al., 2008, Fan et al., 2010, Snyder and Toberer, 2011, Sumithra et al., 2011, Kim et al., 2015). Kim et al. present a Ni-doped MgAgSb thermoelectric device with a measured efficiency close to 6% with  $ZT = 1.2$ , as seen in Fig. 1.1. Despite

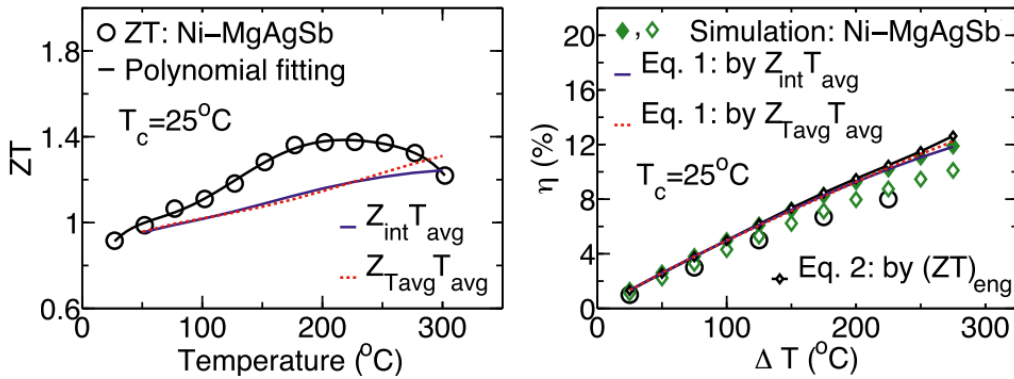


Figure 1.1:  $ZT$  vs.  $T$  of Ni-doped MgAgSb (Kim et al., 2015). For night harvesting,  $\Delta T_{max} = 100^\circ$  C and for  $ZT = 1.2$ , the efficiency is close to 6%.

these promising results, these materials are yet to be demonstrated in a commercial thermoelectric

device. Other technologies for waste-heat harvesting, such as electrochemical systems, are limited to efficiency numbers below 0.5% at temperatures  $< 100^\circ \text{C}$  (Quickenden and Mua, 1995). An alternative approach for night harvesting is to explore optical rectennas as waste-heat rectification. The blackbody spectrum of objects radiating at room temperature ( $\sim 300 \text{K}$ ) peaks in mid terahertz frequencies, making MIM-based rectennas an ideal candidate for waste-heat harvesting, if certain challenges can be circumvented first.

## 1.2 Rectennas

An optical rectenna consists of an ultra-high speed rectifier coupled to a micron-scale antenna. The antenna absorbs incident electromagnetic radiation and converts it to a high frequency current and the diode rectifies the AC current to produce a DC signal (Moddel and Grover, 2013), as presented in Fig. 1.2. Rectennas, originally developed for wireless power transmission (Brown, 1984) and microwave frequency detection (McSpadden and Chang, 1994), have become the focus of numerous research groups for optical detection (Dees, 1966, Fumeaux et al., 1998, Bean et al., 2011, Wang et al., 2015, Auton et al., 2017) and solar energy harvesting (Sarehraz et al., 2005, Moddel and Grover, 2013, Briones et al., 2013, Jayaswal et al., 2018). Although microwave rectennas have been demonstrated to achieve energy conversion efficiencies beyond 85% with semiconductor diodes (Yoo and Chang, 1992), the energy conversion efficiencies of optical rectennas are still very low ( $< 10^{-8}\%$ ) (Jayaswal et al., 2018, Pelz, 2018). The challenge in demonstrating efficient optical rectennas is in designing an ultra-high speed diode with a high rectification efficiency at the desired operating frequency. The femtosecond fast electron tunneling time in metal-insulator-metal (MIM) diodes makes them the current best candidates for optical rectification (Nagae, 1972).

## 1.3 Metal-insulator-metal diodes

Metal-insulator-metal (MIM) tunnel diodes play an important role in many applications, such as high frequency rectification (Moddel and Grover, 2013, Briones et al., 2013), infrared detection (Dees, 1966, Fumeaux et al., 1998, Bean et al., 2011), single electron transistors (Karbasian et al.,

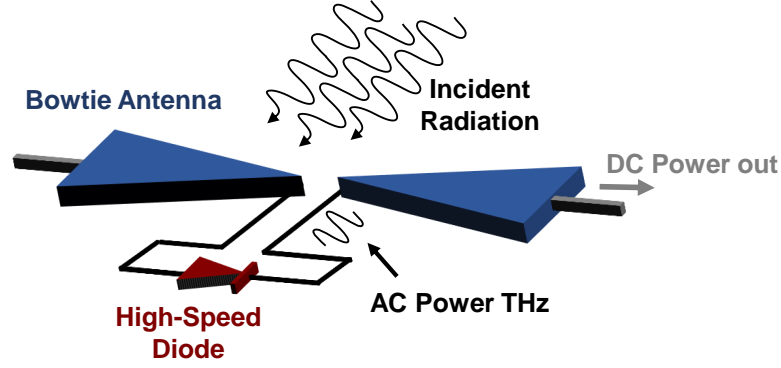


Figure 1.2: Rectenna diagram. The antenna absorbs incident electromagnetic radiation and converts it to a high frequency current and the diode rectifies the AC current to produce a DC signal.

2017, Matsumoto, 1996), resistive random access memory (Niu et al., 2016, Vallée et al., 2009) and matrix addressed displays (Tannas, 1994). MIM diodes for energy harvesting are made out of two different metals, with different work functions, separated by extremely thin insulators ( $< 6$  nm). These diodes work using the fast mechanism of quantum-mechanical tunneling of electrons. The probability of an electron tunneling through the classically forbidden region of an insulator has a nonlinear dependence on the shape of the energy-band profile of the diode (Grover, 2011). The shape is determined by barrier heights ( $\phi$ ), defined as the difference between metal work function ( $\varphi$ ) and insulator electron affinity ( $\chi$ ), and thickness of the insulator ( $t_{ox}$ ), as presented in Fig. 1.3.

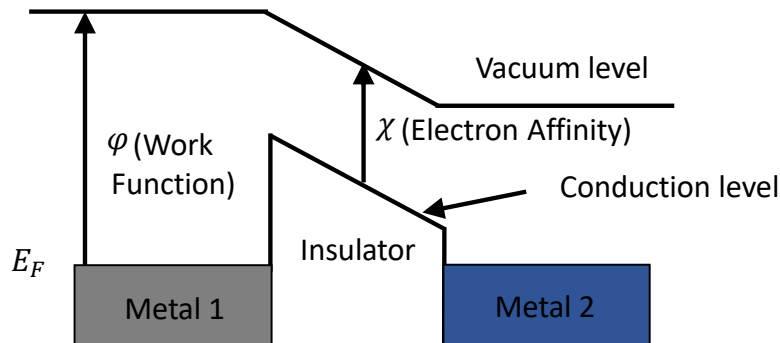


Figure 1.3: MIM diode energy band profile of an MIM diode with band edge energies.

Since applied voltage affects the shape of the energy-band profile and thus the tunneling prob-

ability, tunnel current has a nonlinear dependence on applied voltage. The asymmetric tunneling characteristics result from the different work function values of the two chosen metals. For an applied voltage that is higher than the second barrier height ( $\phi_2$ ), asymmetry (defined as  $I(V^+)/I(V^-)$ ) is determined from the difference in distance the electron tunnels through between positive and negative bias, as well as the height of the vacuum level compared to the tunneling energy. In positive bias, electrons tunnel through a thinner oxide region compared to negative bias, which leads to a higher current in positive bias, as seen in Fig. 1.4. A higher diode asymmetry can be achieved by increasing the number of insulators in the structure to make double-insulator metal-insulator metals (MI<sup>2</sup>M) diodes (Grover and Moddel, 2012). With the added complexity of a second insulator, new diode design challenges arise, especially for optical frequency operation.

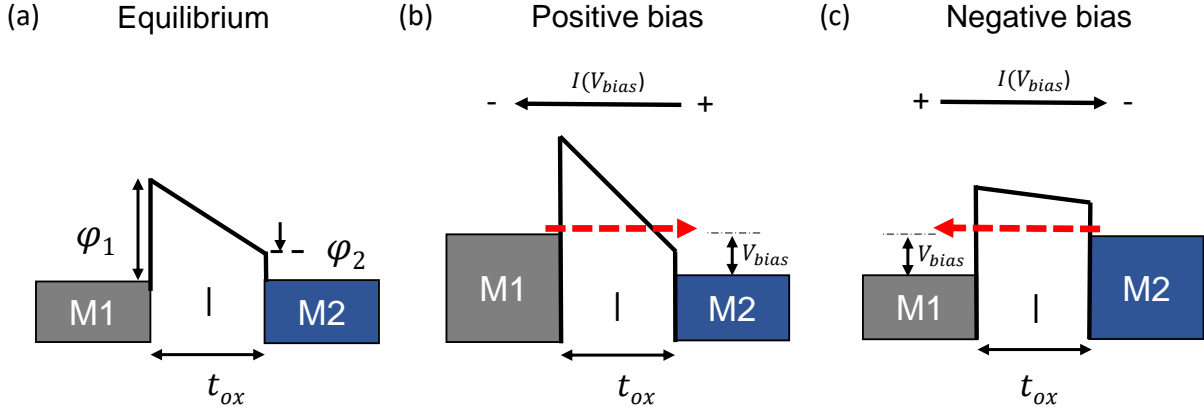


Figure 1.4: MIM diode energy band profile.  $M_1$  and  $M_2$  present the diode dissimilar metals,  $I$  presents the diode insulator,  $t_{ox}$  is oxide thickness, and  $\phi_1$  and  $\phi_2$  are the barrier height formed between  $M1/I$  and  $M2/I$ .

### 1.3.1 Diode challenges for high frequency operation

Diode responsivity ( $\beta$ ) is a measure of current produced in response to incident power, calculated as  $\beta = I''/2I'$  (Cowley and Sorensen, 1966). The idea that a high responsivity is always better is a common misconception about MIM diodes for optical rectennas. High responsivity typically comes at the price of high diode resistance, which has a larger impact on rectenna per-

formance in both cutoff frequency and impedance matching with the antenna. This misconception has driven numerous research paper into designing new diode material and structures that provide high responsivity diodes ( $> 1$  A/W) with high resistance values ( $> 5$  k $\Omega$ ), thus inhibiting their efficient integration in optical rectennas for energy harvesting (Cowell III et al., 2011, Bean et al., 2011, Briones et al., 2013, Alimardani and Conley Jr, 2014, Weerakkody et al., 2015, Arsoy et al., 2016, Mitrovic et al., 2018).

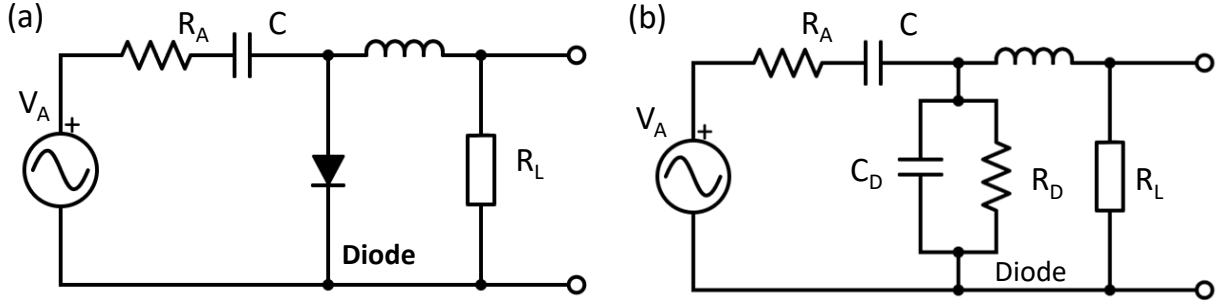


Figure 1.5: (a) Rectenna clamping circuit and (b) small signal circuit model of the rectenna proposed by Sanchez (Sanchez et al., 1978). The antenna is modeled as a voltage source ( $V_A$ ) in series with a resistance ( $R_A$ ) and the MIM diode is modeled as a capacitance ( $C_D$ ) in parallel with a resistance ( $R_D$ ).

The total rectenna efficiency ( $\eta_{rectenna}$ ) can be broken down into three main components (Kale, 1985) computed as

$$\eta_{rectenna} = \eta_a \eta_c \eta_{rect} \quad (1.2)$$

where  $\eta_a$  is the antenna absorption efficiency, i.e., the efficiency of coupling EM radiation to the antenna,  $\eta_{rect}$  is diode rectification efficiency and  $\eta_c$  is the coupling efficiency between the antenna and the diode. The  $\eta_a$  depends on the material properties and antenna design. Rectification efficiency  $\eta_{rect}$  is directly proportional to diode responsivity. The coupling efficiency  $\eta_c$  presents the ratio of AC power delivered to the diode to the power absorbed by the antenna, computed following the circuit diagram in Fig. 1.5 developed by Sanchez (Sanchez et al., 1978). The simplified coupling efficiency between a diode and an antenna, for a diode without capacitance, can be calculated as

$$\eta_c^{simplified} = \frac{4R_A R_D}{(R_A + R_D)^2} \quad (1.3)$$

where  $R_A$  is antenna impedance and  $R_D$  is diode impedance. Antenna impedance is typically on the order of a few hundred ohms at terahertz frequencies (Fumeaux et al., 1998, Pelz, 2018, Jayaswal et al., 2018). A very high responsivity diode (5 A/W) with a 10 k $\Omega$  resistance would be almost useless as 96% of the total power is lost due to the impedance mismatch. For energy harvesting applications where MIM diodes operate as rectifiers, the diode capacitance ( $C_D$ ) and resistance ( $R_D$ ) determine the maximum operation frequency  $f_c = 1/(2\pi RC)$ . This modifies the coupling efficiency to include frequency-dependent diode capacitance ( $C$ ) such that

$$\eta_c = \frac{4R_A R_D}{(R_A + R_D)^2 + (R_A R_D \omega C_D)^2} \quad (1.4)$$

This equation assumes the antenna reactance is negligible compared to the diode reactance, which is not always the case at high frequency ( $> 1$  terahertz) and can reduce the coupling efficiency by a factor of 10 or more. A high rectenna efficiency would require a low resistance ( $< 1$  k $\Omega$ ) and high responsivity ( $> 2$  A/W) diode or a high resistance antenna ( $\sim 1$  k $\Omega$ ).

MIM diodes suffer from extremely low rectification efficiencies ( $\eta_{rect} = 10^{-10}$ ) at high frequency. Diodes measured at 10.6  $\mu\text{m}$  have not exceeded a rectification efficiency of  $\sim 0.01\%$  (Pelz, 2018, Jayaswal et al., 2018). The rest of the losses are due to the  $10^{-2}$  antenna absorption loss and the  $10^{-4}$  coupling efficiency loss. One of the crucial problems in designing MIM diodes for optical rectification is the poor understanding of material properties at high frequency, which leads to the poor modeling of high frequency behaviors. This has led to a difficulty in fabricating MIM diodes that have the best modeled characteristics.

## 1.4 Thesis organization

I will begin in chapter 2 by presenting the thermal-to-electrical energy conversion with diodes. I apply the well developed theory of photon assisted tunneling (PAT) for optical rectennas to calculate the efficiency of MIM diodes rectifying thermal noise. In chapter 3, I present the experimental methods used through the course of this thesis work, from fabrication to diode characterization. The main challenges for a high efficiency waste-heat harvesting system are the diode's rectification

efficiency and the impedance matching between antenna and diode. One challenge in improving rectification efficiency is the difficulty of fabricating MIM diodes that have the best modeled characteristics from simulation. In chapter 4, I present the error in diode characteristics calculation in DC through the wrong use of capacitive voltage division to determine the shape of the band lineup. This is the main reason fabricated diodes have not been able to match simulated diode. Another challenge in improving rectification efficiency is the responsivity/resistance trade-off where high responsivity diode, which would increase rectification efficiency, come at the price of high responsivity that lowers coupling efficiency to low resistance antennas. In chapter 5, I present resonant tunneling as a solution to reduce resistance while maintaining the high responsivity of diodes. In chapter 6, I discuss improving coupling efficiency using a transmission line compensation structure. The diode and antenna improvements were then used to demonstrate waste heat harvesting using MIM diode and radiative cooling in a rectenna configuration, as discussed in chapter 7. I conclude in chapter 8 with the ramifications of this work and suggestions for future work.

## CHAPTER 2

### THERMAL-TO-ELECTRICAL ENERGY CONVERSION WITH DIODES

A rectenna can be modeled with a hot resistor in place of the antenna. This is due to the fact that an ideal broadband rectenna rectifying blackbody radiation generates voltages with the same power spectral density as thermal noise across a hot resistor (Oliver, 1965). These thermal fluctuations (Johnson-Nyquist noise) across the resistor are simply blackbody radiation of a single mode. This allows for the modeling of a rectenna as a resistor connected to a rectifier, as shown in Fig. 2.1, and the use of optical rectenna circuitry and concepts to study thermal noise rectification.

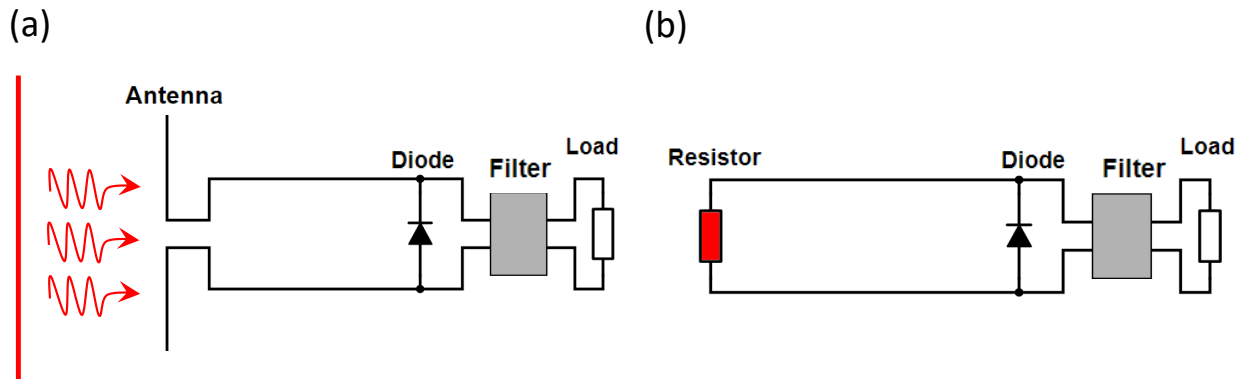


Figure 2.1: Blackbody radiation and thermal noise rectifier circuits. (a) Typical rectenna circuit absorbing blackbody radiation through an antenna for rectification at the diode. (b) Equivalent circuit where the radiation-absorbing antenna has been replaced with a resistor generating Johnson-Nyquist noise and using a high-speed diode for rectification. Both circuits include a low pass filter and a load.

In this chapter, I analytically evaluate the energy conversion process of diodes rectifying radiation from a hot body using a resistor-based thermal noise rectification model. The peak

frequency in a resistor noise spectrum at ambient temperatures and above is  $>15$  THz, which requires an ultra-high-speed diode for rectification and a quantum-based theory to describe the rectification process. I use the analyses developed by Joshi (Joshi and Moddel, 2013) and Grover (Grover et al., 2013) to calculate thermal noise rectification efficiency of an MIM diode using measured  $I(V)$  characteristics and photon-assisted tunneling (PAT) theory.

## 2.1 Resistor thermal noise rectification

Resistor thermal noise produces random temporal voltage/current oscillations which, in principle, can be rectified for thermal energy harvesting. In 1928, Nyquist presented the idea of power flow between two resistors, each of resistance  $R$ , at different temperatures connected by a long, non-dissipative transmission line (Nyquist, 1928). Nyquist described the modes of vibration present in a transmission line connecting the two resistors as random fluctuations in voltage resulting from thermal agitation of electrons, known as Johnson noise. The average power transferred from each resistor to the line within a narrow band of frequencies,  $dv$ , was calculated as  $k_B T dv$ , where  $k_B$  is Boltzmann's constant. At low frequencies, the mean thermal energy contained in each electromagnetic mode in the transmission line is  $k_B T$  and its mean-squared noise voltage  $E_v^2$  within a narrow band of frequencies is expressed as  $E_v^2 dv = 4Rk_B T dv$ . Similarly, for an energy per degree of freedom of  $h\nu/(e^{h\nu/k_B T} - 1)$ ,  $E_v^2$  is expressed as

$$E_v^2 dv = 4Rv \frac{h\nu dv}{e^{h\nu/k_B T} - 1} \quad (2.1)$$

and the total thermal noise power available from a resistor, over the full range of frequencies, is

$$P = \int_0^\infty \frac{E_v^2}{4Rv} dv = \int_0^\infty \frac{h\nu}{e^{h\nu/k_B T} - 1} dv = 2 \frac{(k_B T)^2}{h} \int_0^\infty \frac{\alpha}{e^\alpha - 1} d\alpha = \frac{(k_B T)^2}{h} \frac{\pi}{6} \text{ W}. \quad (2.2)$$

The power ( $P$ ) represents the rate at which the resistor would cool if it loses heat only through electromagnetic radiation over a matched transmission line to a load at  $T = 0$  (Oliver, 1965), and is independent of the resistance value. For two matched resistances ( $R_1$  and  $R_2$ ) at the same temperature,  $R_1$  sends its power down the transmission line to be dissipated at  $R_2$ . The same

process occurs with  $R_2$ . When  $R_1$  is at a lower temperature than  $R_2$ , the power sent from  $R_2$  to be dissipated at  $R_1$  is greater than the reverse situation, resulting in power transfer between the two resistors.

Thermally fluctuating voltages/current associated with resistor Johnson-Nyquist noise can be rectified by a diode and converted to DC power if the system is brought out of thermal equilibrium (Pan et al., 2014). This idea is not new; in 1950, Brillouin proposed the concept of diodes rectifying random noise oscillations produced in a resistor to generate a DC current (Brillouin, 1950). Feynman's classical mechanical ratchet and pawl engine was also later linked to a diode driven by Johnson-Nyquist noise (Magnasco and Stolovitzky, 1998). Both systems appear to break the second law of thermodynamics on the macroscopic scale, but upon closer examination require a temperature gradient to generate power in agreement with the second law. Sokolov developed a more accurate theoretical model based on a master-equation approach and showed that power can be generated from the thermal fluctuations in a hot resistor with a cold diode (Sokolov, 1998, Pan et al., 2014).

The diode-resistor generator circuit has been extensively studied in literature as a model to explore thermodynamics limits of a nonlinear system. Byrnes et al. (Byrnes et al., 2014) summarize those results by presenting three configuration of the classical diode-resistor generator circuit: in thermal equilibrium (Fig. 2.2 A), in the conventional rectifier configuration (Fig. 2.2 B) and in a new configuration with a hot diode (Fig. 2.2 C). In thermal equilibrium where the diode and resistor are at the same temperature, no net flow of energy or open-circuit voltage are measured. When the resistor temperature ( $T_R$ ) is higher than the diode temperature ( $T_D$ ), the resistor's thermal fluctuations (AC noise) are rectified by the diode and produce a DC signal. Similarly, when the diode is hot ( $T_R < T_D$ ), the thermal fluctuations of the diode are rectified and DC power is produced. For a semiconductor diode, rectification of a hot resistor using a cold diode results in open-circuit voltage in the opposite direction of rectification using a hot diode. The capacitance is negatively charged when current flows from the resistor to the diode and positively charged when electrons flow in the other direction, as seen in Fig. 2.2 (Byrnes et al., 2014). Realizing such a

system requires diodes with high rectification efficiencies at low voltages, good thermal isolation between the diode and resistor, and low power loss in the transmission line.

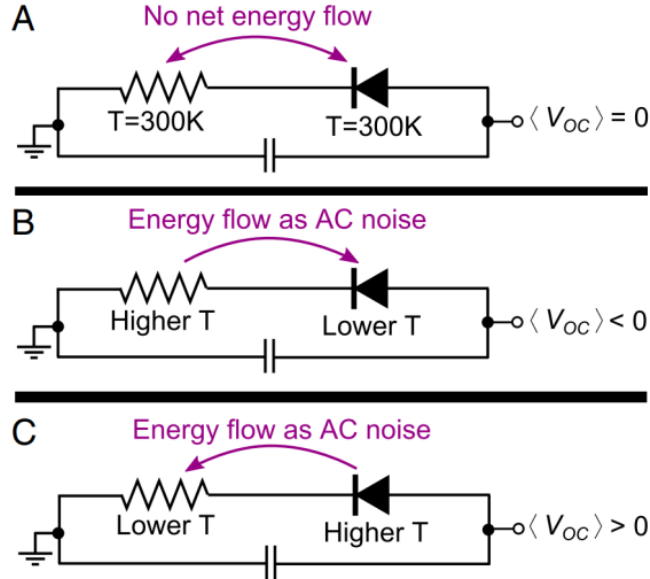


Figure 2.2: Three configurations of the classical diode-resistor generator circuit. (A) In thermal equilibrium where the diode and resistor are at the same temperature, no net flow of energy or open-circuit voltage are measured. (B) When the resistor temperature ( $T_R$ ) is higher than the diode temperature ( $T_D$ ), the resistor’s thermal fluctuations (AC noise) are rectified by the diode and produce a DC signal. (C) Similarly, when the diode is hot ( $T_R < T_D$ ), the thermal fluctuations of the diode are rectified and DC power is produced (Byrnes et al., 2014).

Analogous to the three resistance configurations presented by Byrnes et al. is a rectenna circuit radiatively coupled to a surface at the same temperature with zero net power generation, a rectenna net absorbing electromagnetic radiation from a hot surface and a rectenna net radiating power to a cold surface, as shown in Fig. 2.3. Detailed balance (Boltzmann and Brush, 1964) in such a system dictates that the cold rectenna system absorbing heat from a hot reservoir (Fig. 2.3a) produces the same power as a hot rectenna radiating to a cold reservoir though the antenna (Fig. 2.3b), assuming that the rectifier is not temperature dependent, but it is, fundamentally. Both systems have the same requirements and face the same challenges: achieving a low RC time constant, matching antenna and diode impedances and maximizing diode rectification efficiency. Differences between the two generally arise from temperature-dependent properties within the

system itself, such as the MI<sup>2</sup>M diode  $I(V)$  characteristics where the Fermi-Dirac distribution changes with temperature. The practical success of such a system relies heavily on the diode's  $I(V)$  characteristics and asymmetry at low voltages ( $< 10$  mV), since the input power from a resistor is extremely low resulting in low self-bias operating voltages.

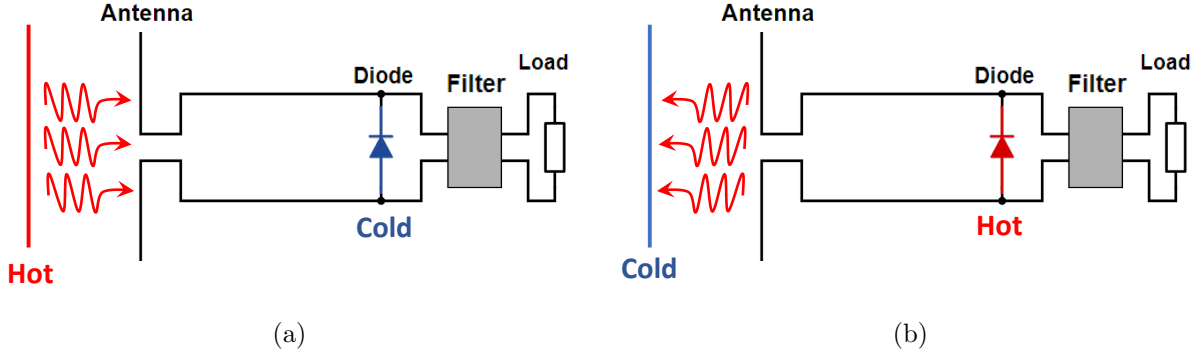


Figure 2.3: Rectenna detailed balance with (a) a cold rectenna system absorbing heat from a hot reservoir and (b) a hot rectenna radiating to a cold reservoir.

In the next sections, I explore this diode-resistor generator circuit theoretically to determine its expected efficiency under a temperature gradient. The simplicity of this system provides valuable insight into rectenna operation under the conventional configuration of absorbing heat or the intriguing configuration of radiating to a cold reservoir. I begin with revisiting the rectenna efficiency limit under broadband illumination presented by Joshi (Joshi, 2015).

## 2.2 Rectenna efficiency under broadband illumination

The power conversion efficiency of a rectenna depends on the performance of its components, which can be lumped into three main efficiencies: the antenna absorption efficiency (which includes significant material losses at high frequencies), diode rectification efficiency, and the antenna-diode coupling efficiency. The DC output power, the power produced by the rectenna for a given incident intensity, is the product of the rectified (DC) output current (the illuminated current  $I_{illum}$ ) and the DC output voltage (operating voltage ( $V_O$ )). The ratio of rectified current to incident optical power, known as responsivity, determines the rectification efficiency of a diode. For monochromatic light,

one electron is generated per incident photon and an operating voltage ( $V_O$ ) of  $\hbar\omega/q$  corresponds to an ultimate efficiency limit of 100%. The process is more complicated for broadband illumination, since each incident optical frequency would require its own operating voltage, but the diode only operates at a single voltage. In his work, Joshi discusses how to calculate the illuminated  $I(V)$  characteristics of a rectenna, using an iterative method to determine the operating voltage and the rectified current (Joshi and Moddel, 2013). For the clamping circuit of a rectenna, presented in Fig. 2.4, the time-dependent voltage across the diode is expressed as

$$v_D(t) = -|V_O| + v_s(t) - i_S(t)R_S \quad (2.3)$$

where  $i_S(t)$  is the AC current in the antenna circuit and  $R_S$  is the equivalent antenna resistance. The operative voltage  $|V_O|$  is equal to the clamping voltage across the capacitor  $C$ . The total current through the diode is simply  $i_D(t) = i_S(t) + I_{illum}$ . For each  $V_O$  value, Eq. 2.3 is solved iteratively to calculate  $v_D(t)$  and  $i_S(t)$ . Each new value of  $v_D(t)$  is used to calculate  $i_S(t)$  using the diode  $I(V)$  characteristics. The relationship between  $i_D(t)$  and  $v_D(t)$  is determined using photon-assisted tunneling (PAT) theory, as will be explained in the next subsection.

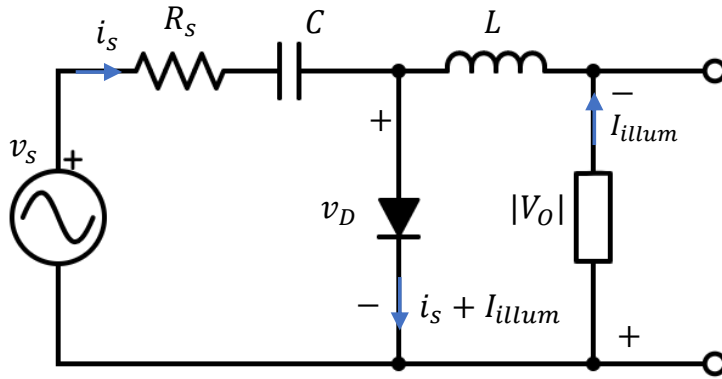


Figure 2.4: Rectenna equivalent circuit. The antenna is modeled as a voltage source ( $v_s$ ) in series with a resistance ( $R_s$ ). The DC current in the antenna is blocked using a capacitor  $C$ . The inductor  $L$  blocks AC power from being dissipated in the load. The current through the antenna is  $i_S(t)$  and the rectified current is  $I_{illum}$ . The total current through the diode,  $i_D(t)$ , is  $i_S(t) + I_{illum}$ . Power delivered to the load  $R_L$  is calculated as  $I_{illum}$  multiplied by the DC operating voltage  $V_O$  (Joshi, 2015). This is the structure used to solve for  $V_O$  and  $I_{illum}$  in the iterative solver.

Joshi employs this method to calculate the optical response of a rectenna under broadband illumination, such as a hot blackbody. The antenna is assumed to have a frequency-independent impedance and effective area (no losses due to being designed for optimum performance for a single frequency operation - these will be later referred to as broadband losses), and is modeled using a source voltage which is consistent with the expected blackbody spectrum. This is done by taking the inverse-Fourier transform of a blackbody spectrum to obtain a source voltage signal with the desired characteristics. The resultant time-dependent voltage signal allows the use of the developed iterative method. Accurate calculation of a voltage signal consistent with the blackbody spectrum requires two main simulation conditions: 1) application of a random phase to each different frequency component in the Planck blackbody spectrum and 2) normalization of the time-dependent voltage such that the voltage signal  $V_S$  has total average power  $P_{in}$  (Joshi and Modell, 2013).

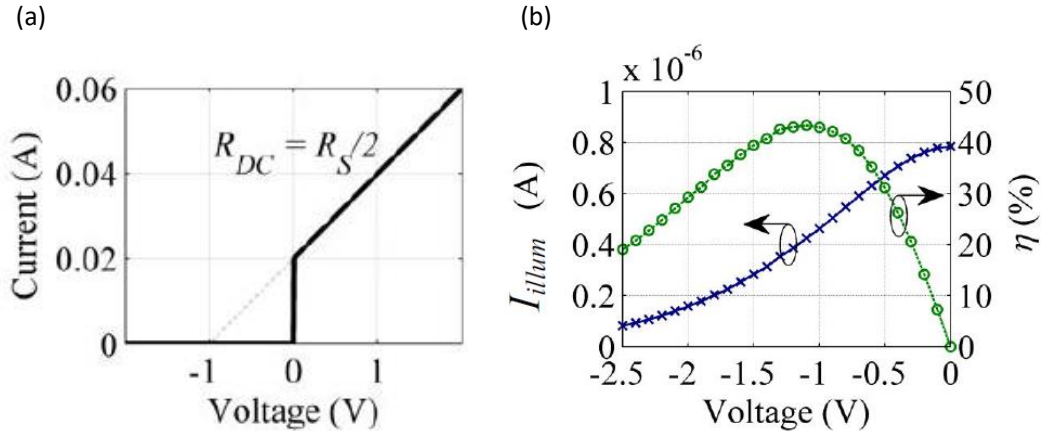


Figure 2.5: Broadband illuminated  $I(V)$  and conversion efficiency calculation for a blackbody source of temperature 5780 K for (a) an ideal diode with zero capacitance used for optical matching to the antenna. Perfectly matching the diode and the antenna requires the first quadrant differential resistance ( $R_{DC}$ ) to be half the antenna impedance ( $R_S$ ) with an x-axis intercept at  $V_O$ . (b) The conversion efficiency of this rectenna peaks at  $V_O = -1.1$  V with an efficiency of  $\sim 44$  % (Joshi and Modell, 2013).

Figure 2.5 presents  $I(V)$  characteristics of an ideal diode used for optical matching to the antenna and its corresponding response to illumination from a blackbody source of  $T = 5780$  K, with an input power of  $1.1 \mu\text{W}$ . Perfectly matching the diode and the antenna requires the first

quadrant differential resistance to be half the antenna impedance with an x-axis intercept at  $V_O$  (Joshi and Moddel, 2013), as shown in Fig. 2.5 (a). In this example, the diode operates in the quantum regime due to the low input power and the corresponding low source voltage (Joshi and Moddel, 2016). The conversion efficiency of this rectenna peaks at  $V_O = -1.1$  V. The calculated efficiency is consistent with the Trivich-Flinn limit of  $\sim 44$  % (Trivich et al., 1955, Green, 2012) since photons with energy less than  $q|V_O|$  do not contribute to current as they do not have sufficient energy to tunnel, while photons with energy greater than  $q|V_O|$  contribute part of their energy to generate current at  $V_O$ . Similar to conventional solar cells, where the limit results from a single bandgap energy, here the Trivich-Flinn efficiency limit results from the single operating voltage of the diode. Under practical constraints, such as diode radiative recombination and finite temperature of the diode, the maximum efficiency is reduced to the Shockley-Queisser limit of 33% (Shockley and Queisser, 1961). Further reduction in total conversion efficiency is expected when realistic antenna and diode limitations are imposed.

### 2.2.1 Photon-assisted tunneling

The response of a rectenna under optical illumination is determined using the theory of photon-assisted tunneling (PAT) (Dayem and Martin, 1962, Tien and Gordon, 1963, Tucker, 1979). Tien and Gordon examined the multiphoton-assisted tunneling current in superconducting diodes (Tien and Gordon, 1963), where microwave radiation gave rise to DC tunneling current in voltage steps of  $\hbar\omega/q$ . Mathematically, this is equivalent to sampling the diode dark  $I(V)$  characteristics at voltage steps of  $\hbar\omega/q$ , written as (Joshi and Moddel, 2013)

$$I_{illum} = \sum_{n=-\infty}^{\infty} J_n^2 \left( \frac{qV_D}{\hbar\omega} \right) \times I_{dark} \left( V_o + n \frac{\hbar\omega}{q} \right) \quad (2.4)$$

where  $V_D$  is the amplitude of the AC voltage across the diode,  $I_{dark}$  is the diode DC dark current and  $J_n$  is the Bessel function of order n. The Bessel terms are determined by the available electrons for tunneling through the barrier, which is affected by source intensity and photon energy (Grover et al., 2013, Joshi and Moddel, 2013). At high frequencies and low intensities, when  $\hbar\omega > qV_D$ , the

only significant Bessel terms are  $n = -1, 0$  and  $1$ . Only electrons with energies equal to the Fermi level ( $n = 0$ ), and to one photon energy lower ( $n = -1$ ) and one higher ( $n = 1$ ) than the Fermi level, are available for tunneling across the barrier, as illustrated in Fig. 2.6.

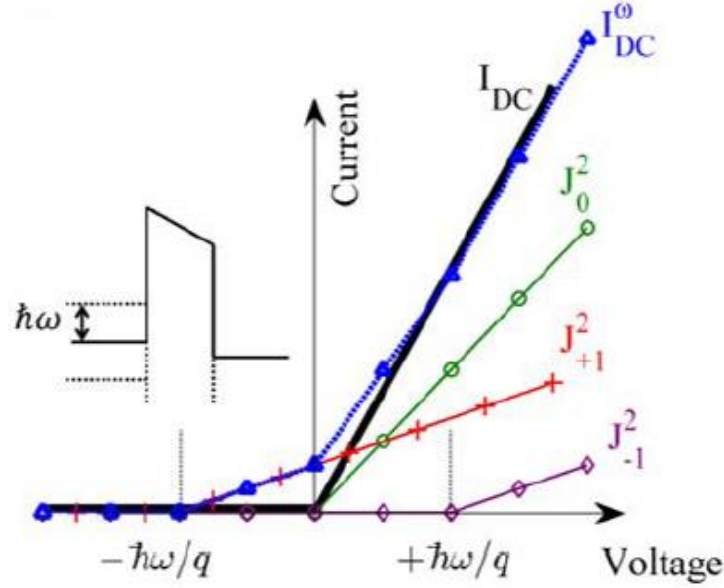


Figure 2.6: The effects of photon-assisted tunneling (PAT) on diode  $I(V)$  characteristics under illumination. The DC tunneling current ( $I_{DC}^\omega$ ) is the combination of three tunneling currents with Bessel terms  $J_0^2$ ,  $J_{-1}^2$  produced by photon emission and  $J_{+1}^2$  produced by photon absorption. The inset illustrates the energy band diagram of an MIM diode under DC bias (Joshi and Moddel, 2013).

Tucker (Tucker, 1979) also studied the interaction of high-speed diodes with quantized photons and presented a generalized PAT theory where diode current ( $i_D(t)$ ) can be calculated as

$$i_D(t) = \int \int d\omega' d\omega'' W(\omega') W^*(\omega'') e^{-i(\omega' - \omega'')t} I_{dark} \left( \omega' + \frac{qV_O}{\hbar} \right). \quad (2.5)$$

The phase modulation factor,  $W$ , is the result of Fermi level modulation in the diode metal contact due to the applied AC voltage perturbation, and is related to the diode voltage  $v_D(t)$  through its Fourier transform

$$\exp \left\{ -i \frac{q}{\hbar} \int^t dt' [v_D(t')] \right\} = \int_{-\infty}^{\infty} d\omega' W(\omega') e^{i\omega' t}. \quad (2.6)$$

The illuminated current  $I_{illum}$  that flows through the load is the average of the current  $i_D(t)$ . At

the self-bias DC operating voltage ( $V_O$ ), the DC output power is

$$P_{out}^{DC} = |V_O| \times I_{illum}(V_O). \quad (2.7)$$

### 2.3 Thermal noise rectifier equivalent circuit

PAT theory applies in the semi-classical (quantum) regime when the photon energy divided by electron charge ( $\hbar\omega/q$ ) is larger than the amplitude of the AC voltage across the diode ( $v_D$ ) (Joshi and Moddel, 2013). The typical temperature of low-grade waste heat ranges between 287 K and 350 K. The blackbody spectrum of objects with these temperatures peaks in the range of 8 - 10  $\mu\text{m}$ . That corresponds to

$$\frac{\hbar\omega}{q} = \frac{hf}{q} = \frac{(6.6 \times 10^{-34} \text{ m}^2\text{kg/s})(28.3 \times 10^{12}/\text{s})}{1.6 \times 10^{-19} \text{ C}} = 153 \text{ mV}. \quad (2.8)$$

The amplitude of the AC voltage across the diode is typically 100  $\mu\text{V}$  - 10 mV, limited by the antenna impedance and input power available, and therefore PAT can be applied. In this section, I employ Joshi's iterative diode voltage calculation methods to determine the operating voltage ( $V_O$ ) and illuminated current ( $I_{illum}$ ) and calculate the output power and total conversion efficiency of an MI<sup>2</sup>M diode rectifying thermal noise from a hot resistor..

For thermal noise rectification, the antenna is replaced with a hot source resistor,  $R_S$ , and modeled as being in series with its noise voltage source ( $v_n^S$ ). The noise voltage signal is generated using the inverse Fourier transform of the noise frequency spectrum. The clamping capacitor  $C$  in the circuit, also presented in Fig. 2.4, allows the output DC voltage to approach the AC peak voltage. The voltage across the capacitor is the operating voltage across the load (Joshi and Moddel, 2013). The low-pass filter  $L$  blocks the AC power from being dissipated in the load ( $R_L$ ). The diode is modeled as an ideal diode in series with a resistor  $R_D$  and an associated diode noise source  $v_n^D$ .

At thermal equilibrium, where the temperature of the resistor  $R_S$  is equal to the temperature of the diode and its internal resistance  $R_D$ , the rectified current  $I_{illum}$  should be equal to zero. We next examine the proposed circuit in Fig. 2.7 to ensure the second law of thermodynamics holds. For short circuit conditions, we replace the source resistor  $R_S$  with a short circuit, as seen

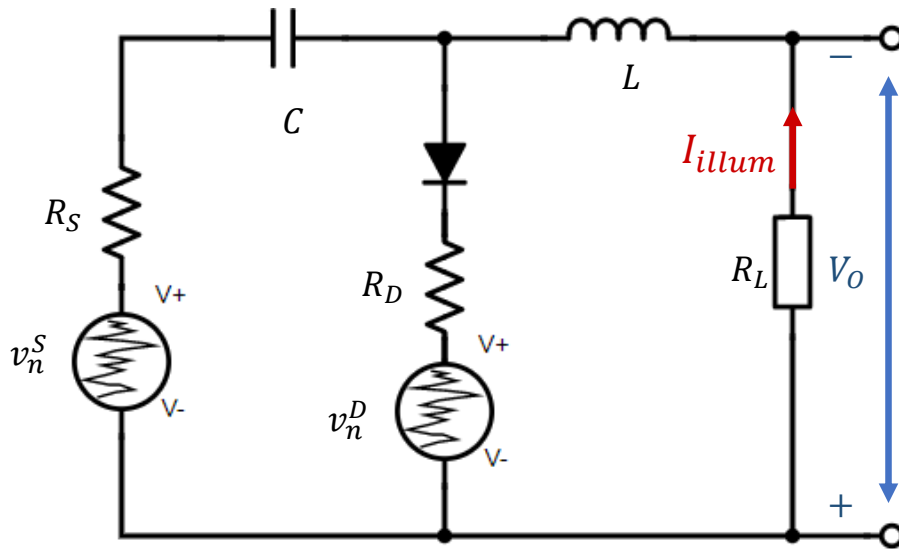


Figure 2.7: Thermal noise rectifier equivalent circuit. The resistor  $R_S$  has a noise voltage source  $v_n^S$  computed from the inverse Fourier transform of the Planck distribution. The clamping capacitor  $C$  in the circuit allows the output DC voltage to approach the AC peak voltage. The low-pass filter  $L$  blocks the AC power from being dissipated in the load. The diode is modeled as an ideal diode in series with a resistor  $R_D$  and noise source  $v_n^D$ .

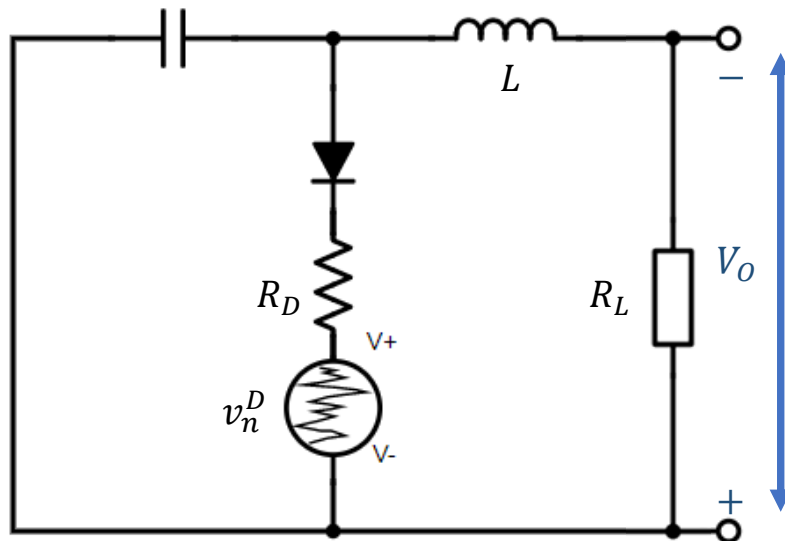


Figure 2.8: Thermal noise rectifier equivalent circuit under Short-circuit conditions where the source resistance is replaced with a short circuit. The thermal noise produced is rectified in the diode and power is generated. The circuit violates the second law of thermodynamics.

in Fig. 2.8. Thermal noise in the diode is dissipated in its internal resistance as heat and a DC current is produced as the diode rectifies part of the power emitted by its resistor, even at thermal equilibrium. This system violates the second law of thermodynamics.

To make the circuit consistent with the second law, we add a current source to cancel the rectified current generated at thermal equilibrium (Joshi and Moddel, 2015). We use PAT to calculate the rectified current from  $R_S$  and  $R_D$  at the same cold temperature  $T_C$  and determine the value of the current source,  $I_0$ , as shown in Fig. 2.9. The same issue is present when using PAT theory to calculate power generated from a rectenna when the blackbody radiation is at room temperature, and would require the use of an artificially added current source to the circuit. Next, we calculate the combined rectified current from  $R_S$  at the hot temperature  $T_H$  and  $R_D$  at the cold temperature  $T_C$ . The resulting rectified current  $I_{rectified}$  is expressed as

$$I_{rectified} = I_S - I_0. \quad (2.9)$$

$$I_{rectified} = I_{illum}(v_n^D(T_C) + v_n^S(T_H)) - I_{illum}(v_n^D(T_C) + v_n^S(T_C)). \quad (2.10)$$

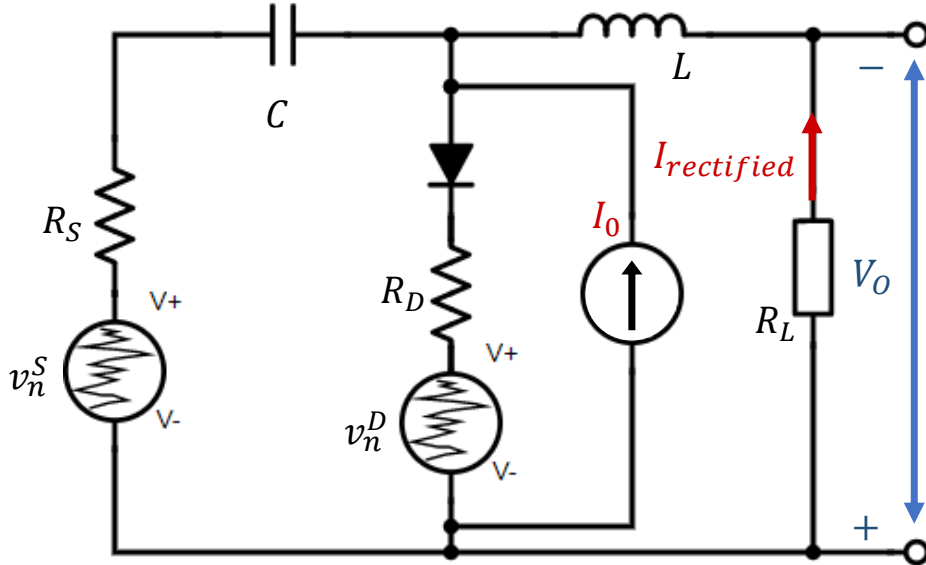


Figure 2.9: Modified Thermal noise rectifier circuit.

## 2.4 Thermal noise rectification efficiency with MI<sup>2</sup>M diodes

I use the method described in the previous section to calculate the optical response of an MI<sup>2</sup>M diode connected to a hot resistor. The temperature of the diode is maintained at 200 K, while the temperature of the hot resistor is varied between 200 and 300 K. An example thermal noise voltage signal computed from the inverse Fourier transform of the one-dimensional blackbody spectrum is presented in Fig. 2.10. The low input power of the system ( $P_{in} \sim 10 - 100$  nW) at ambient temperatures calculated from the blackbody radiation in a square meter with around a billion diodes (discussed in Ch. 7), and the resulting low self-bias voltage ( $< 10$  mV), cause the diode to operate in the quantum regime where the semi-classical theory of PAT applies (Joshi and Modell, 2016). To evaluate the efficiency of realistic MI<sup>2</sup>M diodes, I use the asymmetry ( $I(V)/I(-V)$ ) of a fabricated and measured Co/Co<sub>3</sub>O<sub>4</sub>/TiO<sub>2</sub>/Ti MI<sup>2</sup>M diode, as shown in Fig. 2.11 (a), with an imposed zero-bias resistance ( $R_0$ ) equal to 100  $\Omega$ . The source resistance is chosen to be 100  $\Omega$ . This diode has an asymmetry of 1.2 at a voltage of 100 mV and a zero-bias responsivity of  $\sim 0.8$  A/W. Knowing the source voltage  $v_S(t)$  and the diode  $I(V)$  characteristics, I iteratively solve for different  $V_O$  values using PAT theory to calculate  $I_{rectified}$ . The DC output power  $P_{out}^{DC}$  and total conversion efficiency  $\eta$  are calculated as

$$\eta = \frac{P_{out}^{DC}}{P_{in}} = \frac{|V_O|I_{rectified}(V_O)}{P_{in}}. \quad (2.11)$$

Figure 2.11 (b) presents simulation results of the diode's total power conversion efficiency and a scaled Carnot efficiency curve for ease of comparison. The total thermal noise power conversion efficiency is 1.34 % at a temperature gradient ( $\Delta T$ ) = 100 K. These simulations do not take into account RC time constant or broadband losses (losses due to components designed to optimize performance at a single frequency). The same efficiency presented in Fig. 2.11 is expected for a hot diode in radiative contact with a cold surface, following detailed balance. In a system with an ideal diode perfectly matched to the antenna, the efficiency will approach the Carnot limit (Santhanam and Fan, 2016).

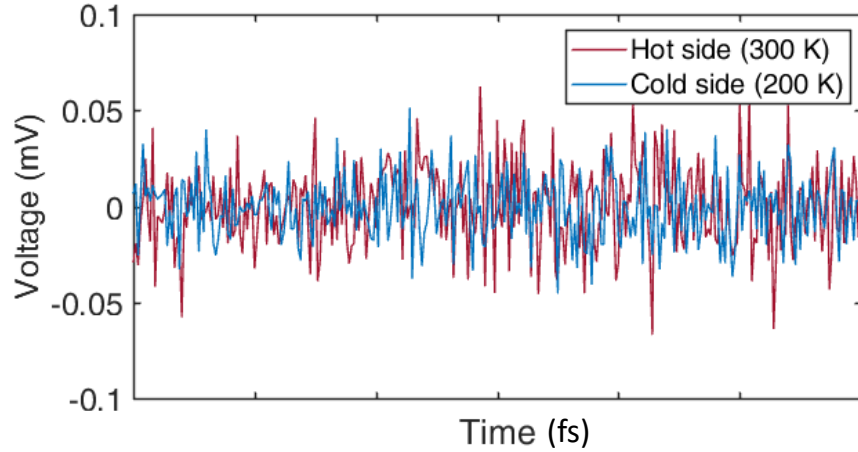


Figure 2.10: The thermal noise voltage signal, computed from the inverse Fourier transform of the one-dimensional blackbody spectrum. The diode temperature, the cold side, is 200 K and the resistor temperature, the hot side, is 300 K.

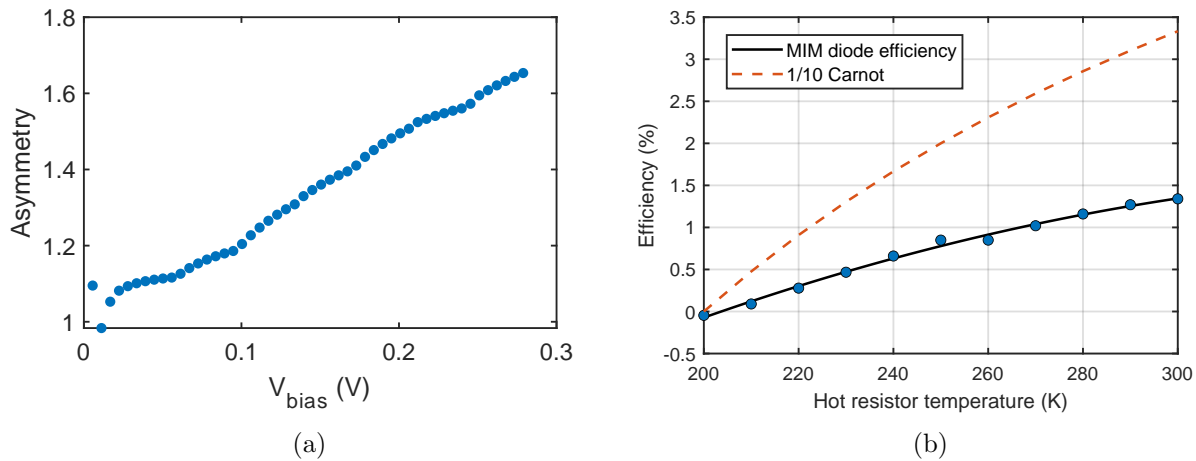


Figure 2.11: Simulated power conversion efficiency for a  $\text{Co}/\text{Co}_3\text{O}_4/\text{TiO}_2/\text{Ti}$  MI<sup>2</sup>M diode with (a) an asymmetry of 1.2 at 100 mV. The measured  $I(V)$  curve is interpolated before the asymmetry is calculated as  $I(V)/I(-V)$ . (b) Total power conversion efficiency as a function of resistor temperature compared with a scaled Carnot efficiency curve.

## 2.5 Conclusion

In this chapter, I described the procedure of calculating rectenna circuit response under broadband illumination and diode rectification of thermal noise from a hot resistor. For realistic MI<sup>2</sup>M characteristics, the maximum power conversion efficiency with a temperature gradient of 100

K approaches 1.5%. Because of impedance mismatch between measured diodes ( $\sim 1\text{-}2\text{ k}\Omega$ ) and their antennas ( $\sim 50\text{ - }100\ \Omega$ ), the coupling efficiency is below 1% which further reduces the input power to the diode and its rectification efficiency to  $10^{-2}\%$ . A blackbody generates  $459\text{ W/m}^2$  at room temperature. Around 4 billion diodes can be spread over an area of  $1\text{ m}^2$ , with an input power of  $114\text{ nW}$  to each diode. With a coupling efficiency of  $10^{-2}\%$  and a diode rectification efficiency of  $10^{-2}\%$ , the expected output power is  $4.59\ \mu\text{W/m}^2$ . Increasing the total efficiency requires better understanding of MI<sup>2</sup>M diodes to achieve high asymmetries at low operating voltages, due to the low input power from ambient heat, and increasing the coupling efficiency. I explore these concepts in the next chapters.

## CHAPTER 3

### EXPERIMENTAL METHODS

Diodes in this work were fabricated using a modified germanium shadow mask (GSM) process (Hobbs et al., 2005, Bean et al., 2011, Pelz and Moddel, 2019). Because the GSM process uses only a single lithography step before any material depositions, it is ideal for diode material testing and thickness analysis. The ability to deposit ultra-thin oxides and to combine multiple insulators in a device enables the tailoring of the diode's characteristics for high frequency operation. The GSM also facilitates the fabrication of structures with feature sizes beyond the resolution of the lithography due to the shadowing effect from the suspended bridge and angled evaporation.

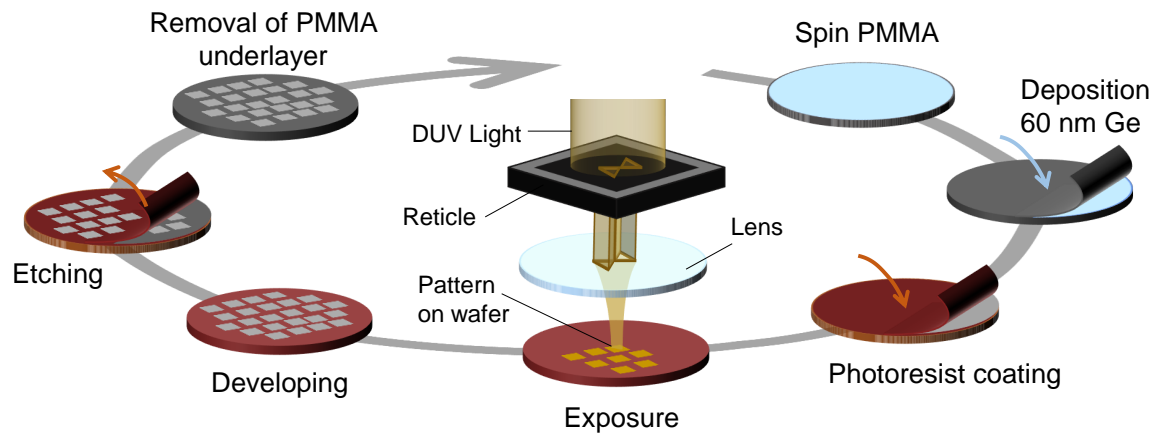


Figure 3.1: Device fabrication process, starting with 300 nm of thermal oxide deposited on a silicon wafer. First, PMMA is spun on the wafer followed by 60 nm of evaporated germanium. Next, I coat with photoresist and expose at 248 nm. The reticle contains the mask and design pattern. The stepper prints around 20 dies on the wafer. I then develop the desired pattern and etch the pattern onto the germanium and remove the underlayer of PMMA. What is left is a suspended Ge bridge supported by a PMMA undercut.

### 3.1 Germanium shadow mask process

The devices were fabricated on 4 inch, high-resistivity silicon wafers with a 300 nm layer of thermally grown  $\text{SiO}_2$ . First, I spin 4% polymethyl-methacrylate (PMMA) in anisole solution onto the wafer at a thickness of 260 nm and bake it at  $180^\circ\text{C}$  for 15 min to removed all the solvent. Next, I evaporate 60 nm of germanium on the wafer, followed by an anti-reflective coating and photoresist. Anti-reflective coating reduces interference-related artifacts and unwanted exposure by reflections on wafer structures. I use an ASML 5500 248 nm DUV stepper in the nanofabrication cleanroom at the University of California, Santa Barbara to print our pattern. The pattern is then etched into the germanium with a  $\text{CF}_4$  reactive ion etch, followed by an  $\text{O}_2$  plasma clean to remove the under layer of PMMA. The complete process is illustrated in Fig. 3.1. It is necessary to ensure the PMMA removal undercuts the Ge to be able to perform angled evaporation. The top view in the insert of Fig. 3.2 presents the pattern printed on the wafer with the cross-section illustrated in the full figure. The cross section shows a suspended Ge bridge supported by PMMA.

### 3.2 Material deposition

In this thesis, I will focus on one material set: Ni/NiO/ $\text{Al}_2\text{O}_3$ /Cr/Au. After dicing the wafer into individual dice ( $\sim 2\text{ cm}^2$ ), I perform an additional 5 min  $\text{O}_2$  plasma clean in a reactive ion etcher (March Jupiter III plasma system) at a pressure of 350 mTorr (100 W) to remove any organic contaminates and ensure a good PMMA undercut beneath the germanium. The first metal, Ni, is then thermally evaporated at an angle  $\theta = 43^\circ$  or  $\theta = 39.5^\circ$  from the right. The deposition angle varies depending on the desired overlap, the Ge bridge width and PMMA thickness. Next, nickel oxide is either grown in  $\text{O}_2$  plasma (30 W power, 50 mTorr pressure) or DC reactively sputter deposited (60 W power, 2.5 mTorr pressure) from a Ni target in an  $\text{O}_2/\text{Ar}$  plasma.  $\text{Al}_2\text{O}_3$  is RF reactively sputter deposited (75 W power, 2.5 mTorr pressure) from an  $\text{Al}_2\text{O}_3$  ceramic target in Ar plasma. Depending on the desired overlap, a layer of Cr and a layer of Au are evaporated at either normal incidence (for  $\theta_{Ni} = 45^\circ$ ) or at an angle of  $\theta = 39.5^\circ$  from the left (for  $\theta_{Ni} = 39.5^\circ$ ). The

thin Cr layer provides a good barrier for asymmetric diodes, and the Au layer provides a low loss tangent for illuminated measurements. Excess metal was lifted off in an acetone bath.

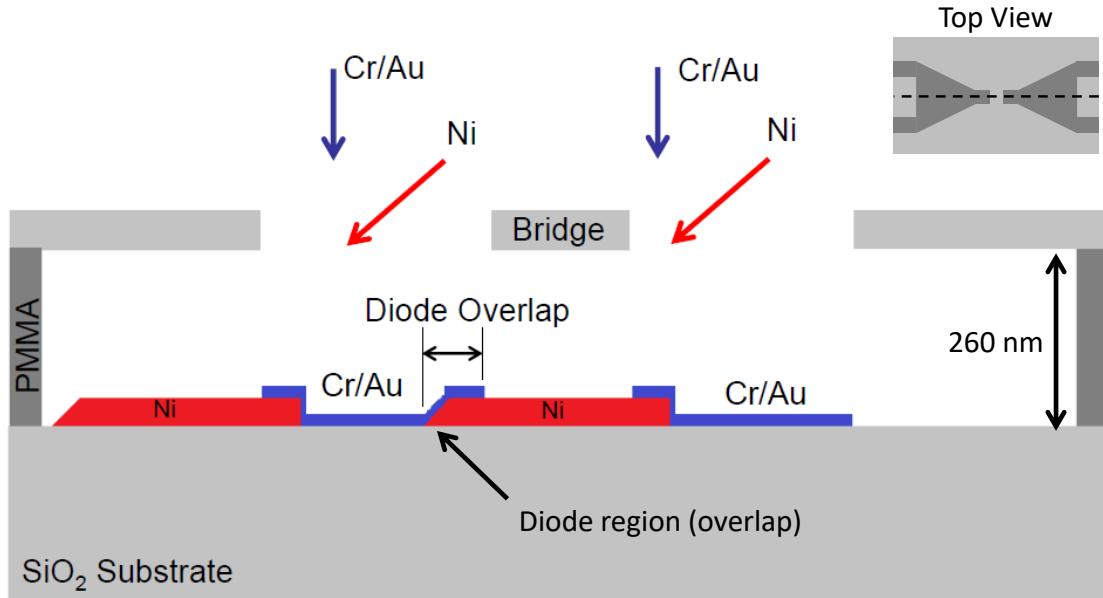


Figure 3.2: Diode fabrication with germanium shadow mask process. Insert shows top view of the device while figure shows the cross section with the suspended Ge bridge on PMMA. Image modified from Brad Pelz's thesis (Pelz, 2018).

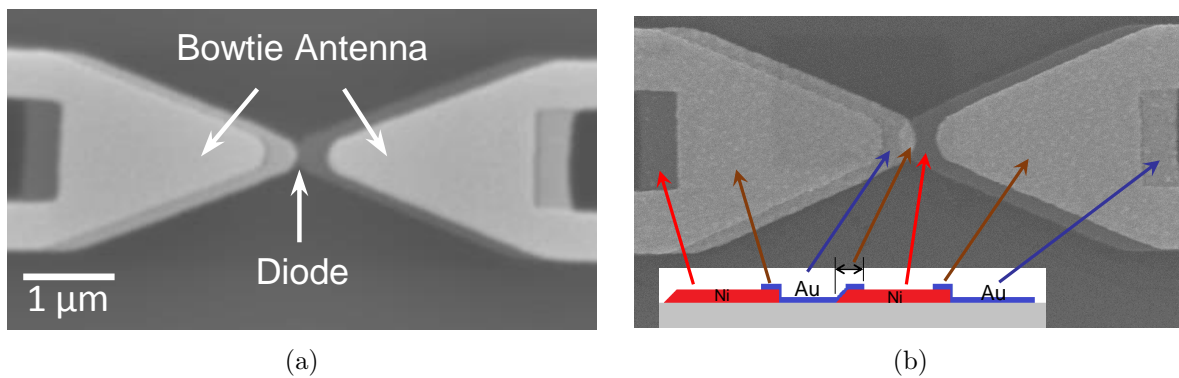


Figure 3.3: (a) Scanning electron microscopy (SEM) image of lumped element configuration with a bowtie antenna. (b) SEM image with the cross section of deposited materials highlighting the shadowing effect of the germanium shadow mask process with the seven regions of materials. SEM image taken by Ayendra Weerakkody.

### 3.3 Diode characterization

The rectenna consists of a bow-tie antenna with two opposing  $2.3 \mu\text{m}$ -long triangular arms and a diode junction at its feed point. Figure 3.3a presents a scanning electron microscopy (SEM) image of a fabricated lumped-element diode. Figure 3.3b presents the SEM image with the cross section of deposited materials highlighting the shadowing effect of the germanium shadow mask process with the seven regions of materials.

#### 3.3.1 DC measurements

The first step in experimentally analyzing and testing an optical rectenna is measuring the DC current-voltage [ $I(V)$ ] characteristic of fabricated MIM diodes. DC  $I(V)$  characteristics are measured using a 4-point probe setup to eliminate lead resistance effects of the probe/wiring structure. I use a Keithley 2602 source meter as a source current and an HP 3478A multimeter to measure voltage. I sweep the voltage over a limited range of -300 mV to +300 mV to avoid breaking down the sub-nanometer thick dielectrics. The diode metrics of interest, which are central in assessing a diode's suitability for use in an optical rectenna, are the dynamic resistance and responsivity, shown in Fig. 3.4, and defined as

$$R(V) = \frac{1}{I'(V)} \quad (3.1)$$

$$\beta(V) = \frac{1}{2} \frac{I''(V)}{I'(V)} \quad (3.2)$$

A high diode responsivity, which is an indication of the device nonlinearity and a measure of the DC current generated per unit incident radiation, is required for efficient rectification. A low diode resistance is desired for high coupling efficiency between the MIM diode and the antenna and for a high cutoff frequency. For our diodes, I am interested in differential resistance and responsivity near zero-bias. Zero-bias values are sufficient to assess performance of these diodes in energy harvesting applications, where they self-bias at approximately  $100 \mu\text{V}$  under open circuit conditions. To smooth out measurement noise, an exponential fit (Pelz et al., 2018) was used on the measured  $I(V)$  data before extracting resistance and responsivity.

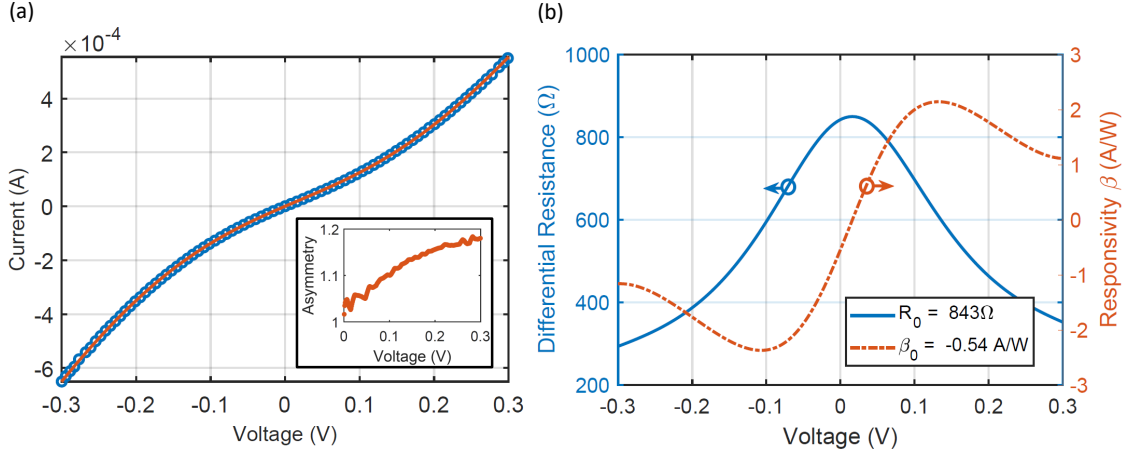


Figure 3.4: (a) Current-voltage characteristics of an MIM diode. The measured data is presented in blue circles with the fit presented in a solid orange line. The insert represents diode asymmetry. (b) differential resistance and responsivity curves with zero-bias resistance ( $R_0$ ) and zero-bias responsivity ( $\beta_0$ ).

### 3.3.2 Optical measurements

The optical measurement setup of the rectenna is presented in Fig. 3.5. The high frequency response of rectennas was assessed by illuminating them with a SYNRAD 481SWJ 10.6  $\mu\text{m}$  linearly polarized pulsed  $\text{CO}_2$  laser. The laser power was controlled by changing the pulse width at 20.0 kHz from an Agilent 33220A function generator. A Stanford Research System (SR540) chopper is used to mechanically chop the laser beam at 2 kHz as well as provide a reference for the lock-in amplifier (SR830). The beam passes through a shutter (ThorLabs SH05), a half-wave plate (Gooch and Housego XC13), and a focusing lens before illuminating the diode. The half-wave plate rotates the laser polarization with respect to the antenna axis. Two-point probe measurements were performed to compute open-circuit voltage ( $V_{oc}$ ) and short-circuit current ( $I_{sc}$ ) of the antenna-coupled diodes.

The polarization angle of the incident laser beam is varied with respect to the antenna axis. Peak  $V_{oc}$  is expected when the polarization angle of the beam is either  $0^\circ$  or  $180^\circ$  where the beam is parallel to the antenna axis. The  $V_{oc}$  should be comparable to the noise level when the polarization angle is  $90^\circ$ , i.e., perpendicular to the antenna axis, as seen in Figure 3.5. After the  $V_{oc}$  measurements, the  $I_{sc}$  values were measured at  $0^\circ$ . It is important to note that the lock-in

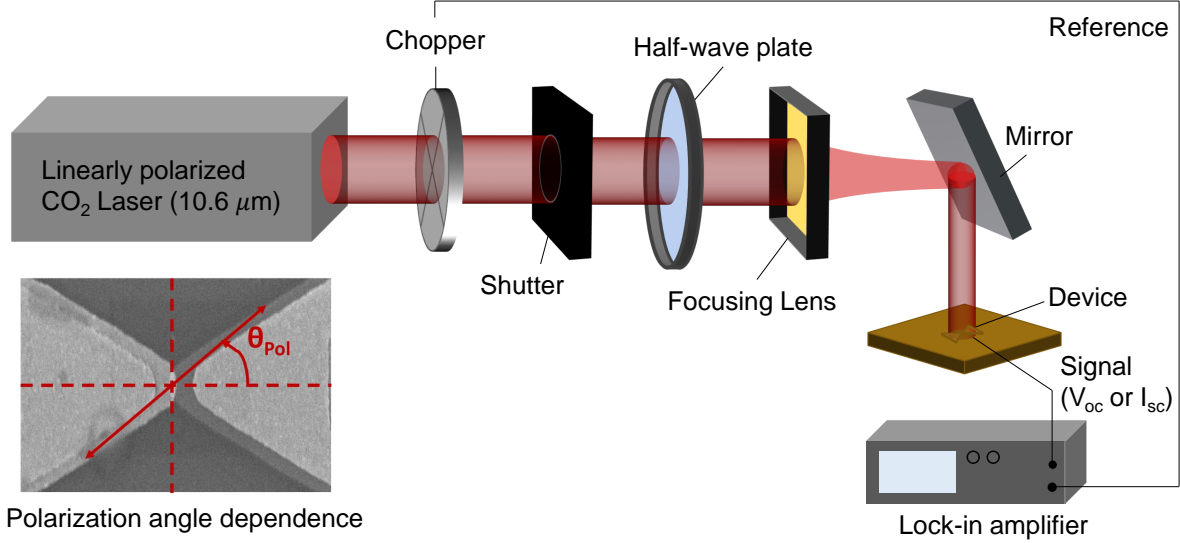


Figure 3.5: Infrared optical illumination measurement setup with linearly polarized CO<sub>2</sub> laser. SEM shows polarization angle dependence with respect to antenna Axis. SEM image taken by Ayendra Weerakkody.

amplifier measures RMS values with a function generator duty cycle  $D$  (Pelz, 2018), which modifies the measured values such that

$$V_{oc} = \frac{V_{rms}\pi}{D\sqrt{2}} \quad (3.3)$$

The same correction is applied to measured  $I_{sc}$  values. The measured  $V_{oc}$  against polarization angle is fit using the following equation

$$V_{oc}(\theta) = A_{\parallel}\cos(\theta + \phi)^2 + A_{\perp}\sin(\phi)^2 \quad (3.4)$$

where  $\theta$  is the polarization angle and  $\phi$  is the angular shift due to alignment issues or beam wander. Beam wander, which results from laser power fluctuations and laser beam instability, could result in angular shift up to  $\phi = 10^\circ$ , as discussed in detail in Pelz's thesis (Pelz, 2018). A dominant cosine-squared relationship indicates rectification and a sine-squared relationship indicates thermal effects (Bareiβ et al., 2013). More information on fabrication and optical measurements is available in Pelz's thesis (Pelz, 2018).

### 3.4 Conclusion

In this thesis, I use the GSM technique to fabricate two different material sets: Ni/NiO/Cr/Au single-insulator MIM diodes and Ni/NiO/Al<sub>2</sub>O<sub>3</sub>/Cr/Au double-insulator MI<sup>2</sup>M diodes. The GSM techniques allows for small feature sizes and clean diode interfaces, as well as repeatable diodes with fast fabrication turn around. Diodes fabricated in this work were characterized using SEM images to confirm desired overlap regions and determine diode areas. Following fabrication, the diodes were DC measured using a four-point probe setup, as well as optically measured under 10.6  $\mu\text{m}$  laser illumination, to verify polarization dependence and measure the open-circuit voltage and short-circuit current. Diode metrics, such as dynamic resistance, responsivity, asymmetry, open-circuit voltage, and short-circuit current, are used to compare diodes and evaluate their total conversion efficiency.

## CHAPTER 4

### MI<sup>2</sup>M DIODE ANALYSIS: RESISTIVE AND CAPACITIVE VOLTAGE DIVISION

We review an erroneous method for distributing DC voltage drops across multiple insulator layers that is used in all the published literature on these devices. It has resulted in large errors between designed and fabricated multi-insulator diodes. For multi-insulator MIM diodes, voltage division is dependent on both tunneling resistances and oxide capacitances. To determine the validity of resistive and capacitive voltage division among insulating layers, we use measurements and simulations to compare diode characteristics at DC and under 28 THz infrared illumination for single and double-insulator diodes. We demonstrate that correct voltage division at DC is determined by the rectification resistance, as opposed to the commonly used capacitive voltage division. Because the high frequency voltage division is dependent on both the resistance and the capacitance, which is frequency dependent, we find that DC characteristics of multi-insulator diodes cannot be used to predict high frequency behavior. Work carried out in this chapter was performed in close collaboration with Ayendra Weerakkody.

#### 4.1 Introduction

Designing diodes for high frequency operation requires accurate knowledge of the shape of the diode's energy band diagram. The difficulty in designing multi-insulator diodes stems from correctly determining the slope of the conduction band edge of each dielectric, which is determined by the voltage division across each oxide. By choosing different oxides with particular thicknesses,

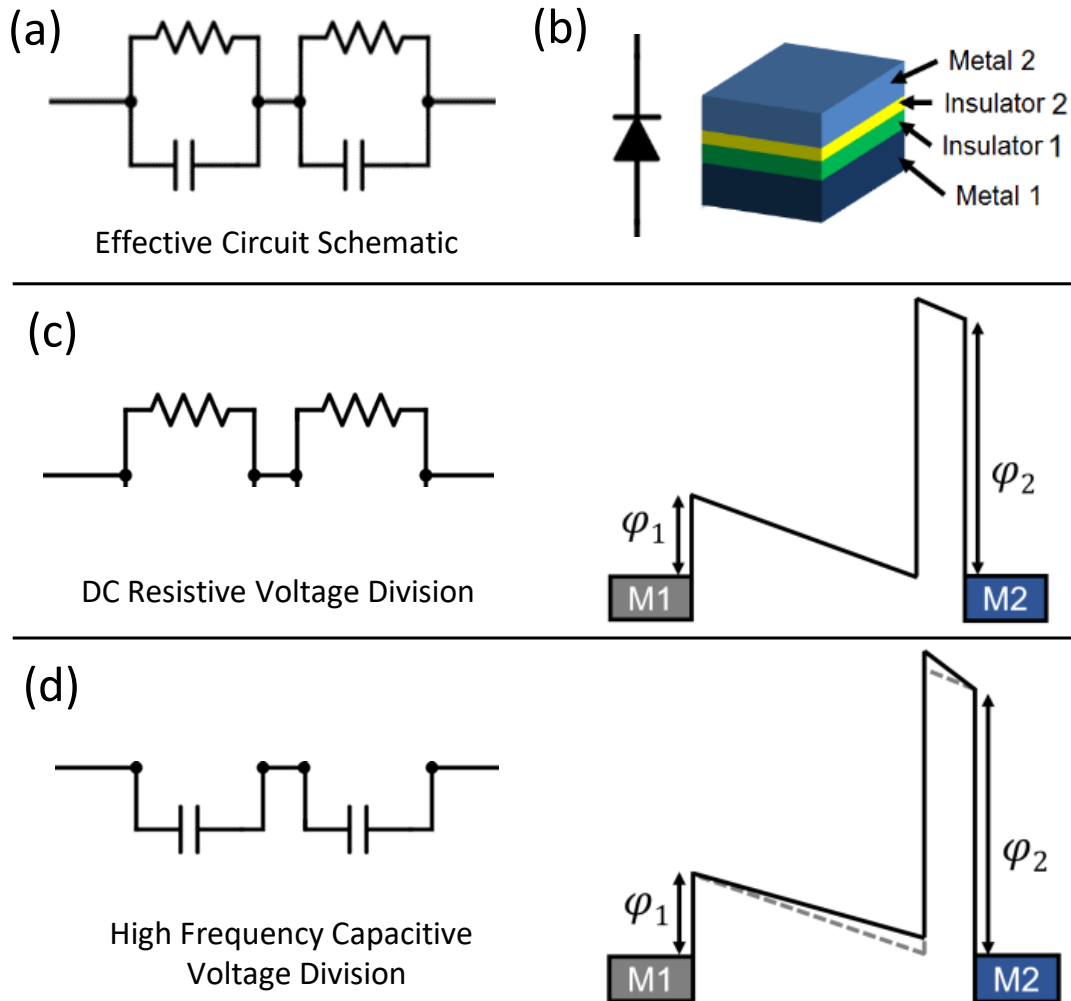
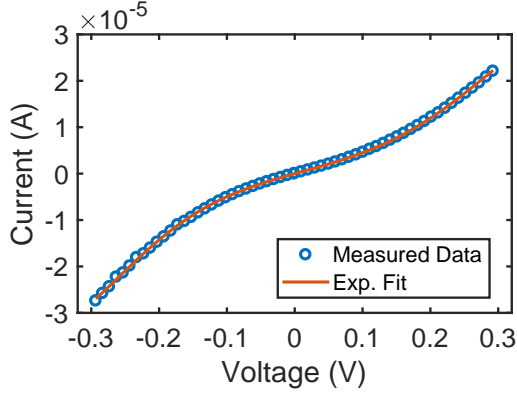
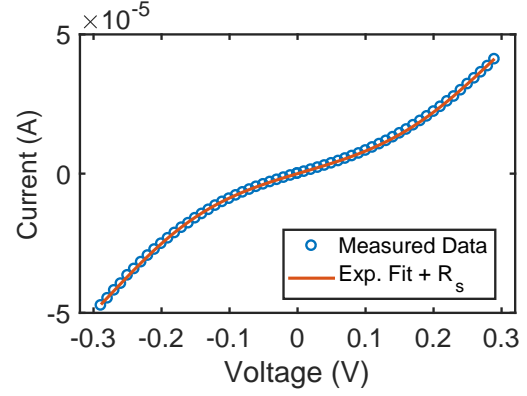
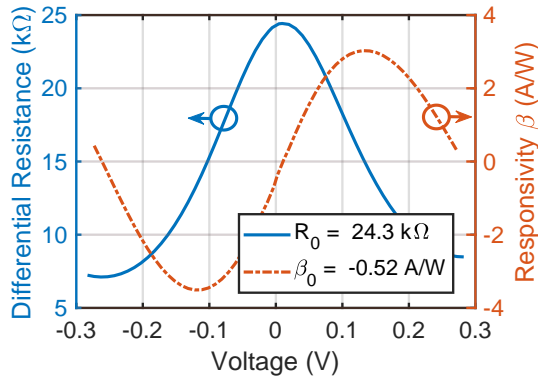
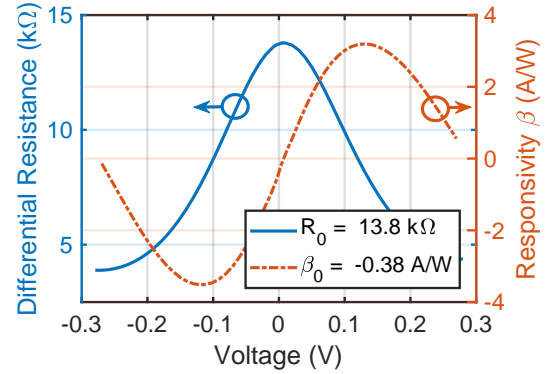
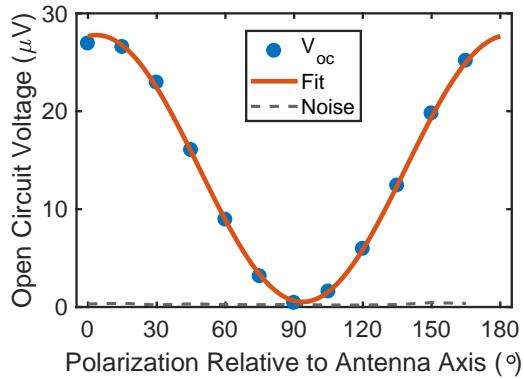


Figure 4.1: (a) Circuit diagram of a double insulator MIM diode where each oxide is represented by a resistor and a capacitor in parallel. (b) MIM diodes are made of two very thin insulators ( $<5$  nm) in series sandwiched between two metal contacts. (c) Resistive voltage division across insulators and band bending at DC. (d) Capacitive voltage division across insulators and band bending at high frequencies. The dotted line in the band diagram represents the DC bending due to resistive voltage division, for comparison.

barrier heights and dielectric constant ratios, we can take advantage of voltage division across the insulators to enhance the diode's nonlinearity (Grover and Moddel, 2013). For a double-insulator, as seen in Figures 4.1 (a) and (b), the two oxides are in series, and each oxide is represented with a simplified circuit diagram of a resistor and a capacitor in parallel. The oxides resistance depends on barrier height and oxide thickness, where a higher barrier or thicker oxide leads to a more resistive insulator, a higher applied voltage and more bending of the band. Capacitance is determined by the materials' dielectric constant, where a lower dielectric constant would result in a lower capacitance value and thus more voltage applied across it and more bending. Most MIM simulators described in literature (Grover and Moddel, 2012, Hashem et al., 2013, Hegyi et al., 2007, Herner et al., 2017, 2018, Mitrovic et al., 2018, Abdolkader et al., 2018), which are extensions of Simmons' tunneling model (Simmons, 1963), determine the voltage division across the insulators in DC based on dielectric constants and thicknesses. The flaw in this approach is that it does not take the tunneling resistance into account. This resistance, which depends on tunneling probability across oxides, governs voltage division at DC, where the capacitors are effectively open circuits, as depicted in Figure 4.1 (c). At frequencies above cutoff, where the magnitude of the capacitive reactances are smaller than the tunneling resistances, it is the capacitive voltage division that dominates and therefore using a dielectric constant-based voltage division approach is valid, as depicted in Figure 4.1 (d). This appears to be the reason that measured DC characteristics of double-insulator diodes do not match their simulated characteristics, and attempts to accurately design them have been unsuccessful. For the same reason, characteristics measured at DC have not correlated well with measured optical (AC) responses. We experimentally demonstrate and theoretically prove this concept by fabricating, measuring, and analyzing single and double-insulator MIM diodes.

## 4.2 Diode fabrication: MIM-1 and MI<sup>2</sup>M-1

MIM-1 and MI<sup>2</sup>M-1 consist of thermally evaporated Ni, DC sputtered NiO, RF sputtered Al<sub>2</sub>O<sub>3</sub> and evaporated Cr and Au, with thicknesses presented in Table 4.1. The Ni/NiO interface was chosen for its low barrier height of approximately 0.1 eV (Hobbs et al., 2005), which facilitates

(a) MIM-1  $I(V)$ (b) MI<sup>2</sup>M-1  $I(V)$ (c) MIM-1  $R_D(V)$  and  $\beta(V)$ (d) MI<sup>2</sup>M-1  $R_D(V)$  and  $\beta(V)$ 

(e) Ni/NiO/CrAu MIM

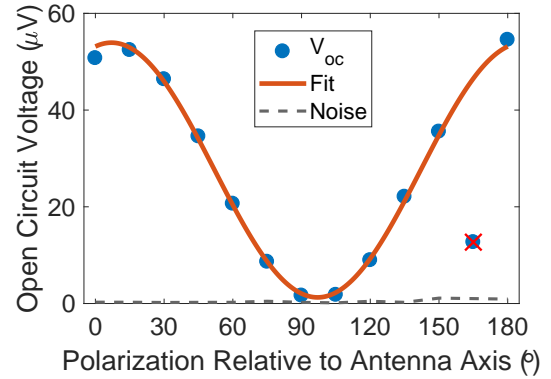
(f) Ni/NiO/Al<sub>2</sub>O<sub>3</sub>/CrAu MIIM

Figure 4.2: Current-voltage characteristics of (a) MIM-1 diode and (b) MI<sup>2</sup>M-1 diode. Differential resistance and responsivity curves with zero-bias resistance ( $R_0$ ) and zero-bias responsivity ( $\beta_0$ ) of (c) MIM-1 diode and (d) MI<sup>2</sup>M-1. Polarization angle dependence of  $V_{oc}$  measurements were performed for (e) MIM-1 and (f) MI<sup>2</sup>M-1, with a function generator duty cycle was 7%, and fit using a  $\cos^2$  polarization dependence relationship. The 165° data point was disregarded in the fit due to a measurement error. Measured data provided by Ayendra Weerakkody.

low resistance devices. The Au layer was chosen for its low loss tangent for optical measurements at 28 THz. To calculate the areas of the fabricated diodes, scanning electron microscopy (SEM) images were obtained, as shown in Figure 3.3a and discussed in Table 4.1. Figures 4.2 present the diodes DC current-voltage [ $I(V)$ ] characteristics and their calculated voltage-dependent responsivity and resistance plots. To assess the mid-infrared response of the fabricated rectenna system, both open circuit voltage ( $V_{oc}$ ) and short circuit current ( $I_{sc}$ ) were measured under  $10.6 \mu\text{m}$  illumination. MIM-1 and MI<sup>2</sup>M-1 were fabricated and measured by Ayendra Weerakkody.

Table 4.1: Diode material thicknesses and areas extracted from SEM images. Diodes fabricated by Ayendra Weerakkody.

Diode	Material set	Thickness (nm)					Area
		Ni	NiO	Al <sub>2</sub> O <sub>3</sub>	Cr	Au	
MIM-1	Ni/NiO/CrAu	35	6	-	3	37	$0.8 \times 250 \text{ nm} \times 90 \text{ nm}$
MI <sup>2</sup> M-1	Ni/NiO/Al <sub>2</sub> O <sub>3</sub> /CrAu	37	3.5	0.73	3	62	$0.8 \times 180 \text{ nm} \times 100 \text{ nm}$

Materials that have very low dielectric constants at terahertz frequencies, such as Al<sub>2</sub>O<sub>3</sub> (Kischkat et al., 2012), can enhance nonlinearity as well as reduce diode capacitance. In a single-insulator MIM diode, Al<sub>2</sub>O<sub>3</sub> forms a high barrier with most metals, thus increasing the diode resistance and lowering the cutoff frequency (Weerakkody et al., 2015, Bean et al., 2011, Jayaswal et al., 2018, Mitrovic et al., 2018, Bhatt et al., 2019). When combined with NiO, the overall diode DC resistance can be reduced (Weerakkody et al., 2019), but the challenge becomes optimizing the structure for high frequency rectification. This requires accurate knowledge of the shape of the diode’s energy band diagram.

### 4.3 DC and high frequency resistance

The best indication of a change in voltage division is the comparison between DC and high frequency resistances for our fabricated diodes. Because there is no change in distribution of voltage for a single-insulator MIM diode, there should be no changes in the measured zero-bias resistance between DC and high frequencies. Small variations are expected due to lead resistance from two-point probe optical measurements and laser instabilities due to beam wander. For a double-insulator

structure, the change in voltage division from resistive to capacitive across the insulators alters the band-bending and affects tunneling characteristics of the diode, thus resulting in two completely different  $I(V)$  characteristics at DC and high frequencies. To confirm this, we compare measured high frequency diode resistance ( $R_0^{HF}$ ) to DC resistance ( $R_0^{DC}$ ) by computing a percentage change ( $\Delta R_0$ ). Following the fact that the  $I(V)$  curve is linear in the low voltage range and using a clamping circuit model of the rectenna configuration discussed in Ch. 1 Fig. 1.5, we compute the high frequency diode resistance ( $R_0^{HF}$ ) as the ratio of  $V_{oc}$  and  $I_{sc}$  minus the lockin amplifier's 1 k $\Omega$  series resistance. The 5.8% change in  $R_0^{HF}$  of the MIM-1 diode (fabrication and measurements in Ch. 3) is attributed to a measured lead resistance of 600  $\Omega$  and a laser beam instability margin of error ( $<10\%$ ). The 70% increase in  $R_0^{HF}$  for the MI<sup>2</sup>M-1 structure (fabrication and measurements described in Ch. 3) can be explained neither by lead resistance nor by the laser instability margin of error alone. The only possible explanation for the increase in resistance is the change in voltage division across insulators, where more voltage is applied on Al<sub>2</sub>O<sub>3</sub>. In the following section, we investigate this theoretically by simulating the measured DC  $I(V)$  characteristics using a resistive voltage division approach and fitting the high frequency  $I(V)$  characteristics by a capacitive voltage division approach.

Table 4.2: Measured optical response values for the diodes at 10.6  $\mu\text{m}$ .

Diode	$V_{oc}$ ( $\mu\text{V}$ )	$I_{sc}$ (nA)	$R_0^{HF}$ ( $\Omega$ )	$R_0^{DC}$ ( $\Omega$ )	$\Delta R_0$ (%)
Ni/NiO/CrAu	11.2	0.42	25.7 k	24.3 k	5.8
Ni/NiO/Al <sub>2</sub> O <sub>3</sub> /CrAu	53.2	2.17	23.5 k	13.8 k	70

The complexity of modeling and analyzing multi-insulator MIM diodes increases with the number of oxides used. For a single insulator MIM, the process is simple, and an accurate fit between simulated and measured data can be achieved (Eliasson, 2001, Joshi, 2015, Abdolkader et al., 2018, Jayaswal et al., 2018, Weerakkody et al., 2019) since there are only three main parameters to change: the two barrier heights and the thickness of the oxide. These three parameters affect the shape of the  $I(V)$  curve of a single insulator, while electron mass and scattering losses in the oxide affect the magnitude. As the number of insulators increases, the number of fit parameters

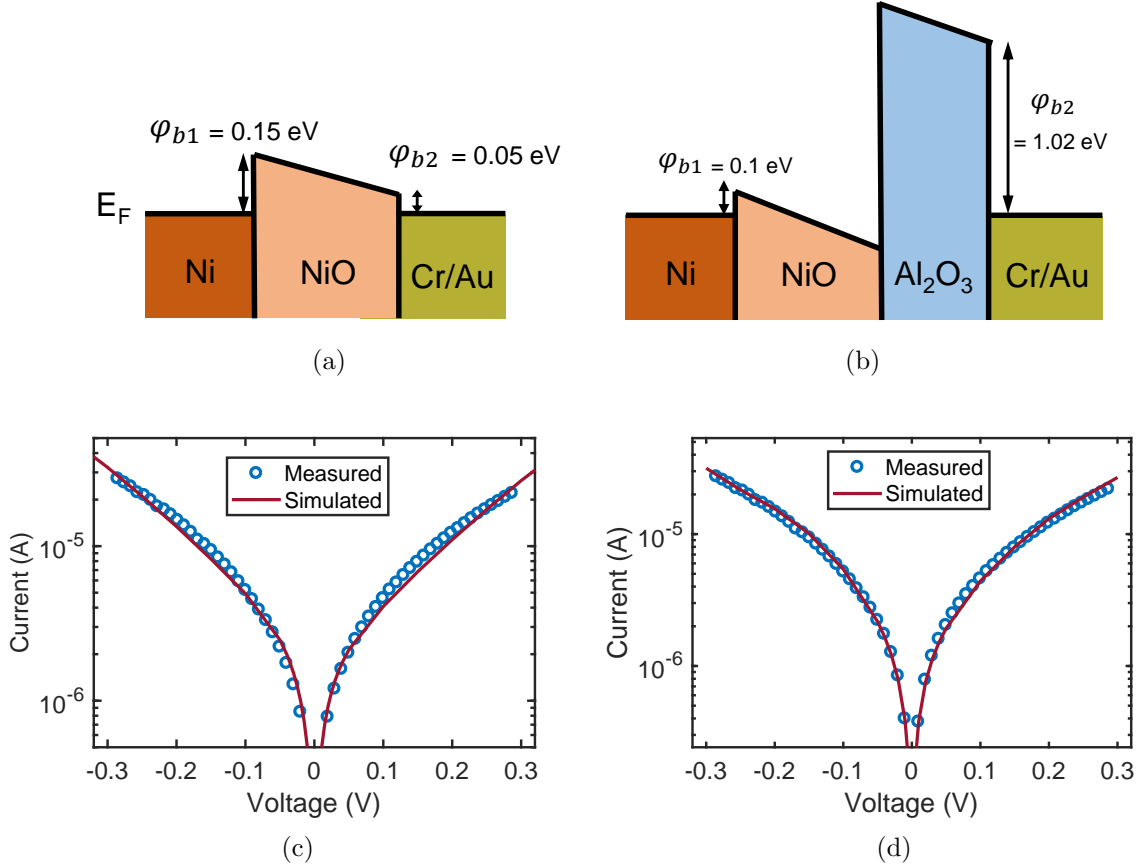


Figure 4.3: Band diagrams of (a) MIM-1 diode and (b) MIM-2 diode. (c) Diode simulation of the MIM-1 diode at DC to extract diode oxide thickness for dielectric constant estimation and Ni/NiO barrier information for the MI<sup>2</sup>M-1 diode analysis. (d) Diode simulation of the MI<sup>2</sup>M-1 diode at DC to predict high frequency  $I(V)$  characteristic.

increases linearly and voltage division across the insulators becomes a concern, thus increasing the difficulty of achieving an accurate fit (Herner et al., 2017, 2018, Hashem et al., 2013). To correctly fit our double-insulator diodes, we started by extracting as much information as possible about the structure: the thickness of both oxides using variable angle spectroscopic ellipsometry (VASE) and the Ni/NiO interface by building a single-insulator diode. We expect the oxide in our simulations to be thinner than the measured values because of surface non-uniformity across the diode junction and the fact that tunneling probability increases in thin regions over thick ones, thus dominating the diode  $I(V)$  characteristics. Figure 4.3c presents a good correspondence between our measured

and simulated single-insulator diode. We determined a Ni/NiO barrier height of 0.12 eV. This leaves the second barrier height and the voltage division across the insulators as parameters to vary for the double-insulator diode. Figure 4.3d presents simulation results that accurately fit measured data for MI<sup>2</sup>-1. The resistive voltage division ends up being 83% across NiO and 17% across Al<sub>2</sub>O<sub>3</sub>. Even in the presence of the high barrier formed between Al<sub>2</sub>O<sub>3</sub> and Cr/Au, a thinner Al<sub>2</sub>O<sub>3</sub> layer (0.73 nm) leads to a lower resistance oxide which results in a lower voltage applied across it.

#### 4.4 Band diagrams computation

##### Resistive voltage division

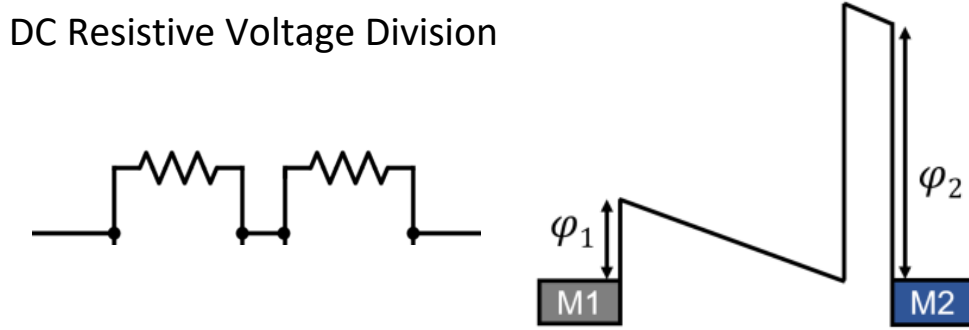


Figure 4.4: DC resistive voltage division simplified circuit model and corresponding band diagram.

To determine the energy-band profile at a certain voltage bias ( $V_D$ ) at DC, we first determine the resistive voltage division across each insulators. Figure 4.4 presents the simplified circuit diagram of the diode stack at DC as two resistors in series. The barrier heights ( $\phi$ ) are determined as

$$\phi = WF - EA \quad (4.1)$$

where WF is the metal's work function and EA is the oxide electron affinity. The voltage drop across each insulator is then determined as

$$\Delta V_j = (V_D - V_{bi}) \times (\%V_{RD}) \quad (4.2)$$

where  $V_{bi} = \phi_1 - \phi_2$  is the built-in potential and  $\%V_{RD}$  is the percentage voltage drop due to resistive voltage division. This is a fictitious resistance designed to fit the DC  $I(V)$ . The voltage drop ( $\Delta V_j$ ) represents the slope of the conduction band of the  $j^{th}$  insulator. Drawing the band diagram becomes a simple matter of

$$E_{BD} = E_F + \phi_1 - \sum_{j=1}^N \frac{\Delta V_j \times x}{t_j} \quad (4.3)$$

where  $E_{BD}$  is the energy band diagram vector in eV and  $x$  is the displacement vector and  $t_j$  is the thickness of the  $j^{th}$  oxide layer. For this particular structure, the thin  $\text{Al}_2\text{O}_3$  layer results in a lower applied voltage (17%) compared to the 83% applied across the thicker 3.5 nm of NiO, as illustrated in Fig. 4.4. The two competing effects of the thin and high barrier in  $\text{Al}_2\text{O}_3$  result in similar slope band bending as the lower barrier, thicker NiO insulator. Even though tunneling in an  $\text{MI}^2\text{M}$  diode goes through the entire structure and cannot be physically divided into two resistance values that sum to the total resistance, we were able to use this fictitious resistance method to achieve accurate fits of DC  $I(V)$  characteristics, as seen in Fig. 4.3c and Fig. 4.3d.

### Capacitive voltage division

#### High Frequency Capacitive Voltage Division

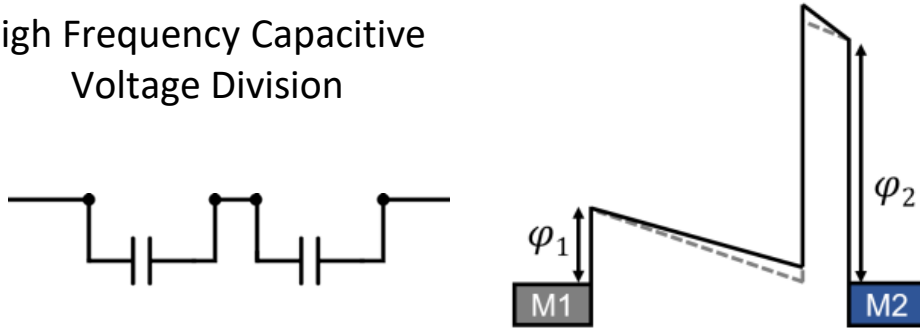


Figure 4.5: Capacitive voltage division circuit model and corresponding band diagram. The dashed lines represent the resistive voltage division band diagram for comparison.

For frequencies well above cutoff, voltage division is determined by the oxide capacitors, as

seen in Figure 4.5. The voltage drop across each insulator becomes

$$\Delta V_j = (V_D - V_{bi}) \times \frac{x_j/\epsilon_j}{\sum x_j/\epsilon_j} \quad (4.4)$$

where  $x_j$  and  $\epsilon_j$  represent the thickness and dielectric constant, respectively, of the  $j^{\text{th}}$  layer. The percentage voltage drop due to capacitive voltage division ( $V_{CD}$ ) is represented here as  $(x_j/\epsilon_j)/(\sum x_j/\epsilon_j)$ .

This comes from the voltage division across two capacitors in series where

$$C_{Total} = \frac{C_1 C_2}{C_1 + C_2} \quad (4.5)$$

For capacitive voltage division in the NiO/Al<sub>2</sub>O<sub>3</sub> structure, the lower Al<sub>2</sub>O<sub>3</sub> high frequency dielectric constant results in more voltage applied across Al<sub>2</sub>O<sub>3</sub> and more bending, as seen in Fig. 4.5. Similarly, the higher NiO dielectric constant results in lower voltage applied and thus, less bending compared to the resistive voltage division.

#### 4.5 Efficiency Calculations

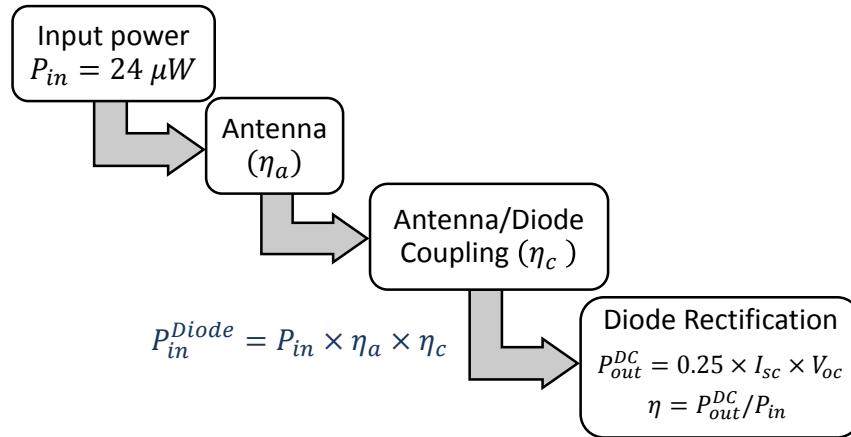


Figure 4.6: Output power and efficiency waterfall diagram

We use the waterfall diagram in Fig. 4.6 to calculate the projected diode efficiency of MIM-1 and MI<sup>2</sup>M-1 using DC resistance and responsivity values. The antenna efficiency ( $\eta_a$ ) is estimated to be 10% from COMSOL simulations. The antenna and diode coupling efficiency  $\eta_c$  is defined

here as

$$\eta_c = \frac{4R_a R_d}{(R_a + R_d)^2 + (X_a + X_d)^2} \quad (4.6)$$

where  $R_a$  and  $X_a$  are antenna resistance and reactance, respectively, estimated to be  $100 - j100\Omega$  from COMSOL simulations. The clamping circuit model of the rectenna configuration, where the lumped-element diode resistance and capacitance are considered to be in parallel, requires the calculation of the series equivalent impedance to use in Eq. 4.6. The  $R_d$  is the diode's equivalent real part of impedance, defined as

$$R_d = \frac{(R_0 X_D^2)}{(R_0^2 + X_D^2)} = \frac{R_0}{(\omega C R_0)^2 + 1} \quad (4.7)$$

and  $X_d$  is diode's equivalent imaginary part of impedance, defined as

$$X_d = \frac{-(R_0^2 X_D)}{(R_0^2 + X_D^2)} = \frac{-\omega C R_0^2}{(\omega C R_0)^2 + 1} \quad (4.8)$$

where  $R_0$  and  $X_D$  are diode's zero-bias resistance and reactance,  $\omega$  is the angular frequency and  $C$  is the diode's geometric capacitance.

Table 4.3: MIM-1 and MI<sup>2</sup>M-1 coupling efficiency calculations

Diode	$R_0$ (k $\Omega$ )	C (fF)	$R_d^*$ ( $\Omega$ )	$X_d$ ( $\Omega$ )	$\eta_c$ (%)
MIM-1	24.3	0.19	0.038	-30.3	0.056
MI <sup>2</sup> M-1	13.8	0.18	0.067	-30.4	0.099

The short circuit current ( $I_{sc}$ ) is calculated as

$$I_{sc} = \eta_a \eta_c P_{in} \beta_0 \quad (4.9)$$

The open circuit voltage ( $V_{oc}$ ) is calculated from  $I_{sc}$  multiplied by the zero-bias resistance ( $R_0^{DC}$ ).

Diode efficiency is then calculated as

$$\eta = \frac{P_{out}}{P_{in}} = \frac{(V_{oc} \times I_{sc})/4}{P_{in}} \quad (4.10)$$

Since the area of the rectenna is  $24 \mu\text{m}^2$  and the maximum beam intensity is  $1 \text{ W/mm}^2$ , the input power ( $P_{in}$ ) is calculated to be of  $24 \mu\text{W}$ . Here, we arbitrary assume the effective area of the

rectenna is the physical area, and account for antenna absorption efficiency later in the coefficient  $\eta_a$ . Table 6.8 presents the theoretically calculated efficiency number for both the single-insulator MIM diode and the double-insulator MIM diode. As can be seen from this, if we use DC values only to predict AC behavior, the single-insulator diode total efficiency ( $\eta = 1.14 \times 10^{-8}\%$ ) would surpass the double-insulator diode ( $\eta = 1.19 \times 10^{-8}\%$ ) by a factor of 1.04.

Table 4.4: Efficiency calculations using waterfall diagram with  $P_{in} = 24 \mu\text{m}$  and  $\eta_a = 10\%$

Diode	$\eta_c(\%)$	$\beta_0$ (A/W)	$I_{sc}$ (nA)	$R_0(\Omega)$	$V_{oc}$ ( $\mu\text{V}$ )	$\eta(\%)$
MIM-1	0.056	0.52	0.70	24.3 k	16.9	$1.23 \times 10^{-8}$
MI <sup>2</sup> M-1	0.099	0.38	0.91	13.8 k	12.5	$1.18 \times 10^{-8}$

We therefore use measured  $I_{sc}$  and  $V_{oc}$  values to demonstrate how erroneous using DC values for calculations is and determine the correct efficiency values (presented in table 4.5). The  $R_0^{HF}$  is calculated as

$$R_0^{HF} = \left( \frac{V_{oc}}{I_{sc}} \right) - R_{Lockin} - R_{lead} \quad (4.11)$$

where  $R_{Lockin}$  is the lockin amplifier's resistance equal to 1 k $\Omega$  and  $R_{lead}$  is the lead resistance equal to 600  $\Omega$ . The efficiency is then computed as

$$\eta = \frac{P_{out}}{P_{in}} = \frac{(V_{oc}^2)/(4 \times R_0^{HF})}{P_{in}} \quad (4.12)$$

The measured double-insulator diode efficiency surpasses that of the single insulator by a factor of 25.

Table 4.5: Efficiency calculations from experimental results

Diode	$V_{oc}$ ( $\mu\text{V}$ )	$I_{sc}$ (nA)	$R_0^{HF}(\Omega)$	$\eta$ (%)
MIM-1	11.2	0.42	25.1 k	$5.2 \times 10^{-9}$
MI <sup>2</sup> M-1	53.2	2.17	22.9 k	$1.3 \times 10^{-7}$

## 4.6 High Frequency $I(V)$

To generate the high frequency  $I(V)$  characteristic of the diode, we used computed material parameters (see Appendix A) and changed the voltage division to become dependent on dielectric

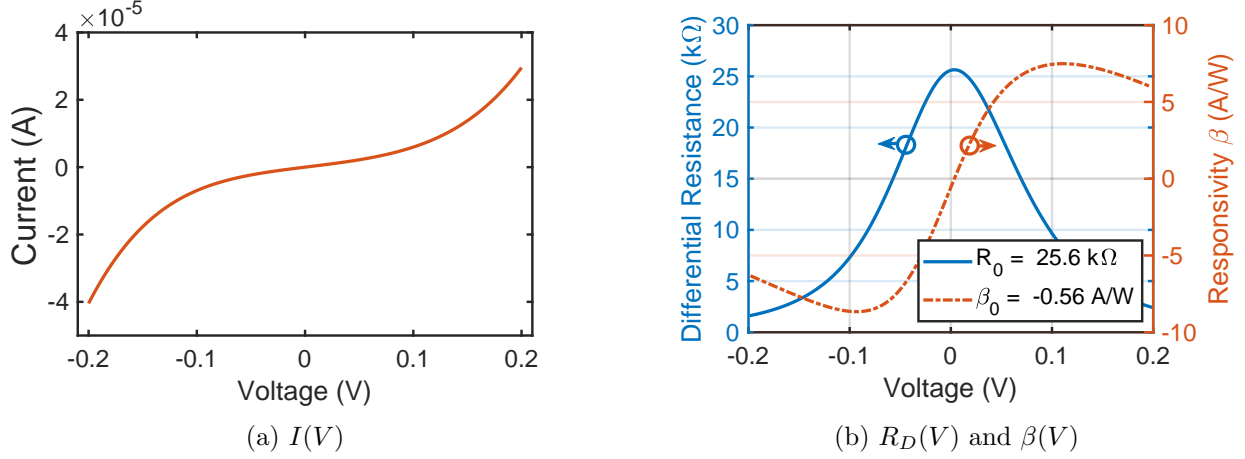


Figure 4.7: MI<sup>2</sup>M-1 diode simulated 28 THz characteristics.(a) Current-voltage characteristics and (b) differential resistance and responsivity curves with zero-bias resistance ( $R_0$ ) and zero-bias responsivity ( $\beta_0$ ).

constant. The estimated dielectric constants from our high frequency fit for NiO and Al<sub>2</sub>O<sub>3</sub> were 7 and 3.85, respectively. The capacitive voltage division results in 73% across NiO and 27% with a high frequency resistance of 25.6 k $\Omega$ , as seen in Figure 4.7. The measured high frequency resistance of 24.5 k $\Omega$  is within a 12% error margin. All this makes it clear that voltage division changes from resistive to capacitive are what drive the change in resistance in this diode. It is also confirmation that DC diode characteristics cannot be used to predict high frequency  $I(V)$  characteristics. For our fabricated diodes, this is evident from the efficiency calculations of both diodes where the double-insulator diode's measured efficiency is approximately 25 times larger than that of the single-insulator, whereas based on the DC characteristics, the single-insulator efficiency would surpass the double-insulator's by a factor of 1.04.

At 28 THz, the tunneling resistance of the diode is 750 times larger than the capacitive reactance, which allows us to use a purely capacitive voltage division at this frequency. As we transition from high frequencies that are below cutoff to DC, the voltage division across the insulators becomes a combination of resistive and capacitive voltage division, and determining it theoretically becomes difficult. The band bending of the structure is then affected by the barrier height, thickness and material dielectric constant, which are all competing effects when determining the voltage division.

Depending on the material properties and the changes with frequency, the diode could improve or degrade at high frequencies. With future measurement of dielectric constants at 28 THz, we will be able to further quantify how much of the simulation deviation is from voltage division and how much is from other frequency parameters that are currently unaccounted for.

## 4.7 Conclusions

Research groups working with MIM diodes for optical rectennas typically use DC characteristics to compare diodes behavior when operated at high (THz) frequencies. This is valid for single-insulators, but for multiple-insulator diodes, the  $I(V)$  characteristics, and therefore the resistance and responsivity curves, change. In analyzing double-insulator MIM diodes, the correct method of dividing the voltage across the two insulator layers in DC is through resistive voltage division, where each oxide is modeled by a resistance. The simulated oxide resistances are fictitious elements used to achieve resistive voltage division for tunneling simulations. At frequencies higher than the RC cutoff, the commonly used dielectric-dependent capacitive voltage division method still applies. While a single-insulator diode  $I(V)$  curve remains almost the same at DC and high frequencies, the  $I(V)$  characteristic of a double insulator diode can change dramatically. The change is evident in the zero-bias resistance of a double-insulator diode changing by 70% between DC and high frequency as opposed to the 5.8% change for the single-insulator diode. The erroneous assumption that the DC and high-frequency  $I(V)$  characteristics are the same has led to incorrect projections of device operating properties at high frequency, and puzzling DC  $I(V)$  curves that cannot be reconciled with designs based on simulations that assume capacitive voltage division.

## CHAPTER 5

### DEMONSTRATION OF RESONANT TUNNELING EFFECTS IN METAL-DOUBLE-INSULATOR-METAL (MI<sup>2</sup>M) DIODES

Resonant tunneling in metal-double-insulator-metal (MI<sup>2</sup>M) diodes has drawn significant attention in recent years. However, until now, there have been no experimental reports of resonant tunneling effects at the low voltages needed for high frequency rectenna applications. Using quantum-well engineering, we demonstrate the effects of resonant tunneling in MI<sup>2</sup>M structures to achieve low resistance and high responsivity simultaneously. By varying the thickness of insulators to create deep quantum wells, we show that quasi-bound states can be reached at near-zero bias, where diodes self-bias when driven by antennas illuminated at 30 THz. The total energy conversion efficiency is improved by more than a factor of 100 over the current state-of-the-art, offering the possibility of engineering efficient rectennas for waste heat harvesting. This study was motivated by simulation which were later verified by experimental results. Work carried out in this chapter was performed in close collaboration with Ayendra Weerakkody.

#### 5.1 Introduction

The challenge in designing diodes suitable for high frequency applications is in achieving low resistance and high responsivity simultaneously. Common methods of increasing responsivity, such as increasing oxide thicknesses or barrier heights, result in an increase in resistance. Herner et al. experimentally verify this responsivity/resistance trade-off by fabricating and measuring hundreds of Co/Co<sub>3</sub>O<sub>4</sub>/TiO<sub>2</sub>/Ti MI<sup>2</sup>M diodes (Fig. 5.1 (a)), where higher responsivity values came at the

expense of higher resistance values (Herner et al., 2018). The spread seen in Fig. 5.1 (a) is due to thickness variations across the wafer, as verified by simulations in Fig. 5.1 (b). The same responsivity-resistance trend was observed by Bean et al. for MIM diodes (Bean et al., 2011). One solution to breaking this established trend is resonant tunneling, which provides improved nonlinearity with a drop in diode resistance (Eliasson and Moddel, 2003, Grover and Moddel, 2012). For almost two decades, numerous theoretical and experimental studies were performed to explore the possibility of achieving resonant tunneling in MIM structures to use in optical rectennas (Apell and Penn, 1992, Eliasson, 2001, Eliasson and Moddel, 2003, Grover and Moddel, 2012, Maraghechi et al., 2012, Weerakkody et al., 2015). All experimental observations of resonant tunneling in MIM structures were made at high voltages ( $> 1$  V), rendering the structures unusable for energy harvesting where self-biasing occurs at  $\sim 1$  mV (Drury and Ishii, 1980, Belenov et al., 1982, Hu and Stapleton, 1991, Watanabe et al., 1993, Sadakuni et al., 2009, Maraghechi et al., 2012, Weerakkody et al., 2015). These groups were not successful in observing resonant tunneling at low voltages due to fabrication limitations and interface quality engineering challenges at metal-dielectric and dielectric-dielectric interfaces. In this chapter, we demonstrate for the first time resonant tunneling effects in MI<sup>2</sup>M diodes, where a reduction in resistance is observed with an increase in responsivity.

## 5.2 Breaking the responsivity/resistance trend using resonant tunneling

Resonant tunneling, where electrons tunnel through discrete quasi-bound states in a triangular quantum well, has the potential of breaking the responsivity/resistance trade-off. We first observed this effect in Co/Co<sub>3</sub>O<sub>4</sub>/TiO<sub>2</sub>/Ti diode simulations by varying only the thickness of the first oxide (Co<sub>3</sub>O<sub>4</sub>), presented in Fig. 5.1 (c). Measured diodes published in literature, such as Herner et al.'s work, typically take on the simulated responsivity/resistance data spread presented in Fig. 5.2 (a), where the thickness ratio of 1:1 is chosen for the two oxides and a  $\pm 4$  Å thickness variation was expected across the wafer (Herner et al., 2018). The dominant tunneling mechanism in such a structure, represented as M<sub>1</sub>/Ox<sub>1</sub>/Ox<sub>2</sub>/M<sub>2</sub>, is Fowler-Nordheim tunneling in the first oxide (Ox<sub>1</sub>) and direct tunneling in the second oxide (Ox<sub>2</sub>), as seen in the energy-band lineup

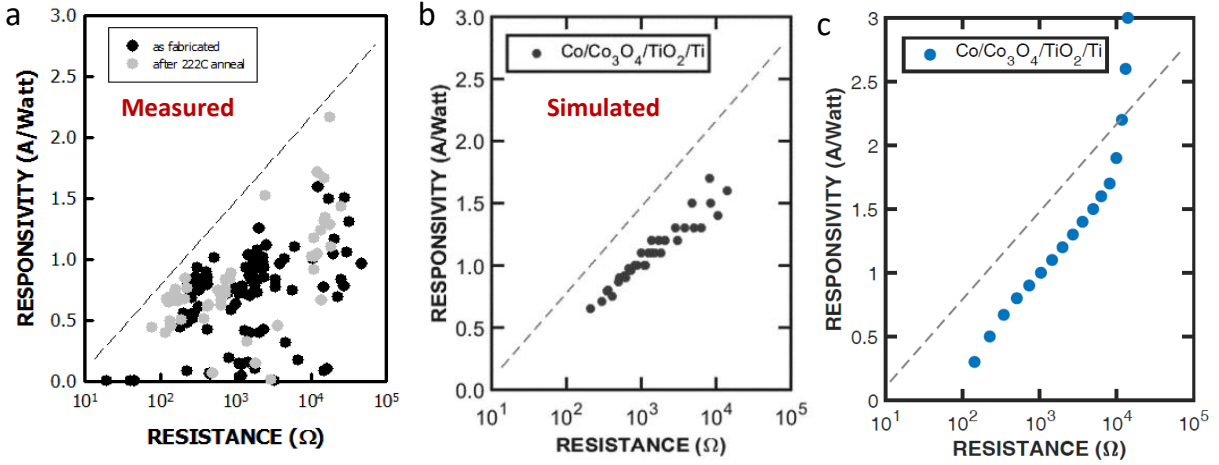


Figure 5.1: Responsivity/resistance trade-off. Plot of resistance and responsivity at 0 V of (a) fabricated  $\text{Co}/\text{Co}_3\text{O}_4/\text{TiO}_2/\text{Ti}$  diodes and (b) simulated  $\text{Co}/\text{Co}_3\text{O}_4/\text{TiO}_2/\text{Ti}$  diodes. The grey dashed line presents the expected trade-off between responsivity and resistance (Herner et al., 2018). (c) Simulated responsivity resistance trend for a  $\text{Co}/\text{Co}_3\text{O}_4/\text{TiO}_2/\text{Ti}$  diode.  $\text{Co}_3\text{O}_4$  Thickness was varied from 0.1 to 2 nm while maintaining the  $\text{TiO}_2$  thickness of 1.1 nm.

presented in Fig. 5.2 (b). We looked at the effects of varying the thickness of  $\text{Ox}_1$  in the range of 1 to 20 Å, while maintaining the thickness of  $\text{Ox}_2$  fixed to 1 nm. Increasing oxide thickness and tunneling distance increases diode asymmetry, and thus responsivity, at the price of increased resistance. Based on the hundreds of diodes fabricated and measured in the Moddel lab, as well as trends observed by Herner et al. (Herner et al., 2018) and Bean et al. (Bean et al., 2011), we expected responsivity to increase with resistance as oxide thickness was increased. Contrary to expectations, as the thickness of  $\text{Ox}_1$  increased beyond 1.7 nm, resistance dropped while responsivity continued to increase (solid line in Fig. 5.2 (a)). This puzzling trend has never been predicted theoretically with variations in thickness or for diode figures of merit (responsivity and resistance) near 0 bias.

When the quasi-bound state is not aligned with the Fermi level of  $\text{M}_1$ , electrons drift or ballistically traverse with an energy at or above the conduction band edge of  $\text{Ox}_1$ . Resonant tunneling occurs near zero-bias when the Fermi level of the first metal is aligned with quasi-bound state, as can be seen in Fig. 5.2 (c). Electrons with energies close to the quasi-bound states in the quantum well can traverse the structure without any reflections, thus producing a higher current

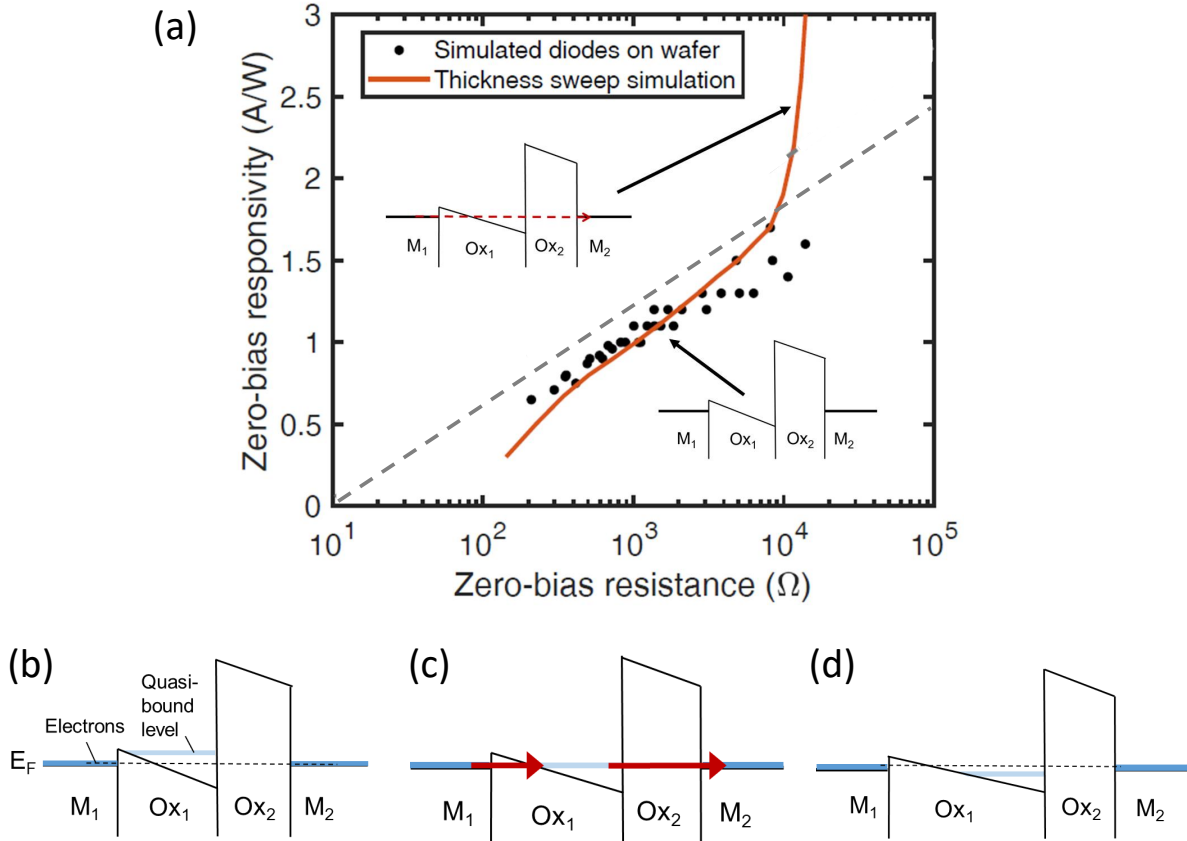


Figure 5.2: (a) Plot of responsivity/resistance trade-off simulated in MI<sup>2</sup>M diodes at a bias of 0 V for a material set of M<sub>1</sub>/Ox<sub>1</sub>/Ox<sub>2</sub>/M<sub>2</sub>, where M<sub>1</sub> and M<sub>2</sub> form the top and bottom metal electrodes of the diodes and Ox<sub>1</sub> and Ox<sub>2</sub> form the two oxides of the diode. The grey dashed line presents a rough expected trade-off between responsivity and resistance. Measured diodes published in literature typically take on the data spread presented in the dots. The solid line depicts results for varying thickness of Ox<sub>1</sub> while maintaining a constant thickness of Ox<sub>2</sub>. Energy-band diagrams of a MI<sup>2</sup>M structure with varying Ox<sub>1</sub>:Ox<sub>2</sub> ratios of (b) 1:1 (c) 2:1 and (d) 3:1 simulated to explain resonant tunneling. The dashed line represents electron tunneling from the Fermi level of M<sub>1</sub> to M<sub>2</sub>. In (b) and (d), Fowler-Nordheim tunneling occurs through Ox<sub>1</sub> and direct tunneling through Ox<sub>2</sub>. In (c), electrons tunnel through the quasi-bound state present in the triangular quantum well, which enhances tunneling probability, increases current and responsivity and decreases resistance.

and lower resistance than structures without quasi-bound states, as will be later demonstrated experimentally and theoretically in this chapter. As we continue increasing the thickness, Fig. 5.2 (d), the Fermi level is no longer aligned with the quasi-bound state and hence, diode resistance increases again. From simulations, we were able to obtain desired band diagram properties necessary

to observe resonant tunneling behavior: the low barrier height dielectric should be thicker than the high barrier height dielectric, fostering a well in between. When the diode is unbiased in DC, the band structure reaches thermodynamic equilibrium by aligning the Fermi levels of the two metal electrodes and band-bending between the two insulators is determined by tunneling resistance at DC, which depends on barrier height and oxide thickness. As the thickness of the low barrier height oxide is increases, more voltage is applied across it, resulting in more band bending of that oxide compared to that of the high barrier height oxide, and a deep and broad well, thus allowing a quasi-bound state to exist closer to self-bias voltage. Varying the thickness of only Ox<sub>1</sub> allowed us to change the width and depth of the quantum well which enabled us to engineer the band line-up to achieve resonant tunneling close to self-bias voltage. The band bending of the oxides depends on the voltage division between the two oxides, which is governed by tunneling resistance in DC and capacitance at high frequencies (Belkadi et al., 2018), discussed in Ch. 4.

Following these design rules, we were able to observe resonant tunneling effects experimentally in Ni/NiO/Al<sub>2</sub>O<sub>3</sub>/Cr/Au diodes, as evidenced by a non-monotonic responsivity-resistance relationship at zero-bias shown in Fig. 5.3. We fabricated four Ni/NiO/Al<sub>2</sub>O<sub>3</sub>/Cr/Au diodes with nominal NiO thicknesses of 3, 4, 5 and 6 nm, while maintaining the nominal thickness of Al<sub>2</sub>O<sub>3</sub> at 1.3 nm. In MI<sup>2</sup>M diodes, thickness ratio variations produce variations in the DC  $I(V)$  characteristics by altering the shape of the triangular barrier. A resonant well is formed between NiO and Al<sub>2</sub>O<sub>3</sub> and by increasing the thickness of NiO, the higher electron affinity insulator, the band bending becomes sufficient to form a deep and broad quantum well. As shown from the relationship between mean values (solid black line in Fig. 5.3), responsivity increases when thickness is increased from 3 to 5 nm while resistance drops for the 4 nm structure before increasing for the 5 nm structure. Data presented includes diodes fabricated from three different wafers. This unprecedented experimental relationship can be explained only by resonant tunneling effects. It serves as a demonstration of the enhancement achieved in MI<sup>2</sup>M diodes, where a reduction in resistance is observed with a concomitant increase in responsivity and nonlinearity. The reason resonant tunneling diodes have been hard to demonstrate is the difficulty of building low-barrier height diodes with wells deep

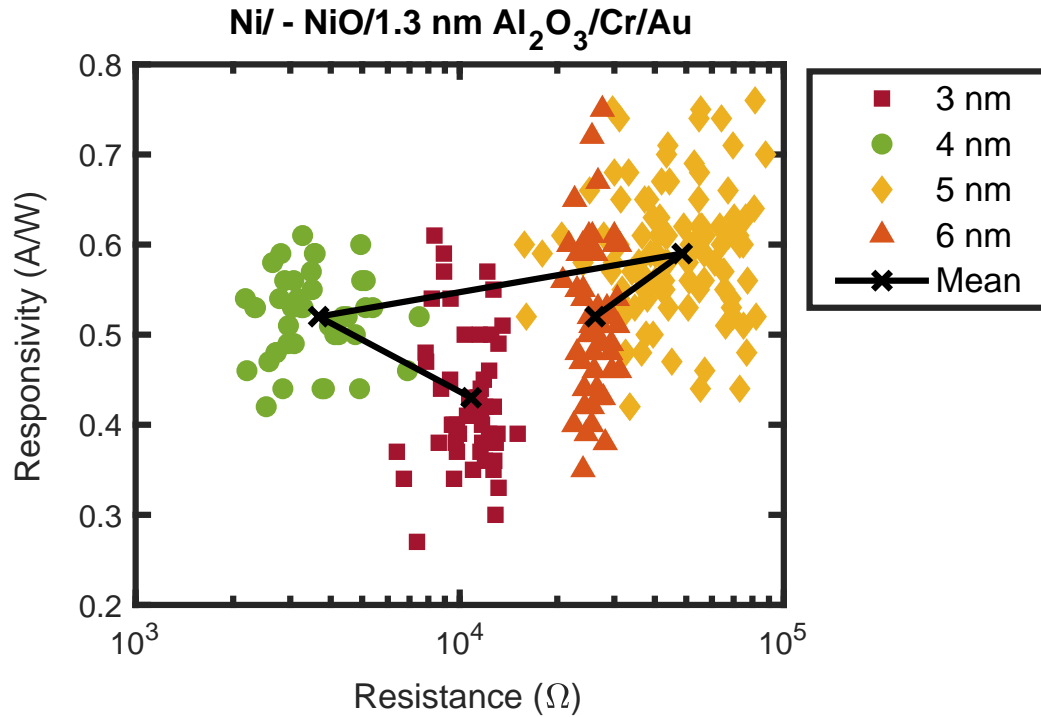


Figure 5.3: Measured responsivity vs. resistance plot of thickness study for Ni/NiO/Al<sub>2</sub>O<sub>3</sub>/Cr/Au diodes. MI<sup>2</sup>M diodes were fabricated by Ayendra Weerakkody for four nominal NiO thicknesses (3 to 6 nm in steps of 1 nm), while maintaining the nominal thickness of Al<sub>2</sub>O<sub>3</sub> at 1.3 nm. The diodes are normalized based on area and filtered to remove extreme outliers. Data presented in this figure includes diodes from three different wafers. As shown from the relationship between mean values (solid black line), responsivity increases when thickness is increased from 3 to 5 nm while resistance drops for the 4 nm structure before increasing again for the 5 nm structure.

and wide enough at low voltages to accommodate bound states and fabrication limitations such as sub-nm control of thicknesses. In this work, we engineered the band line-up of our structures to achieve resonant tunneling close to zero-bias in DC, with the expectation of observing enhanced high frequency response over diodes without resonant tunneling, when the diode self-biases. We were able to observe resonant tunneling due to our low diode barrier created between Ni and NiO ( $\sim 0.15$  eV) as well as our careful control of NiO and Al<sub>2</sub>O<sub>3</sub> thicknesses.

### 5.3 Simulation-based resonant tunneling analysis

The wide spread in experimental resistance and responsivity values, as seen in Fig. 5.1 (b), led us to simulate the thickness variation across our structures and determine whether the trend observed was primarily due to resonant tunneling or something else. We used a quantum mechanical transfer-matrix method diode simulator that accounts for resonant tunneling in a multi-barrier structure to study our MI<sup>2</sup>M diodes (Weiss et al., 2004, Grover and Modell, 2012). In Fig. 5.4 (a), we show the measured and simulated DC  $I(V)$  characteristics of the MI<sup>2</sup>M-2 (Ni/4 nm NiO/1 nm Al<sub>2</sub>O<sub>3</sub>/Cr/Au) diode.

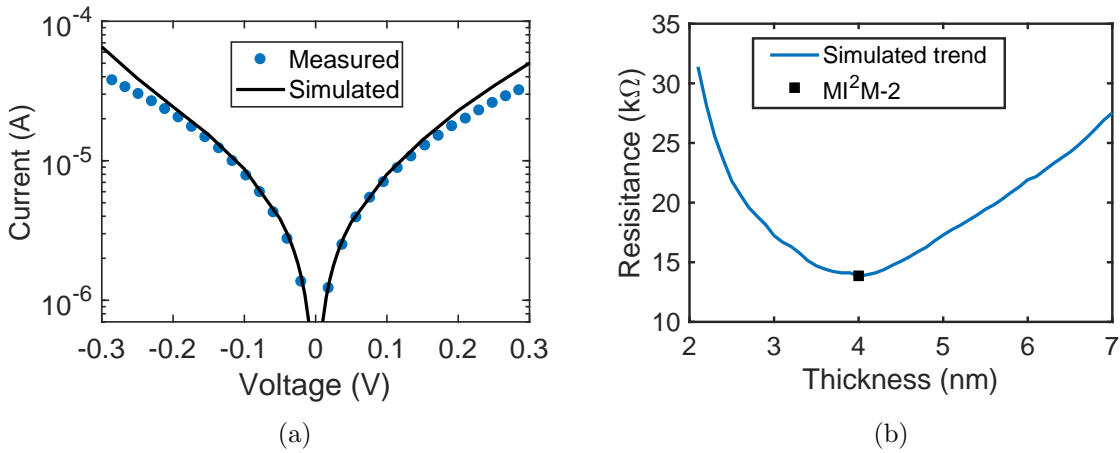


Figure 5.4: MI<sup>2</sup>M-2 (Ni/4 nm NiO/1 nm Al<sub>2</sub>O<sub>3</sub>/Cr/Au) diode simulation analysis (a) Measured (blue circles) and simulated (solid black line)  $I(V)$  characteristics of MI<sup>2</sup>M-2 diode. (b) Simulated resistance vs. NiO thickness (solid blue line) with the measured MI<sup>2</sup>M-2 diode (black square) used in the fit.

The MI<sup>2</sup>M diode areas ( $\sim 0.035 \mu\text{m}^2$ ) and nominal oxide thicknesses were measured using scanning electron microscopy (SEM) and variable-angle spectroscopic ellipsometry (VASE), respectively. The measured oxide thicknesses were used as a starting point for the simulations, and were varied, along with material properties such as barrier heights and effective mass, to achieve the best fit of the measured  $I(V)$  characteristics. We extracted thicknesses of 4 nm and 1 nm for NiO and Al<sub>2</sub>O<sub>3</sub>, respectively. Because the magnetic NiO target suffered from Ti target poisoning, the sputtered NiO used in these diodes is a hybrid oxide with unknown properties. This explains the

difficulty in fitting the fabricated diode accurately with a double insulator simulator at voltages above 150 mV (Fig. 5.4 (a)). A more accurate approach would be to simulate a triple insulator with an interfacial layer (a NiO/Ti hybrid layer), but because our application focuses on operation near zero-bias, the current fit works well to analyze diode operation at voltages lower than 100 mV.

We use the simulation fitting parameters of the measured 4 nm structure (Fig. 5.4 (a)) to investigate the relationship between zero-bias resistance and NiO thickness, by simulating oxide thickness variations from 2 to 7 nm (Fig. 5.4 (b)). The measured 4 nm diode is represented by a black square in Fig. 5.4 (b). The results show that contrary to the expected increase in resistance with thickness, a drop in resistance is observed from 2 to 4 nm. Increasing the thickness of the high electron affinity oxide (NiO) increases the depth and width of the well formed between NiO and  $\text{Al}_2\text{O}_3$ , and thus allows electrons to reach and tunnel through quasi-bound states in the well. Fig. 5.5 (a) presents the simulated trend with the measured diodes. The grey region shows a simulated 20% thickness variation of  $\text{Al}_2\text{O}_3$  across the wafer. That is a thickness variation of  $\pm 2 \text{ \AA}$ , for an  $\text{Al}_2\text{O}_3$  total thickness of 8  $\text{ \AA}$  to 12  $\text{ \AA}$ , as shown in Fig. 5.5b. Resistance variation is also attributed to variations in junction areas of 10% seen in SEM measurements across wafer pieces.

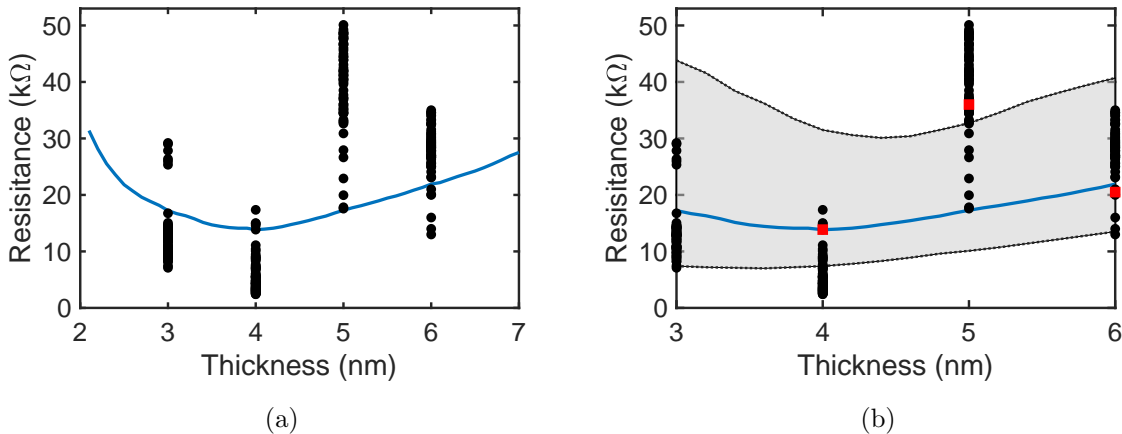


Figure 5.5: (a) Simulated Resistance vs. NiO thickness trend (solid blue line) with measured data from three wafers (solid black dots). (b) The gray shaded area represents simulated thickness variation of 2  $\text{ \AA}$  for an  $\text{Al}_2\text{O}_3$  thickness of 1 nm. The red squares present MI<sup>2</sup>M-2 (4 nm), MI<sup>2</sup>M-2 (5 nm) and MI<sup>2</sup>M-2 (6 nm) measured optically later in the chapter. Measured data provided by Ayendra Weerakkody.

What these simulations were unable to explain through  $\text{Al}_2\text{O}_3$  thickness and area variations is the 4 nm and 5 nm data, where the 4 nm and 5 nm NiO diodes exhibited lower and higher resistance than expected, respectively. One possible explanation is thickness dependent material properties, where NiO chemical compositions varies with thickness (Ratcliff et al., 2011). To verify this, Weerakkody performed x-ray photoelectron spectroscopy (XPS) measurements of 20 nm NiO and 2 nm NiO deposited on 20 nm  $\text{Al}_2\text{O}_3$ . We found that the Ni 2p XPS spectrum shoulder peak (855.42 eV) of the 2 nm NiO sample is more pronounced than the NiO main peak (854.19 eV). A contributing factor to the formation of a shoulder in Ni 2p spectra of thin NiO is that when the thickness of NiO in the order of a few monolayers, growth of NiO happens through small islands with determined heights ascribed to the formation of many nucleation centers at the grain boundaries of the polycrystalline materials (Ratcliff et al., 2011). When NiO thickness is varied, the shoulder peak intensity of Ni 2p spectra varies, implying a thickness dependent NiO island formation. The spread in resistance values is thus attributed to a combination of thickness-sensitive interfacial layer propitiates (Shih et al., 2014, Weerakkody, 2016) and thickness-dependent NiO chemical composition.

### 5.3.1 Maintaining the correct thickness ratio

As the thickness of  $\text{Al}_2\text{O}_3$  is varied, the position of the lowest resistance value shifts towards higher NiO thicknesses and is more pronounced, as seen in both Fig. 5.5 and Fig. 5.6. In Fig. 5.5, a 2 Å change in  $\text{Al}_2\text{O}_3$  thickness results in a shift in the valley from NiO thickness of 4 nm to ~ 4.5 nm. Similarly, in Fig. 5.6, a 5 Å change in  $\text{Al}_2\text{O}_3$  thickness results in a shift in the valley from NiO thickness of 4 nm to ~ 5 nm. This is important as it indicates the same dip in resistance can be achieved with lower zero-bias resistance values by maintaining the NiO: $\text{Al}_2\text{O}_3$  thickness ratio constant. For this particular material set, it is expected to see a similar dip in resistance at a ratio of 3:0.75 nm.

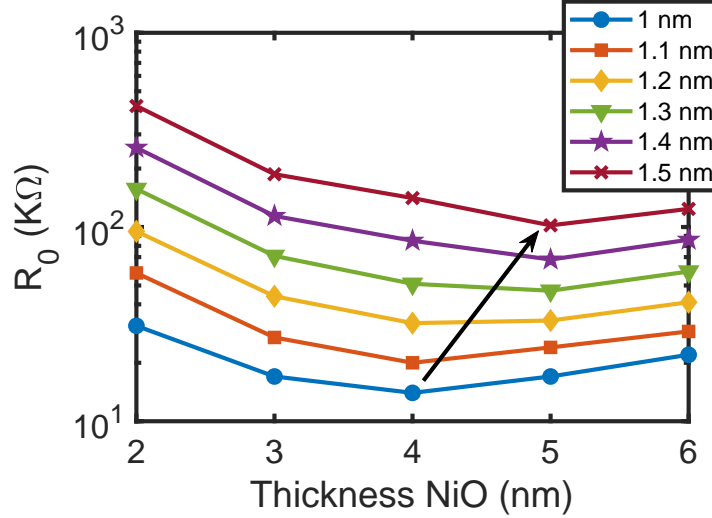


Figure 5.6: Zero-bias resistance ( $R_0$ ) as a function of NiO thickness for different  $\text{Al}_2\text{O}_3$  thicknesses. The black arrow indicates a shift in the valley that occurs as  $\text{Al}_2\text{O}_3$  thickness is increased to maintain the ratio at close to 1:0.25 nm of NiO to  $\text{Al}_2\text{O}_3$ .

### 5.3.2 Transmittance analysis

Transmittance is defined as the tunneling probability of electrons multiplied by the Fermi-Dirac distribution (Weerakkody, 2016). Tunneling probability  $T(E)$  is the ratio of outgoing to incoming quantum mechanical probability current density.  $T(E)$  is the results of electron wave function interference with itself in the quantum well through reflections. At off-resonance, this interference is destructive and  $T(E)$  is very small. At energies that align with the quantum well's quasi-bound states, the interference is constructive which results in the cancellation of reflected waves and the enhancement of transmitted one. Thus, resonant tunneling occurs when the majority of electrons tunnel with a  $T(E)$  that sharply peaks to unity at these specific energies. Figure 5.7 presents the tunneling probability as a function of energy and band diagrams of 4, 5 and 6 nm NiO Ni/NiO/ $\text{Al}_2\text{O}_3$ /Cr/Au simulated structures. The simulator uses a transfer matrix method to solve a time-independent Schrödinger equation and calculate transmission amplitudes, with a Hamiltonian matrix constructed to determine the bound states in a quantum well (Grover, 2011). The 4 nm structures  $T(E)$  peaks close to 0.1 eV, the 5 nm close to 0.09 eV and the 6 nm close to 0.13 eV as presented in Fig. 5.7 (d).

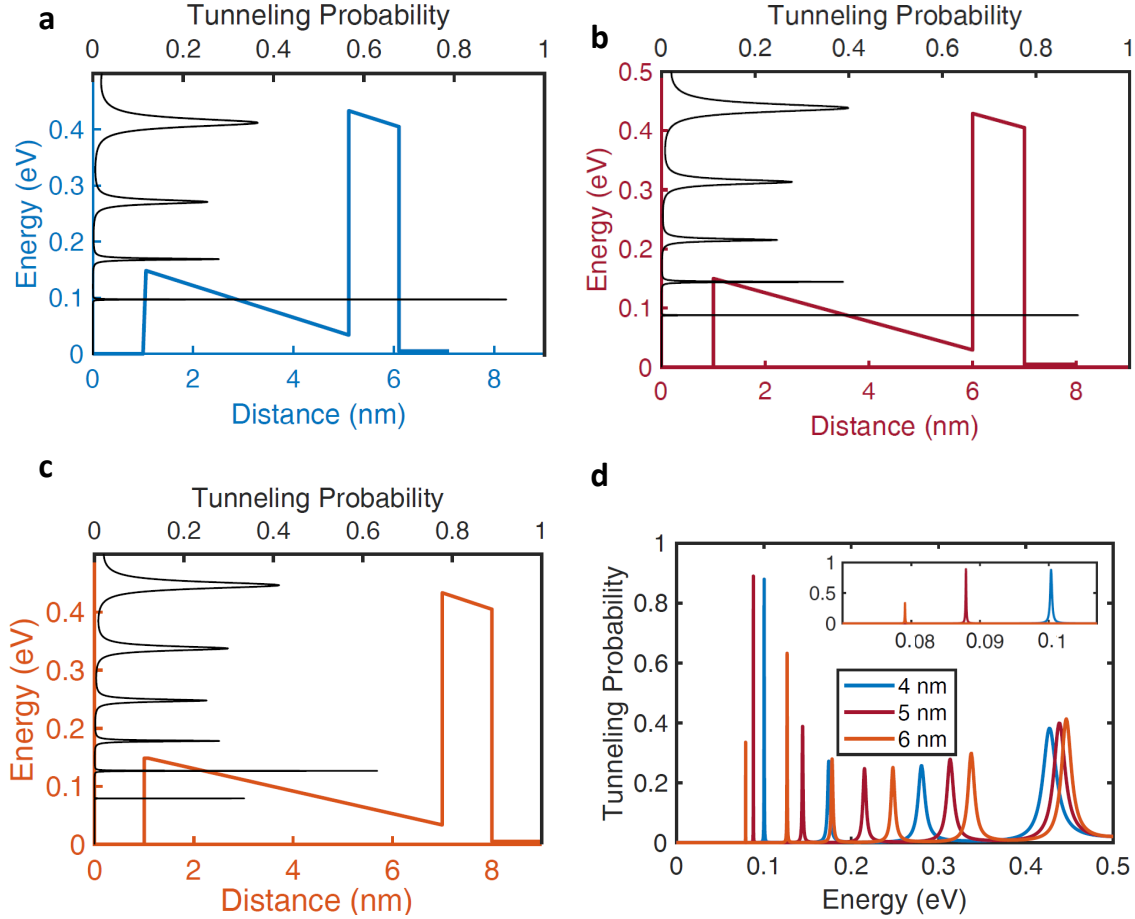


Figure 5.7: Tunneling probability and band diagrams of simulated NiO thicknesses of (a) 4 nm (b) 5 nm and (c) 6 nm Ni/NiO/1 nm  $\text{Al}_2\text{O}_3/\text{Cr}/\text{Au}$  diodes. (d) Tunneling probability of 4, 5 and 6 nm structures.

All of the three simulated thicknesses demonstrate a sharp maxima around 0.1 eV, where a quasi-bound state with a narrow energetic bandwidth exists through which electrons can tunnel. If these sharp peaks were identical, we would expect the 5 nm to exhibit a lower resistance since at room temperature, electrons are tightly concentrated around the Fermi-level, and a lower energy quasi-bound state should have more electrons tunneling through it. This is not the case here as each of these peaks has a different lifetime needed for electrons to decay out of the quasi-bound state. The lifetime associated with any of these states is related to the tunneling probability near resonance and, by the uncertainty principle, to the energy width of the resonance (Mendez and

von Klitzing, 2012). Both the Fermi-Dirac distribution of electrons and the energy width of the resonance peak must be taken into account when determining the current density. The 5 nm structure has a longer lifetime, a higher tunneling probability and a narrower resonance energy width. The 4 nm structure, with its wider bandwidth and a higher energy (0.01 eV above the 5 nm structure as depicted in the insert of Fig. 5.7 (d)) results in a higher current density and lower resistance since more electrons tunnel through the quasi-bound state compared to the 5 nm structure. This is why the lowest resistance is observed at 4 nm in Fig. 5.4 (b).

### 5.3.3 Negative differential resistance near zero-bias

As depicted in Fig. 5.7, a quasi-bound state exists around 0.1 eV above the Fermi level of Ni. Because only a few electrons tunnel through the quasi-bound state energy level due to the broad Fermi-Dirac distribution and its rapid falloff with energy, we do not observe negative differential resistance that normally occurs when tunneling through a resonant state. Instead, we observe a reduction in resistance when a small fraction of current determining electrons tunnel through that energy level. Observing a negative differential resistance near zero-bias in this structure would require a tighter electron distribution around the quasi-bound state energy level that can be achieved only at lower temperatures so that most electrons tunnel into the resonant level. For these reasons, we refer to the observed phenomena due to near-resonant tunneling as opposed to pure resonant tunneling.

## 5.4 Rectification enhancement at a wavelength of 10.6 $\mu\text{m}$

After confirming the near-resonance rectification enhancement effects in DC, Weerakkody performed illuminated measurements at 10.6  $\mu\text{m}$  to explore the possibility of exploiting these effects at high frequency (28 THz). We measured the open-circuit voltage ( $V_{oc}$ ) and the short-circuit current ( $I_{sc}$ ) of three fabricated rectenna structures, MI<sup>2</sup>M-2, MI<sup>2</sup>M-3 and MI<sup>2</sup>M-4 marked with red squares in Fig. 5.5b, using the optical measurement system shown in Fig. 3.5. The measured  $V_{oc}$  and  $I_{sc}$  values of MI<sup>2</sup>M-2 diode surpass those of the other two device thicknesses, as summarized

in Table 6.7. The total energy conversion efficiency of MI<sup>2</sup>M-2 diode-based rectenna surpasses every reported value in literature (Bareiß et al., 2013, Bean et al., 2009, 2011, Tiwari et al., 2009, Pelz and Moddel, 2019, Belkadi et al., 2018).

Table 5.1: MI<sup>2</sup>M-2, MI<sup>2</sup>M-3 and MI<sup>2</sup>M-4 efficiency calculation at 10.6  $\mu\text{m}$ , with a maximum beam intensity of 1  $\text{W}/\text{mm}^2$ , an area of 24  $\mu\text{m}^2$ , the input power ( $P_{in}$ ) is calculated to be 24  $\mu\text{W}$ .

Diode	$t_{NiO}^*$ (nm)	$V_{oc}$ ( $\mu\text{V}$ )	$I_{sc}$ (nA)	$R_0^{DC}$ ( $\text{k}\Omega$ )	$R_0^{HF}$ ( $\text{k}\Omega$ )	$\eta_c$ (%)	$\eta$ ( $10^{-7}$ %)
MI <sup>2</sup> M-2	4	91.7	14.3	13.9	5.2	5.1	17
MI <sup>2</sup> M-3	5	41	0.6	35.8	66.9	0.4	0.26
MI <sup>2</sup> M-4	6	43.8	2.1	21.8	19.6	1.4	1.1

\* $t_{NiO}$  = NiO thickness

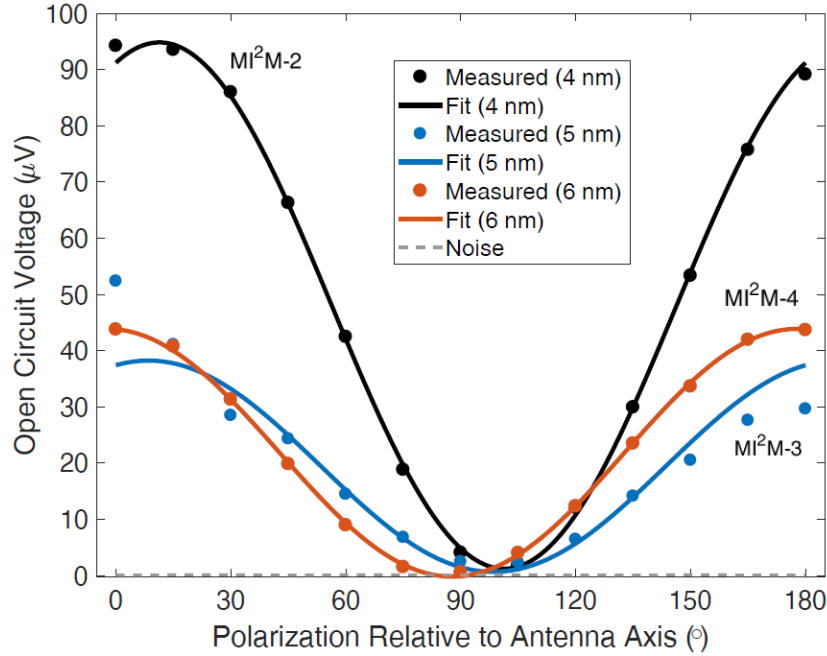


Figure 5.8: MI<sup>2</sup>M-2, MI<sup>2</sup>M-3 and MI<sup>2</sup>M-4  $V_{oc}$  curves. Optical measurements performed by Ayendra Weerakkody.

In the absence of resonant tunneling, the extracted  $R_0^{HF}$  under illumination is expected to increase compared to DC zero-bias resistance ( $R_0^{DC}$ ). This is because the voltage division across insulators in an MI<sup>2</sup>M structure changes from resistive in DC to capacitive at frequencies far above the cutoff frequency. In Ni/NiO/Al<sub>2</sub>O<sub>3</sub>/Cr/Au diodes at 28 THz, more voltage is applied across

the  $\text{Al}_2\text{O}_3$  layer and less across the NiO layer, making the diode resistance larger than in DC, as discussed in Ch. 4. This is due to the small real part of the complex dielectric constant of  $\text{Al}_2\text{O}_3$  at 28 THz. Since we have a quasi-bound state closer to the self-bias voltage in these structures, we are able to achieve a reduction in  $R_0^{HF}$  compared to  $R_0^{DC}$  through near-resonant tunneling effects, as presented in Table 6.7. The improvement in  $R_0^{HF}$  from DC (63 % drop) is extended to a high coupling efficiency ( $\eta_c$ ) and a high overall efficiency ( $\eta$ ) for the 4 nm structure, since in AC we can expect the Fermi level ( $E_F$ ) of Ni to get even closer to the quasi-bound state than in DC, improving the tunneling probability drastically since there is an exponential dependence with the energy difference between the energy state and the  $E_F$ . In MI<sup>2</sup>M-4, the drop in  $R_0^{HF}$  is less dramatic, around 10%, since its quasi-bound state is further away from the Fermi level of Ni compared to the 4 nm structure, as seen in Fig. 5.7. Because the optically measured 5 nm structure does not fall on the same trend line as the 4 and 6 nm structures (Fig. 5.5b) due to thickness dependent effects such as interfacial layers and NiO chemical compositions, we suspect the measured 5 nm structure does not have a quasi-bound state close to self-bias in the well. This is supported by the measured increase in  $R_0^{HF}$  compared to  $R_0^{DC}$  of the 5 nm structure, and the low coupling efficiency and total conversion efficiency.

## 5.5 Conclusions

In this chapter, we have experimentally demonstrated the effects of resonant tunneling in Ni/NiO/ $\text{Al}_2\text{O}_3$ /Cr/Au MI<sup>2</sup>M diodes, where a reduction in resistance is observed with an increase in responsivity. Increasing the thickness of NiO in MI<sup>2</sup>M diodes allows for the modification of the  $I(V)$  characteristics by altering the depth and width of the quantum well formed between the two oxides so that the metal Fermi level is aligned with quasi-bound states in the well. Alternatively, the well depth can be increased through biasing the diode at higher voltages or through changes in oxide voltage division due to capacitive voltage division at high frequency. We find that the reason resonant tunneling has been hard to demonstrate is the difficulty of building low-barrier diodes with wells deep enough at really low voltages, based on hundreds of diodes tried, and fabrication

limitations such as sub-nm control of thicknesses. Deep wells are necessary to reach quasi-bound states at low voltages necessary for energy harvesting applications. These NiO/Al<sub>2</sub>O<sub>3</sub> MI<sup>2</sup>M diode rectennas demonstrate record-setting improved total conversion efficiency, beating the previous state-of-the-art by a factor of a 100. The results of this chapter open a path towards efficient MIM-based optical rectennas for waste heat harvesting.

## CHAPTER 6

### COMPENSATION STRUCTURE FOR HIGH RESISTANCE MI<sup>2</sup>M DIODES

An efficient rectenna system requires a high diode rectification efficiency, a high antenna absorption efficiency and a high coupling efficiency between the diode and antenna. The bowtie antenna is a good candidate for high frequency operation, but has a typical impedance of  $\sim 100 \Omega$ . For maximum power transfer, this requires diodes with  $\sim 100 \Omega$  resistance, which typically have low responsivity and thus low rectification efficiencies at the frequency of operation. Another challenge in achieving a high coupling efficiency is the capacitive nature of MIM diodes. In this chapter, I explore compensation structure designs for impedance matching between the diode and antenna by compensating the diode capacitance with an inductive transmission line. The designs and simulations discussed in the chapter were provided by Gregor Lasser using ANSYS high-frequency structure simulator (HFSS). Using the germanium shadow mask process, described in Ch. 3, I fabricated transmission line compensation structures with varying length and made  $10.6 \mu\text{m}$  wavelength (28.3 THz) illumination measurements. The transmission line compensation structure achieves over an order of magnitude improvement in total conversion efficiency.

#### 6.1 Impedance matching with an MIM diode

The bowtie antenna has been extensively explored for radio frequency applications and microwave rectennas. For optical rectennas, bowtie antennas have been the popular choice because of their broadband impedance, their ease of fabrication, and their polarization-selective absorption efficiency (González and Boreman, 2005, Zhu, 2014). In the absence of diode capacitance, the

challenge in using bowtie antennas is the need for a high resistance antenna to match the diode's impedance. In the presence of diode capacitance, the problem is more complicated as the antenna impedance must match the diode's series equivalent impedance ( $R_d + X_d$ ) in a clamping circuit model of the rectenna configuration, presented in Fig. 1.5 in Ch. 1, such that

$$R_d = \frac{(R_0 X_D^2)}{(R_0^2 + X_D^2)} = \frac{R_0}{(\omega C R_0)^2 + 1} \quad (6.1)$$

$$X_d = \frac{-(R_0^2 X_D)}{(R_0^2 + X_D^2)} = \frac{-\omega C R_0^2}{(\omega C R_0)^2 + 1} \quad (6.2)$$

where  $R_d$  and  $X_d$  are the diode's equivalent real and imaginary parts of impedance, respectively,  $R_0$  and  $X_D$  are the diode's zero-bias resistance and reactance, respectively,  $\omega$  is the angular frequency and  $C$  is the diode's geometric capacitance.

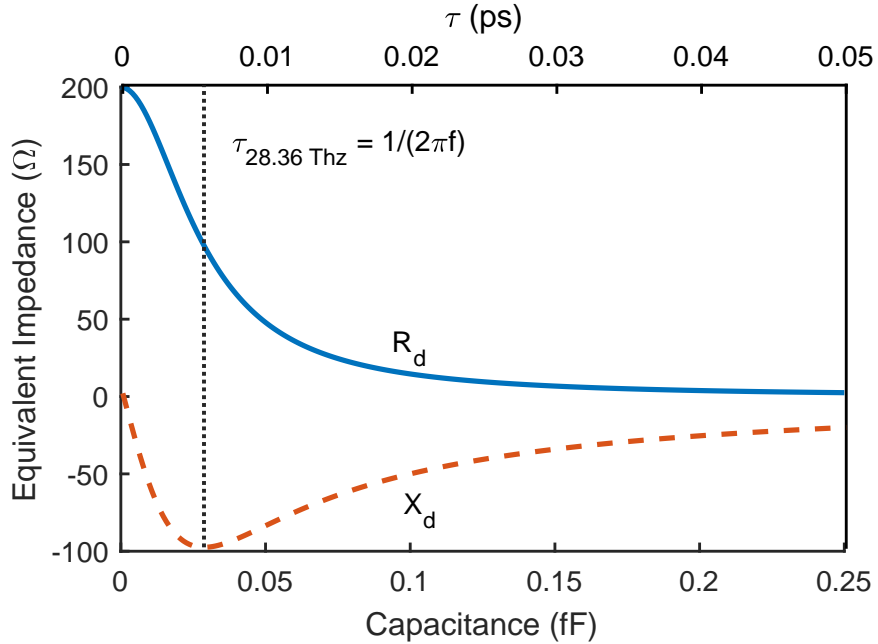


Figure 6.1: Impedance of 200  $\Omega$  MIM diode versus capacitance and RC time constant. For this diode, when capacitance increases beyond 0.15 fF,  $R_d$  drops below 6  $\Omega$ . The  $X_d$  decreases to  $-R_0/2$  ( $-100 \Omega$ ) when  $\tau = 1/2\pi f = RC$  ( $C = 0.028$  fF) before increasing to  $-25 \Omega$  at  $C = 0.22$  fF and eventually to  $-1/\omega C$  at high capacitance values.

Diode resistance, capacitance and operating frequency determine the diode's impedance and therefore the desired impedance of the antenna. Figure 6.1 presents the equivalent series impedance

of an MIM diode with  $R_0 = 200 \Omega$  as a function of capacitance at 28.3 THz. For diodes with very small or negligible capacitance values, where  $C \sim 1$  aF, the diode's impedance  $R_d \sim R_0$ . As capacitance increases,  $X_D$  decreases and  $R_d$  decays to approach zero, while  $X_d$  approaches  $-1/\omega C$ .

## 6.2 Antenna modeling with HFSS

Accurate modeling of the antenna in a shadow mask process is crucial to the impedance tuning in a rectenna system. We used HFSS to model the full rectenna system, including the shadowing effects that result from the GSM process, as shown in Fig. 6.2. The initial antenna design used a  $24^\circ$  bowtie antenna, as seen in Fig. 6.2 (b), and a total antenna width of  $5.6 \mu\text{m}$  including the diode overlap region. The simulated diode stack consisted of Ni (45 nm), NiO (3.5 nm),  $\text{Al}_2\text{O}_3$  (0.7 nm), Cr (3 nm) and Au (35 nm). We used measured oxide material properties at 28 THz for the NiO and  $\text{Al}_2\text{O}_3$  layers, extracted material properties from Palik (Palik, 1998) for Ni, Cr and Au, and default material properties suggested by HFSS for Si and  $\text{SiO}_2$ . For ease of simulation, we used a mixed dielectric layer instead of two dielectrics, as suggested by Pelz (Pelz, 2018), and only simulated 10 nm of Au as the top layer. The mixed dielectric layer has an equivalent relative permittivity calculated from the series capacitance of the two oxides.

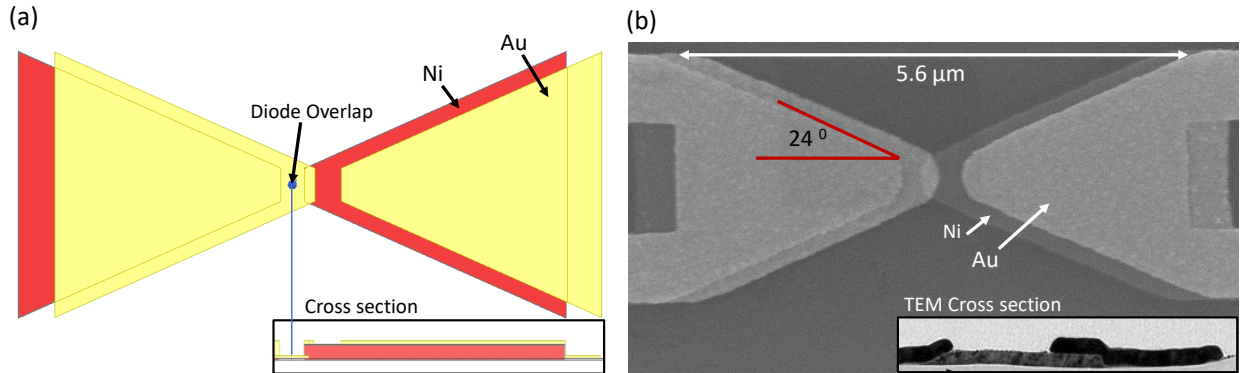


Figure 6.2: Top view and cross section of (a) simulated and (b) fabricated bowtie antenna using the GSM process. The diode stack consisted of Ni, NiO,  $\text{Al}_2\text{O}_3$ , Cr and Au sitting on  $\text{SiO}_2$  (300 nm) on Si. Simulations were conducted by Gregor Lasser using HFSS. The simulated structure (a) is a good representation of the GSM structure, as verified by the scanning electron microscopy (SEM) and transmission electron microscopy (TEM) images in (b).

To calculate antenna impedance only, the diode overlap region was removed using lumped port modeling with diode region excavation. The fields at the ports were obtained through solving for the eigenmodes in HFSS, where the structure was modeled with two thin perfect electric conductor (PEC) strips. This was done because HFSS modeled the metals as perfect dielectrics, based on their 28 THz material properties. Figure 6.3 presents the bowtie antenna impedance, for a frequency sweep between 25 and 40 THz, and the antenna radiation pattern at 28.3 THz. COMSOL simulations for the bowtie antenna impedance at 28.3 THz for a diode stack with 60 nm thick Au and 5 nm total insulator thickness resulted in an antenna impedance of  $Z_a = 117 - j 112 \Omega$  and an antenna efficiency of 10% (Pelz, 2018). Here, HFSS simulations of a  $24^\circ$  bowtie antenna, for a Ni/NiO/Al<sub>2</sub>O<sub>3</sub>/Au material stack, resulted in an impedance of  $Z_a = 92.8 - j 35.1 \Omega$  with an antenna absorption efficiency ( $\eta_a$ ) of 8.5% corresponding to a gain (G) of -10.7 dB at 28.3 THz.

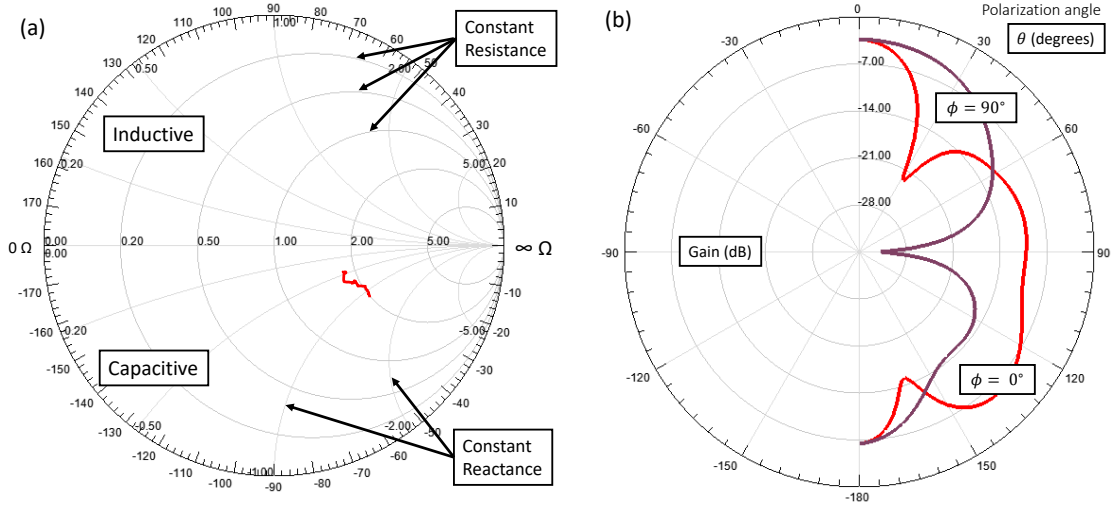


Figure 6.3: Impedance and radiation pattern of simulated bowtie antenna with  $24^\circ$  angle. (a) Smith chart with circles of constant resistance and reactance where both are normalized to  $50 \Omega$ . The bottom and top halves of the chart represent capacitive and inductive reactance. The real and imaginary parts of the bowtie antenna impedance vary between 90 and  $100 \Omega$  and -24 and  $-50 \Omega$ , respectively, for a frequency sweep between 20 and 40 THz, according to simulations. The antenna's impedance is  $Z = 92.8 - j 35.1 \Omega$  at 28.3 THz. (b) The radiation pattern of the bowtie antenna with polarization angle  $\theta$ . The pattern presents the distribution of radiation energy into space as a function of direction, in both principle planes of incidence ( $\phi = 0^\circ$  with illumination normal to the antenna plane and  $\phi = 90^\circ$  with illumination in the antenna plane). For  $\phi = 0^\circ$  and at a frequency of 28.3 THz, the antenna efficiency is 8.5% ( $G = 10 \log_{10}(\eta_a)$ ), for an antenna on 300 nm SiO<sub>2</sub> and 1  $\mu\text{m}$  Si. HFSS simulations were performed by Gregor Lasser.

Next, we looked at the effects of material thickness and bowtie arm lengths on the impedance. The bowtie DC arms are the leads connected to the bowtie antenna ends used for DC measurements, seen in Fig. 6.4. As the thickness of Au increases, the antenna impedance decreases while its capacitance increases. We found that the thickness of the diode oxide layers has no impact on antenna impedance and a very slight impact on gain, where thinner oxides have higher gain. The thickness of SiO<sub>2</sub> was found to have minimal effects on impedance. Radiation pattern gain decreased as the thickness of Si increased beyond 2.65  $\mu\text{m}$  at 28.3 THz. Including the effects of material thicknesses, the bowtie DC arms, and a lossless substrate, the 24° bowtie antenna's impedance was determined to be  $Z = 66 - j 42 \Omega$ . Table 6.1 presents simulation conditions and corresponding antenna impedances. To increase the total rectenna coupling efficiency we need to decrease the antenna's impedance to match the diode series equivalent impedance and cancel the diode's capacitance by making an inductive antenna.

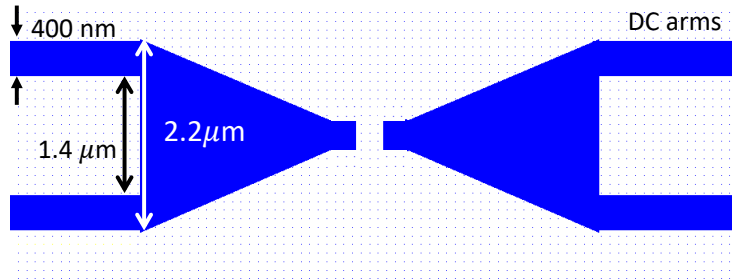


Figure 6.4: Bowtie antenna DC arms with a width of 400 nm.

Table 6.1: Antenna impedance simulation results. The mixed dielectric layer has an equivalent relative permittivity calculated from the series capacitance of the two oxides (NiO and Al<sub>2</sub>O<sub>3</sub>). The bowtie DC arms are the leads connected to the bowtie antenna ends used for DC measurements.

Simulation parameters	Antenna impedance
Base design: GSM process, mixed dielectric layer, 10 nm Au top metal	$Z = 92.8 - j 35.1 \Omega$
Thicker Au (80 nm) top metal and no bowtie DC arms	$Z = 80 - j 33 \Omega$
Adding 5 $\mu\text{m}$ length bowtie DC arms	$Z = 68 - j 28 \Omega$
Adding PEC metals and lossless SiO <sub>2</sub> substrate	$Z = 66 - j 42 \Omega$

### 6.3 Variable impedance bowtie antenna

One method of antenna impedance tuning is a transmission line compensation structure (Bakshi, 2009). For a bowtie antenna, this means moving the diode from the feedpoint of the antenna using a variable length transmission line, as shown in Fig. 6.5. Changing the length of the transmission line causes the antenna impedance to rotate around the Smith chart which enables antenna impedance tuning, as illustrated from simulation results in Fig. 6.5 (c). Structure geometry, for example transmission line gap and bowtie antenna angle, allows for further tuning of the antenna impedance. A smaller transmission line gap between the leads and a smaller antenna angle provide a wider impedance range with transmission line length. A nearly full rotation around the Smith chart is achieved with a transmission line length of  $2.5 \mu\text{m}$ , as seen from simulation results presented in Fig. 6.6 for a  $15^\circ$  angle bowtie antenna with a shadow mask transmission line gap of  $650 \text{ nm}$ , and transmission line widths of  $550 \text{ nm}$ . The effective gap following material depositions is expected to be  $100 \text{ nm}$ . Table 6.2 presents  $0.5 \mu\text{m}$  variations in transmission line length between 0 and  $2.5 \mu\text{m}$  and the antenna's corresponding impedance values. With one full rotation around the Smith chart, resistance drops then increases, while reactance varies from capacitive to inductive and back to capacitive.

Table 6.2: Impedance of a  $15^\circ$  angle bowtie antenna with varying transmission line length between 0 and  $2.5 \mu\text{m}$ .

		Transmission line length					
		$0 \mu\text{m}$	$0.5 \mu\text{m}$	$1 \mu\text{m}$	$1.5 \mu\text{m}$	$2 \mu\text{m}$	$2.5 \mu\text{m}$
Antenna impedance	$R_a (\Omega)$	63	34	30	51	93	96
	$\chi_a (\Omega)$	-44	-22	2	26	23	-23

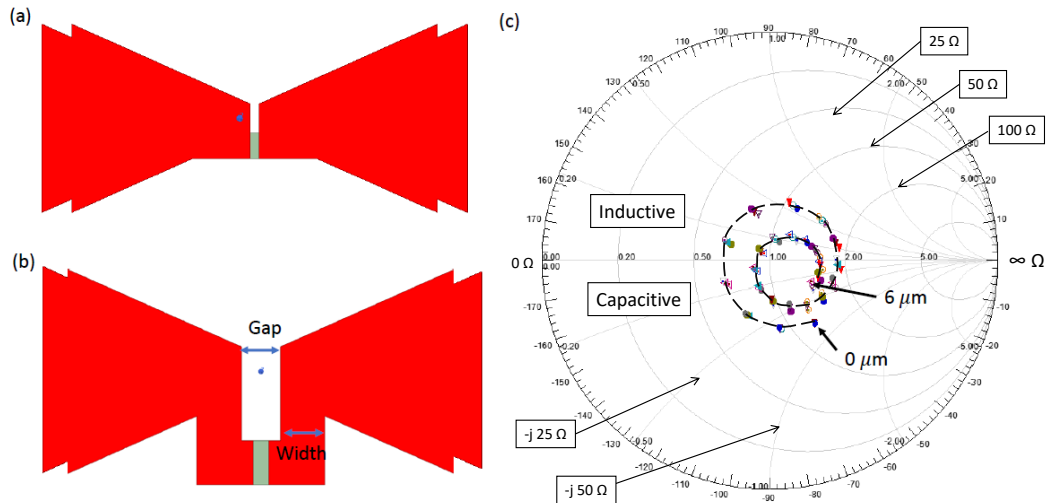


Figure 6.5: Transmission line compensation structure with  $24^\circ$  antenna. GSM shadowing simulation of a bowtie antenna (a) without a transmission line (TX) and (b) with a TX where the diode is shifted from the feed point of the antenna. (c) Changing the TX length, between 0 and  $6 \mu\text{m}$ , allows for a nearly full rotations around the Smith chart which enables antenna impedance tuning. The TX width is varied between 350 and 550 nm for each length, shown by the multiple points per length in the Smith chart. HFSS simulations were performed by Gregor Lasser.

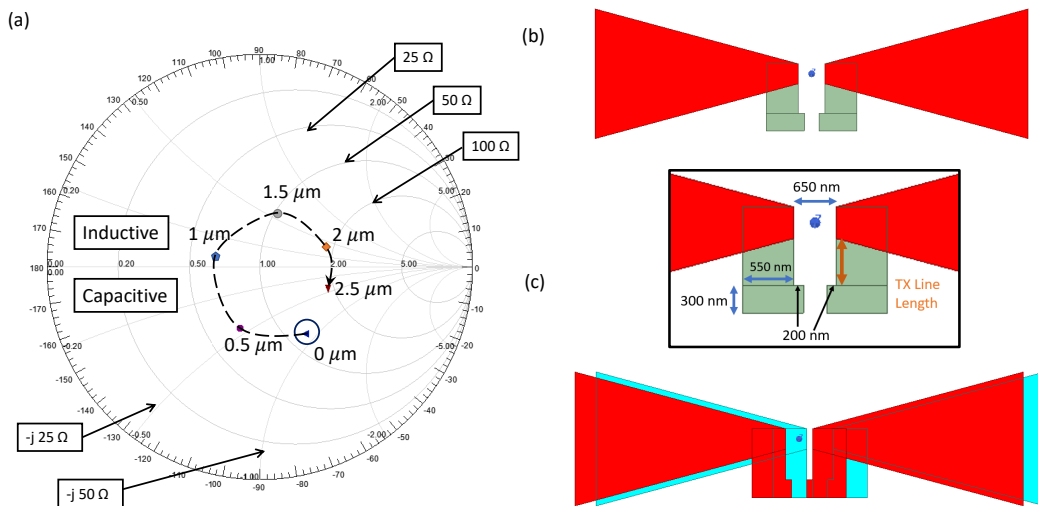


Figure 6.6: Transmission line compensation structure with  $15^\circ$  antenna. (a) Smith chart with antenna impedance modified by a varying TX length between 0 and  $2.5 \mu\text{m}$ . (b) Bowtie antenna and TX dimensions for fabrication with a germanium shadow mask process: bowtie angle of  $15^\circ$ , pre-fabrication TX gap of 650 nm, TX width of 550 nm, diode length of 300 nm, and 200 nm offset to achieve a post-fabrication transmission line gap of 100 nm. The last schematic presents the expected top view of the designed antenna after material angle depositions. HFSS simulations were performed by Gregor Lasser.

## 6.4 Expected efficiency enhancement with transmission line

Following the power waterfall analysis discussed in Ch. 4, and presented in Fig. 6.7, I calculated the projected efficiency for two diodes: a single insulator Ni/NiO/Cr/Au MIM diode with a resistance of  $200 \Omega$  and a capacitance of  $0.19 \text{ fF}$  (MIM-2), and a double insulator Ni/NiO/Al<sub>2</sub>O<sub>3</sub>/Cr/Au MIIM diode with a resistance of  $2000 \Omega$  and a capacitance of  $0.09 \text{ fF}$  (MI<sup>2</sup>M-5) with diode areas of  $0.018 \mu\text{m}^2$ . The diodes' series equivalent impedance is summarized in Table 6.3.

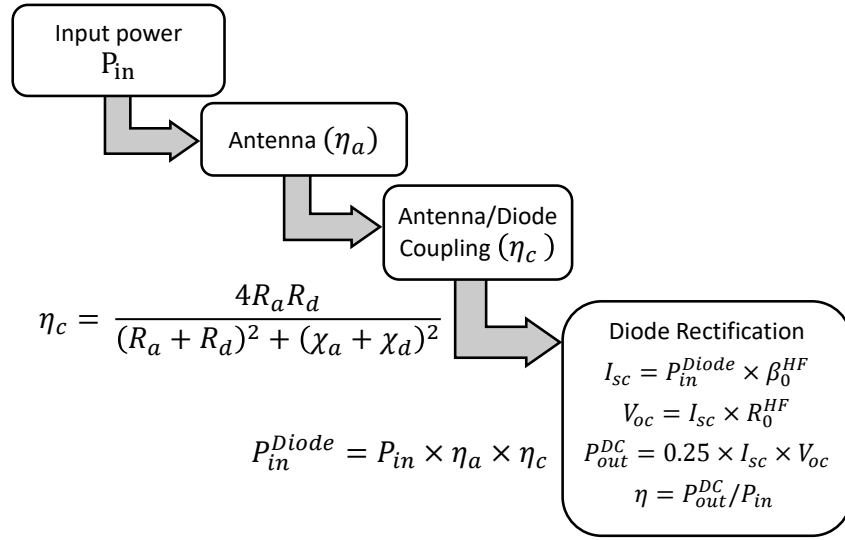


Figure 6.7: Rectenna power waterfall diagram.

Table 6.3: MIM-2 and MI<sup>2</sup>M-5 series equivalent impedance calculations

Diode	$R_0$ ( $\Omega$ )	C (fF)	$R_d$ ( $\Omega$ )	$X_d$ ( $\Omega$ )
MIM-2	200	0.19	4.46	-29.5
MI <sup>2</sup> M-5	2000	0.09	1.94	-62.3

Both rectenna systems were assumed to have an input power of  $24 \mu\text{W}$  and an antenna absorption efficiency of 8.5%, calculated from HFSS simulations. Figure 6.8 (a) illustrates antenna resistance and reactance as a function of transmission line length, for the lengths presented on the Smith chart in Fig. 6.6. Length variation varies antenna resistance,  $R_a$ , between 30 and  $100 \Omega$  while reactance varies between capacitive and inductive.

The diode-antenna system coupling efficiency, presented in Ch. 4, is defined as

$$\eta_c = \frac{4R_a R_d}{(R_a + R_d)^2 + (X_a + X_d)^2} \quad (6.3)$$

As the transmission line length is increased from 0 to 1  $\mu\text{m}$ ,  $R_a$  drops while  $X_a$  increases, which increases coupling efficiency. Given the capacitive nature of MIM diodes, the maximum coupling efficiency improvement occurs between 1 and 2  $\mu\text{m}$  transmission line length, where the antenna is inductive, as shown in Fig. 6.8 (a). The exact peak depends on the diode's capacitance and resistance values where the impedance of the antenna and the diode are best matched. For MIM-2, the best performance occurs at a length of 1.3  $\mu\text{m}$  whereas for MI<sup>2</sup>M-5, the optimal length is 1.5  $\mu\text{m}$ , as seen in Fig. 6.8 (b). Past a length of 2  $\mu\text{m}$ , the antenna becomes capacitive and no longer compensates for the diode capacitance while also increasing in resistance, causing a drop in coupling efficiency. This is observed for two diodes with different impedance values in Fig. 6.8 (b). Figure 6.9 illustrates how the numerator and denominator of Eq. 6.3 change with transmission line length for MIM-2 and MI<sup>2</sup>M-5. The total power conversion efficiency as a function of transmission line length is presented in Fig. 6.10. A high responsivity results in a high short circuit current and a high resistance results in a high open-circuit voltage, which are used to calculate output DC power, as discussed in the waterfall diagram in Fig. 6.7, and summarized as

$$P_{out}^{DC} = P_{in} \times \eta_a \times \eta_c \times 0.25 \times \beta_0^{HF} \times R_0^{HF} \quad (6.4)$$

Because MI<sup>2</sup>M-5 has a high resistance (2000  $\Omega$ ) and a high responsivity (0.5 A/W), its total conversion efficiency is higher than MIM-2 ( $R_0 = 200 \Omega$  and  $\beta_0 = 0.4 \text{ A/W}$ ), even though MIM-2 has a higher coupling efficiency.

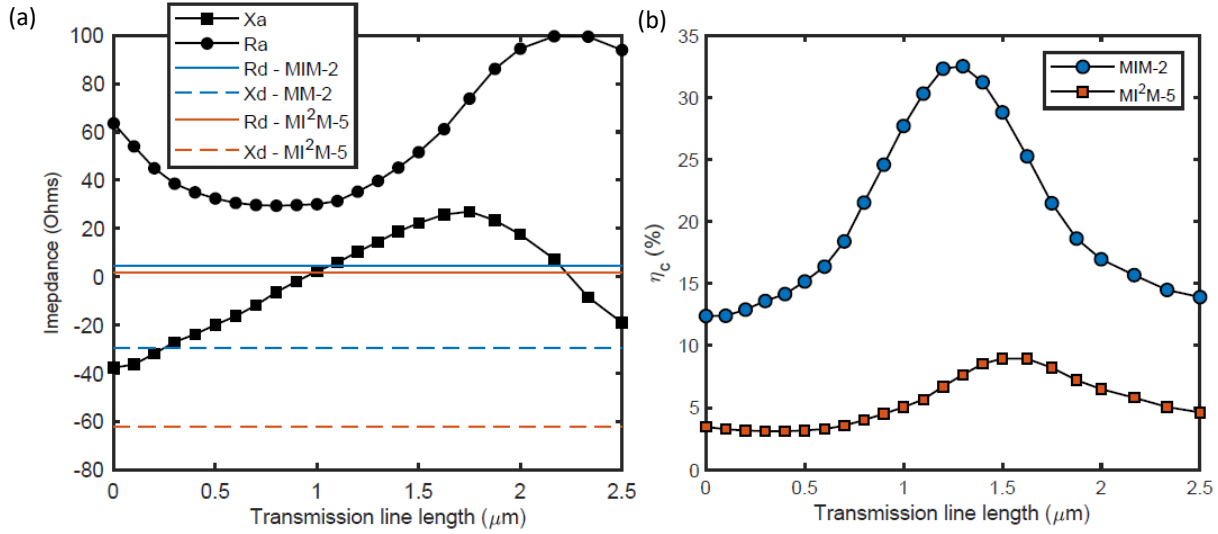


Figure 6.8: Effects of transmission line length on diode characteristics and coupling efficiency. (a) Simulated impedance versus transmission line length where  $R_a$  and  $X_a$  are the antenna resistance and reactance, respectively, as a function of transmission line length. MIM-2 has a series equivalent impedance of  $4.46 - j 29.5 \Omega$  and MI<sup>2</sup>M-5 has a series equivalent impedance of  $1.94 - j 62.3 \Omega$ . (b) Coupling efficiency as a function of transmission line length. As the transmission line length is increased from 0 to 1  $\mu\text{m}$ ,  $R_a$  drops while  $X_a$  increases, which increases coupling efficiency. For MIM-2, the best performance is expected to be for a length of 1.3  $\mu\text{m}$  whereas for MI<sup>2</sup>M-5, the best length is 1.5  $\mu\text{m}$ . Past a length of 2  $\mu\text{m}$ , the antenna becomes capacitive while its resistance increases, causing a drop in coupling efficiency.

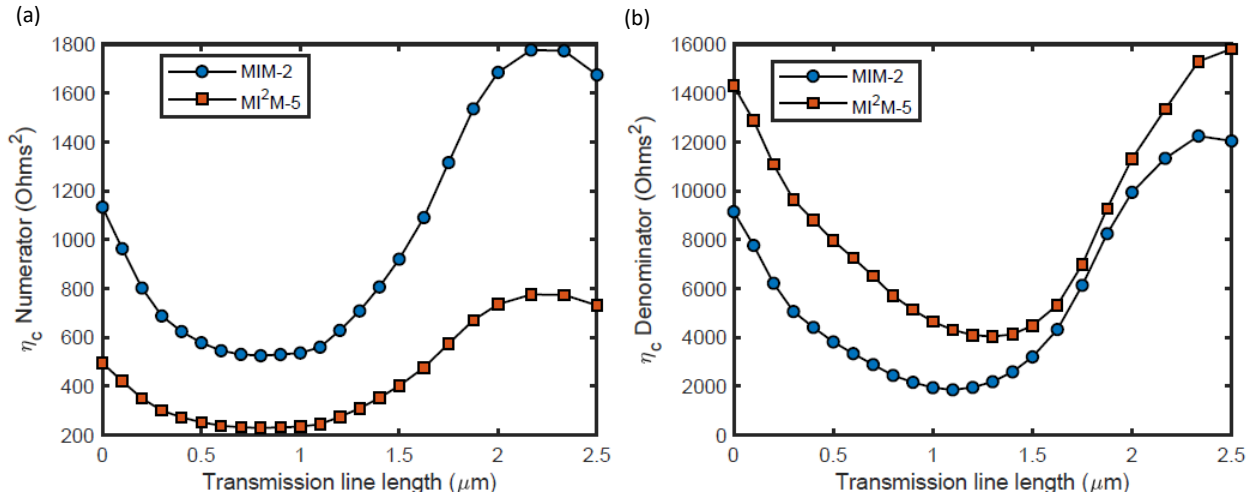


Figure 6.9: Effects of transmission line length on Eq. 6.3. (a) Coupling efficiency numerator and (b) denominator versus transmission line length for MIM-2 and MI<sup>2</sup>M-5. Maximum coupling efficiency occurs around the valley of the coupling efficiency denominator. The best performance is expected to be around 1  $\mu\text{m}$  and 1.5  $\mu\text{m}$  for MIM-2 and MI<sup>2</sup>M-5, respectively.

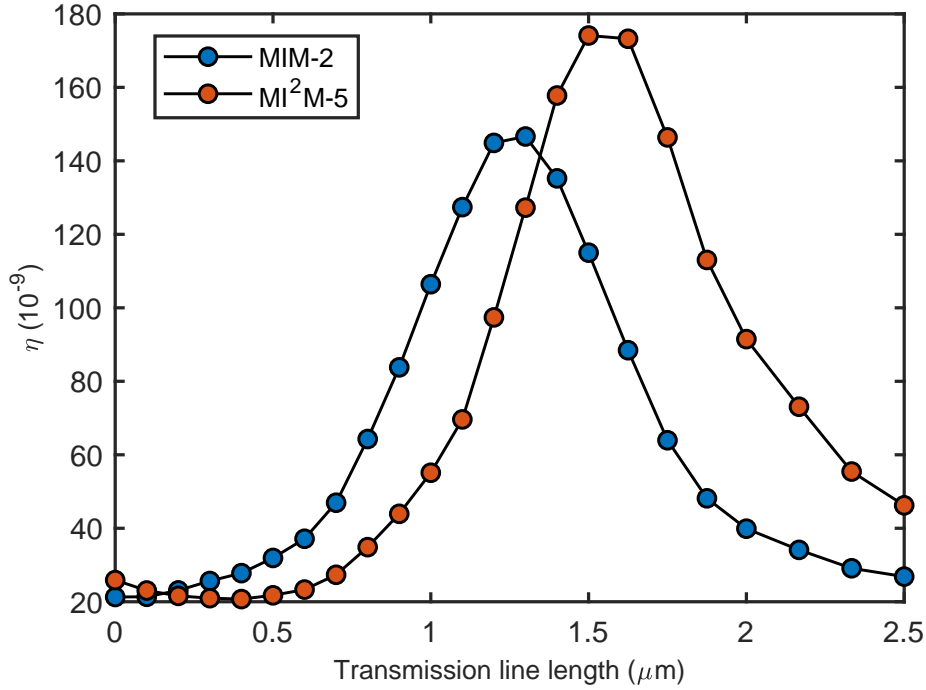


Figure 6.10: Expected rectenna conversion efficiency versus transmission line length. For MIM-2, the best performance is expected to be for a length of  $1.3 \mu\text{m}$  whereas for MI<sup>2</sup>M-5, the best length is  $1.5 \mu\text{m}$ . Because MI<sup>2</sup>M-5 has a high resistance ( $2000 \Omega$ ) and a high responsivity ( $0.5 \text{ A/W}$ ), its total conversion efficiency is higher than MIM-2 ( $R_0 = 200 \Omega$  and  $\beta_0 = 0.4 \text{ A/W}$ ), even though MIM-2 has a higher coupling efficiency. The efficiency is calculated as  $\eta = \eta_a \times \eta_c \times 0.25 \times \beta_0^{HF} \times R_0^{HF}$ .

## 6.5 MIM diode fabrication

To investigate the effect of the compensation structure on the total efficiency of the diode, I designed rectennas with five compensation structure lengths:  $0.5 \mu\text{m}$ ,  $1 \mu\text{m}$ ,  $1.5 \mu\text{m}$ ,  $2 \mu\text{m}$  and  $2.5 \mu\text{m}$ , as presented in Fig. 6.6, as well as reference design without the compensation structure. The transmission line was designed to have a  $100 \text{ nm}$  gap separation between its leads after material depositions. Two different material sets were tested: a single-insulator MIM diode (Ni/NiO/Cr/Au) and a double-insulator MI<sup>2</sup>M diode (Ni/NiO/Al<sub>2</sub>O<sub>3</sub>/Cr/Au), following the material deposition conditions presented in Table 6.4. Two different oxide thicknesses were used when fabrication the MIM diode and one oxide thickness for the MI<sup>2</sup>M diode, resulting in three test structures with varying resistance and capacitance values. The single insulator structure was tested due to ease of

fabrication and analysis. The diodes were fabricated using angled evaporations through the shadow mask, as discussed in Ch. 3, with angles of  $\theta_{Ni} = \theta_{Cr/Au} = 39.5^\circ$ .

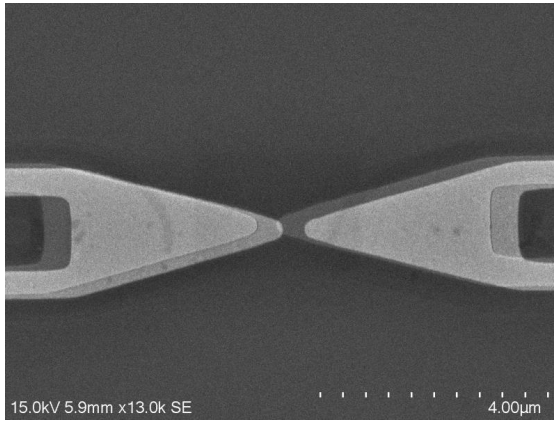
Table 6.4: Material deposition conditions.  $R_0$  is measured zero-bias resistance and C is calculated capacitance. Estimated sputtering rates are 3 nm for 90 s, 2.4 nm for 75 s and 4 nm for 150 s for sputtered NiO and 0.7 nm for 150 s for sputtered  $Al_2O_3$ , based on ellipsometry measurements by Ayendra.

Wafer	Material set	Thickness (nm)		Sputtering time (s)		$R_0$ ( $\Omega$ )	C (fF)
		Ni	Cr/Au	NiO	$Al_2O_3$		
A	Ni/NiO/Cr/Au	45	5/35	150	–	700 - 870	$\sim 0.26$
B	Ni/NiO/Cr/Au	45	5/35	90	–	300 - 400	$\sim 0.31$
C	Ni/NiO/ $Al_2O_3$ /Cr/Au	45	5/35	75	150	740 - 1050	$\sim 0.17$

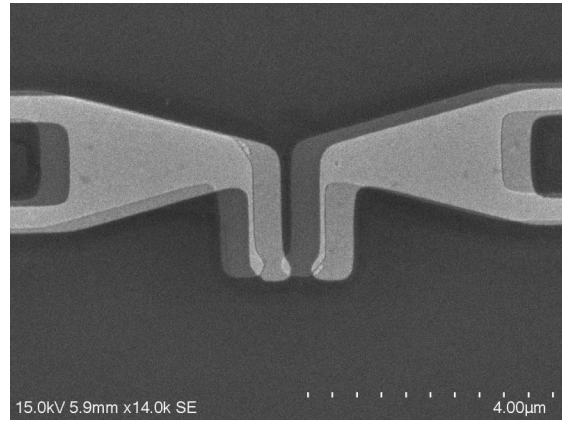
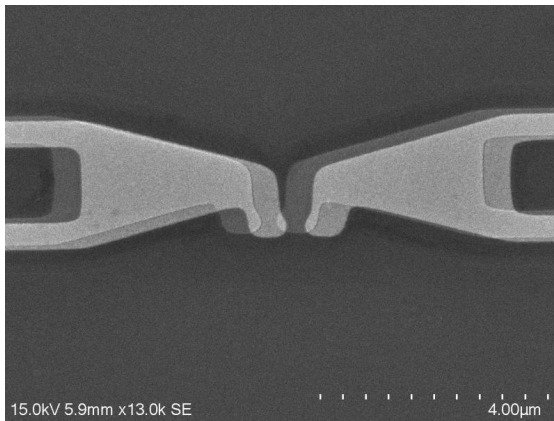
Figure 6.11 shows SEM images of the five different transmission line lengths and a reference design with no transmission line. Measured diode areas and transmission line separations are presented in Table 6.11. As can be seen from the SEM images, the diode overlap area of device A.1 ( $0.017 \mu m^2$ ) is approximately half that of the diode overlap areas of the five devices with transmission line structures ( $0.029 - 0.035 \mu m^2$ ). The transmission line separation varied between 122 and 158 nm. Both diode area and transmission line separation can be adjusted by choosing different angles for material depositions.

Table 6.5: Areas of diodes with transmission lines (TX) and transmission line separation from SEM images in Fig. 6.11. Area is calculated as  $0.7 \times \text{length} \times \text{overlap}$  because of the rounding of the corners.

Diode	TL length	Diode area from SEM images	TX separation
A.1	0 nm	$0.7 \times 235 \text{ nm} \times 101 \text{ nm} = 0.017 \mu m^2$	0 nm
A.2	500 nm	$0.7 \times 341 \text{ nm} \times 147 \text{ nm} = 0.035 \mu m^2$	122 nm
A.3	1 $\mu m$	$0.7 \times 332 \text{ nm} \times 145 \text{ nm} = 0.034 \mu m^2$	150 nm
A.4	1.5 $\mu m$	$0.7 \times 317 \text{ nm} \times 130 \text{ nm} = 0.029 \mu m^2$	158 nm
A.5	2 $\mu m$	$0.7 \times 290 \text{ nm} \times 145 \text{ nm} = 0.029 \mu m^2$	138 nm
A.6	2.5 $\mu m$	$0.7 \times 296 \text{ nm} \times 145 \text{ nm} = 0.030 \mu m^2$	154 nm



(a) A.1 - 0 nm

(d) A.4 - 1.5  $\mu\text{m}$ 

(b) A.2 - 500 nm

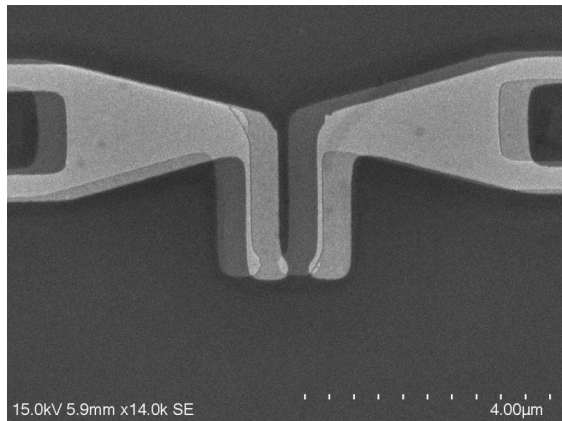
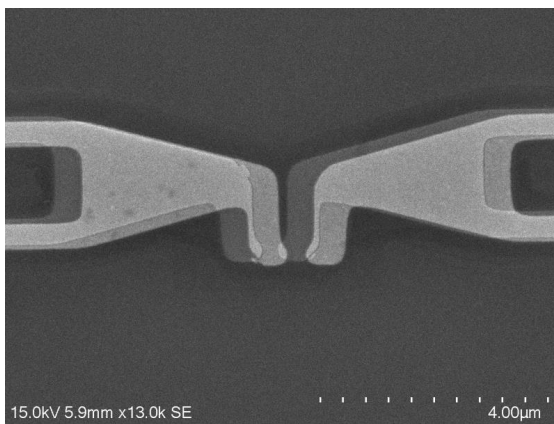
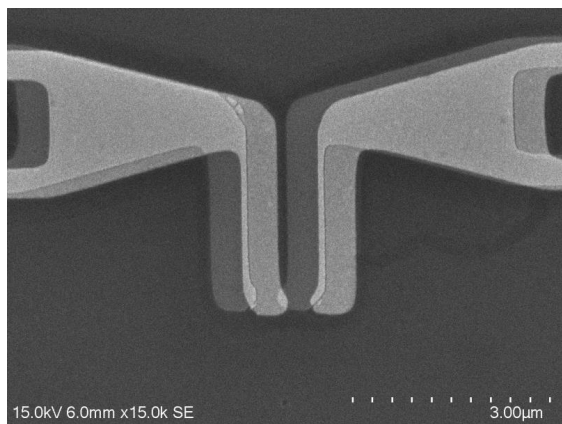
(e) A.5 - 2  $\mu\text{m}$ (c) A.3 - 1  $\mu\text{m}$ (f) A.6 - 2.5  $\mu\text{m}$ 

Figure 6.11: SEM images of different transmission line lengths. (a) Lumped element diode with no transmission line. Lumped element diodes with transmission line lengths of (b) 500 nm (c) 1  $\mu\text{m}$  (d) 1.5  $\mu\text{m}$  (e) 2  $\mu\text{m}$  and (f) 2.5  $\mu\text{m}$ .

### 6.5.1 Diode array design

To better observe rectification enhancement due to the compensation structure, I designed, fabricated and measured arrays of diodes. Three different array designs were explored: 16 element series arrays (Fig. 6.12 (a)), 16 element parallel arrays (Fig. 6.12 (b)) and 36 element staggered arrays (Fig. 6.12 (c)). For illuminated diode experiments of the compensation structures, I chose to use the 16 element series arrays because shorted device were more common on this wafer than open devices. Moreover, with 16 diodes in series, the signal to noise ratio is lower, making it easier to extract individual diode performance metrics and measure low resistance diodes so as to make accurate conclusions regarding transmission line effects. To avoid coupling between rectennas, the horizontal and vertical spacing between elements were  $5.5 \mu\text{m}$  and  $11 \mu\text{m}$  respectively, as determined from HFSS simulations provided by Gregor Lasser. The staggered design will be further explored in Ch. 7.

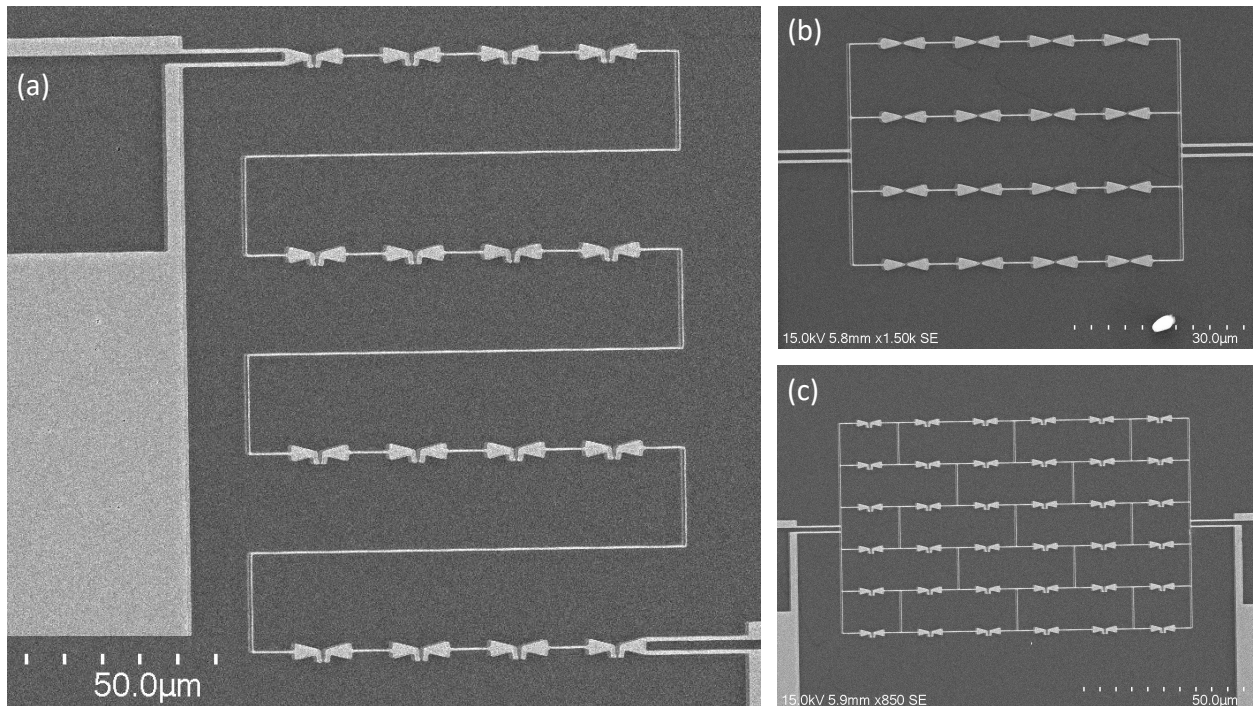


Figure 6.12: SEM image of different array designs: (a) 16 elements in series, (b) 16 elements with four parallel sub-arrays composed of four elements in series and (c) 36 elements in a staggered array design.

## 6.6 Diode array optical measurements

Following fabrication, the diode arrays were DC tested to confirm all 16 elements were diodes without any shorts or opens. This was done by comparing the 16 series element resistance with a single element diode using 4-point probe measurements. I then performed illuminated measurements to check the high frequency response and the effect of the transmission line compensation structure. I performed both open-circuit voltage ( $V_{oc}$ ) and short-circuit current ( $I_{sc}$ ) measurements, using a lock-in amplifier and the measurement setup discussed in Ch. 3. For diodes with resistance values comparable to lead resistances, as is the case for single insulator MIM diodes with  $R_0 < 500 \Omega$ , only  $V_{oc}$  measurements were performed.

The lock-in amplifier measures the RMS voltage ( $V_{rms}$ ) of the fundamental sine wave of the input signal at the modulation frequency. The input signal in this setup is a pulse width modulated (PWM) square wave with a duty cycle of 11%. Therefore,  $V_{oc}$  and  $I_{sc}$  are computed as (Pelz, 2018)

$$V_{oc} = \frac{V_{rms}\pi}{0.11\sqrt{2}} \quad (6.5)$$

$$I_{sc} = \frac{I_{rms}\pi}{0.11\sqrt{2}} \quad (6.6)$$

### 6.6.1 Open-circuit voltage polarization dependence

Under illumination, a bowtie antenna is expected to exhibit a  $\cos^2$  polarization response (Pelz, 2018), with a  $\sin^2$  thermal response Bareiß et al. (2013), as discussed in Ch. 3, such that

$$V_{oc}(\theta) = A_{\parallel}\cos(\theta + \phi)^2 + A_{\perp}\sin(\phi)^2 \quad (6.7)$$

where  $\theta$  is the polarization angle and  $\phi$  is a polarization angle offset due to alignment issues or beam wander. I measured the infrared optical response of MIM-diode based rectennas with different transmission line lengths to verify polarization dependence of rectification, and potentially observe enhancement and then degradation as the length is increased. The input power to the diode arrays was calculated by measuring the maximum beam intensity and using the absorption area of the rectenna. The area of the 16 element series array is  $0.007 \text{ mm}^2$ . The beam is large enough to align

the array at the center where it will receive the maximum intensity. The intensity falls off by no more than 10% inside a 1 mm diameter circle. For ease of calculations, I estimate the absorption area of the rectenna to be a circle with the antenna's largest dimension as the diameter (Pelz, 2018). The absorption area is determined to be  $52.3 \mu\text{m}^2$  and  $48.7 \mu\text{m}^2$  for individual diodes with no transmission line and transmission line structures, respectively, as seen in Fig. 6.13.

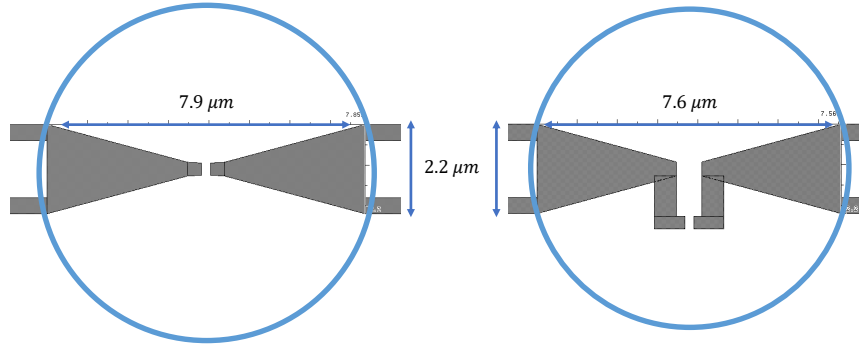


Figure 6.13: Antenna areas for (a) no transmission line and (b) with transmission line. The absorption area is determined by calculating the area of the circle with radius equal to the the largest antenna dimension. In (a), the diameter is computed as  $d = \sqrt{(7.9)^2 + (2.2)^2}$ . Absorption area is calculated as  $A = \pi r^2$  for  $r = d/2$ .

Figure 6.14 presents  $V_{oc}$  response versus polarization angle for two lumped element diodes: one without a transmission line and one with a  $0.5 \mu\text{m}$  length compensation structure, and Fig. 6.15 presents  $V_{oc}$  response versus polarization angle for a  $2 \mu\text{m}$  length compensation structure compared to a lumped element with no compensation structure. The 16 element series array presents a clean  $\cos^2$  response with polarization angle as expected for a rectification response: peaks at  $\theta + \phi = 0^\circ$ ,  $180^\circ$  and  $360^\circ$  when the illumination polarization is aligned with the antenna axis. The response dips to noise level at  $\theta + \phi = 90^\circ$  and  $270^\circ$  when the polarization is perpendicular to the antenna axis. Small shifts are expected since the alignment of the rectenna to the  $0^\circ$  polarization angle is done by eye through a microscope with  $100\times$  magnification. A thermal response would result in a  $\sin^2$  response with polarization angle (Barei et al., 2013). Once polarization dependence was verified for all the structures of different length compensation structure, I used measured  $V_{oc}$  and  $I_{sc}$  values to compute the total energy conversion efficiency ( $\eta = 0.25 \times V_{oc} \times I_{sc}$ ).

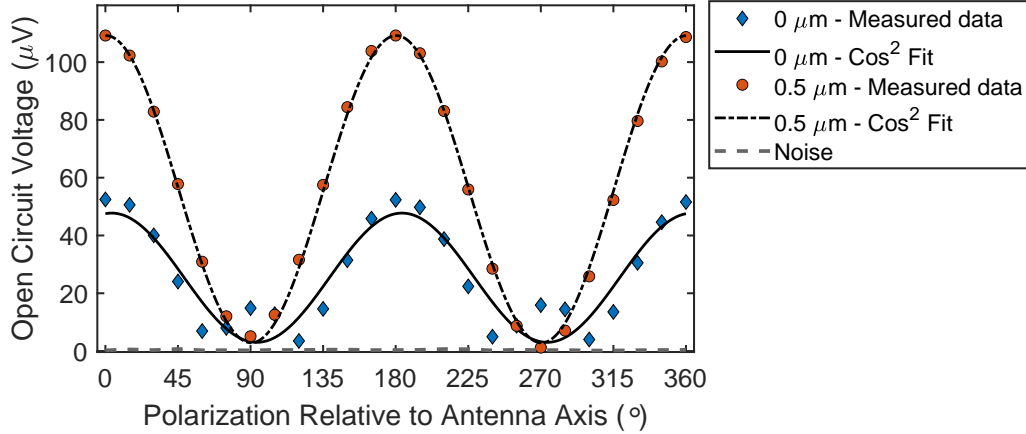


Figure 6.14:  $0$  and  $0.5 \mu\text{m}$  transmission line (TX) array measured open-circuit voltage ( $V_{oc}$ ) for a Ni/NiO/Cr/Au diode. The  $0.5 \mu\text{m}$  transmission line has a measured open-circuit voltage of  $107 \mu\text{V}$  while the  $0 \mu\text{m}$  transmission line has a voltage of  $51 \mu\text{V}$ . The laser's maximum intensity was  $1.61 \times 10^5 \text{ W/m}^2$ .  $P_{in}$  (with TX) =  $125 \mu\text{W}$  and  $P_{in}$  (no TX) =  $135 \mu\text{W}$ . For diode resistances around  $5.65 \text{ k}\Omega$ , the calculated output power and efficiency for the  $0.5 \mu\text{m}$  TX are  $P_{out} = 397 \text{ fW}$  and  $\eta = 31.6 \times 10^{-8} \%$  respectively, while for the  $0 \mu\text{m}$  TX,  $P_{out} = 90 \text{ fW}$  and  $\eta = 6.7 \times 10^{-8} \%$ . The  $0.5 \mu\text{m}$  transmission line offers around a factor of 5 improvement in total conversion efficiency compared to the no transmission line structure.

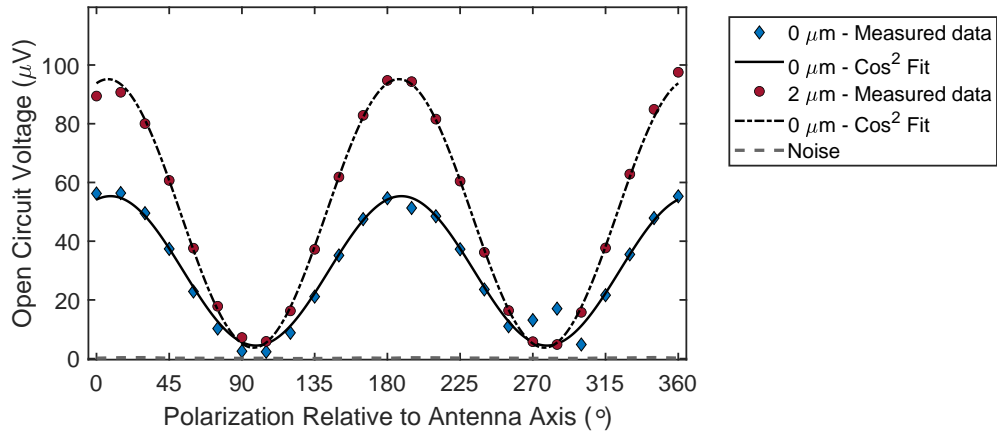


Figure 6.15: The  $0$  and  $2 \mu\text{m}$  transmission line array measured open circuit voltage ( $V_{oc}$ ) for a Ni/NiO/Cr/Au diode. The  $2 \mu\text{m}$  transmission line has a measured open-circuit voltage of  $\sim 90 \mu\text{V}$  while the  $0 \mu\text{m}$  transmission line has a voltage of  $\sim 55 \mu\text{V}$  at  $0^\circ$ ,  $180^\circ$  and  $360^\circ$  polarization angles. The laser's maximum intensity was  $1.52 \times 10^5 \text{ W/m}^2$ .  $P_{in}$  (no TX) =  $141 \mu\text{W}$  and  $P_{in}$  (with TX) =  $131 \mu\text{W}$ . For diode resistances around  $5.95 \text{ k}\Omega$ , the calculated output power and efficiency for the  $2 \mu\text{m}$  TX are  $P_{out} = 444 \text{ fW}$  and  $\eta = 35.4 \times 10^{-8} \%$  respectively, while for the  $0 \mu\text{m}$  TX,  $P_{out} = 117 \text{ fW}$  and  $\eta = 8.7 \times 10^{-8} \%$ . The  $2 \mu\text{m}$  transmission line offers around a factor of 3 improvement in total conversion efficiency compared to the no transmission line structure.

Figure 6.16 presents the measured device efficiency of each wafer along with the efficiency predicted by transmission line simulations. Efficiency increases with the transmission line length from 0 to 2  $\mu\text{m}$ . Unlike simulations, Fig. 6.10, no decrease in efficiency with transmission line length is observed. We expect this is due to variation in material properties relative to the values used in the HFSS simulation in Fig. 6.6. While simulations anticipated a nearly full rotation around the Smith chart would require a 2.5  $\mu\text{m}$  transmission line, the measured values indicated that a longer transmission line length (possible up to 6  $\mu\text{m}$ ) is required. Figure 6.16 illustrates only less than half of a full rotation. Efficiency enhancements by factors of 10 and 5 are observed for Ni/NiO/Cr/Au and Ni/NiO/Al<sub>2</sub>O<sub>3</sub>/Cr/Au diodes, respectively. The efficiency enhancement due to impedance matching is confirmed for different material sets with varying resistance and capacitance values as the diode's capacitive nature is compensated for by the antenna's inductive reactance. A second round of fabrication and measurement was conducted to increase the transmission line length to 6  $\mu\text{m}$  to observe the full predicted trend from Fig. 6.10.

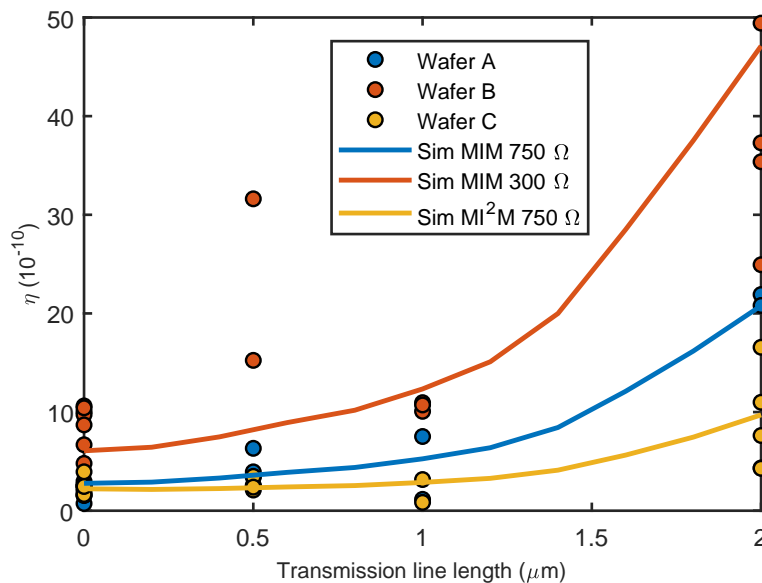


Figure 6.16: Efficiency versus transmission line length for two different material sets presented in Table 6.4, with varying oxide thicknesses and varying resistance and capacitance values. With transmission line lengths between 0 and 2  $\mu\text{m}$ , less than half a full rotation around the Smith chart is observed. Efficiency enhancements by factors of 10 and 5 are observed for Ni/NiO/Cr/Au and Ni/NiO/Al<sub>2</sub>O<sub>3</sub>/Cr/Au diodes, respectively.

## 6.7 MIM diode fabrication - extending transmission line lengths

With the aim of observing a full rotation around the Smith chart, I designed and fabricated rectennas with seventeen different transmission line lengths:  $0.5 \mu\text{m}$ ,  $0.75 \mu\text{m}$ ,  $1 \mu\text{m}$ ,  $1.25 \mu\text{m}$ ,  $1.5 \mu\text{m}$ ,  $1.75 \mu\text{m}$ ,  $2 \mu\text{m}$ ,  $2.25 \mu\text{m}$ ,  $2.5 \mu\text{m}$ ,  $2.75 \mu\text{m}$ ,  $3 \mu\text{m}$ ,  $3.25 \mu\text{m}$ ,  $3.5 \mu\text{m}$ ,  $3.75 \mu\text{m}$ ,  $4 \mu\text{m}$ ,  $5 \mu\text{m}$  and  $6 \mu\text{m}$ . The material set of choice for the second run was Ni/NiO/Cr/Au with 3 nm of sputtered NiO, as it yielded the highest conversion efficiency, discussed in the previous section. After measuring every diode's transmission line length accurately using SEM, I observed that lengths were 70 - 150 nm longer than designed. This is due to over etching the Ge, resulting in a deeper undercut and longer device length. The length variation affected the short lengths, below  $3 \mu\text{m}$ , more dramatically. SEM images of a few selected lengths are presented in Fig. 6.18, where the diode overlap region was measured to be  $\sim 0.03 \mu\text{m}^2$ . The fabricated diodes were DC tested and their open-circuit voltage polarization dependence was verified under  $10.6 \mu\text{m}$  (28.3 THz) illumination. Figure 6.17 presents the calculated total rectification efficiency as a function of length using measured  $V_{oc}$  values and measured transmission line lengths. The analytical trend was generated for a diode with a measured average zero-bias resistance of  $300 \Omega$  and a zero-bias responsivity of  $0.4 \text{ A/W}$ .

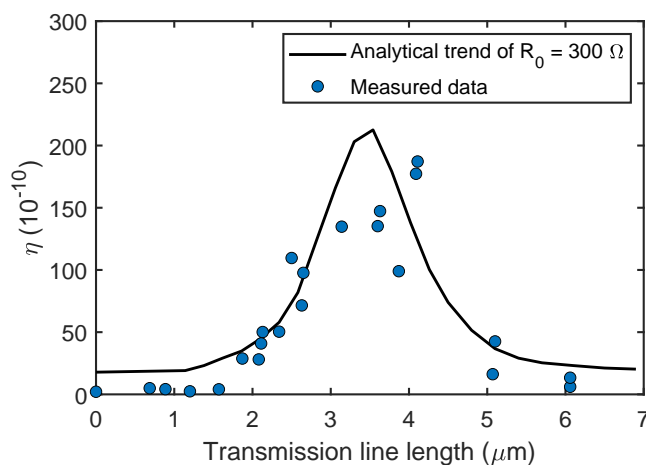


Figure 6.17: Efficiency versus transmission line length for Ni/NiO/Cr/Au diode. Measured efficiency data (circles) and calculated analytical trend (solid line) for a diode with zero-bias resistance of  $300 \Omega$ , a zero-bias responsivity of  $0.4 \text{ A/W}$  and area of  $0.03 \mu\text{m}^2$ .

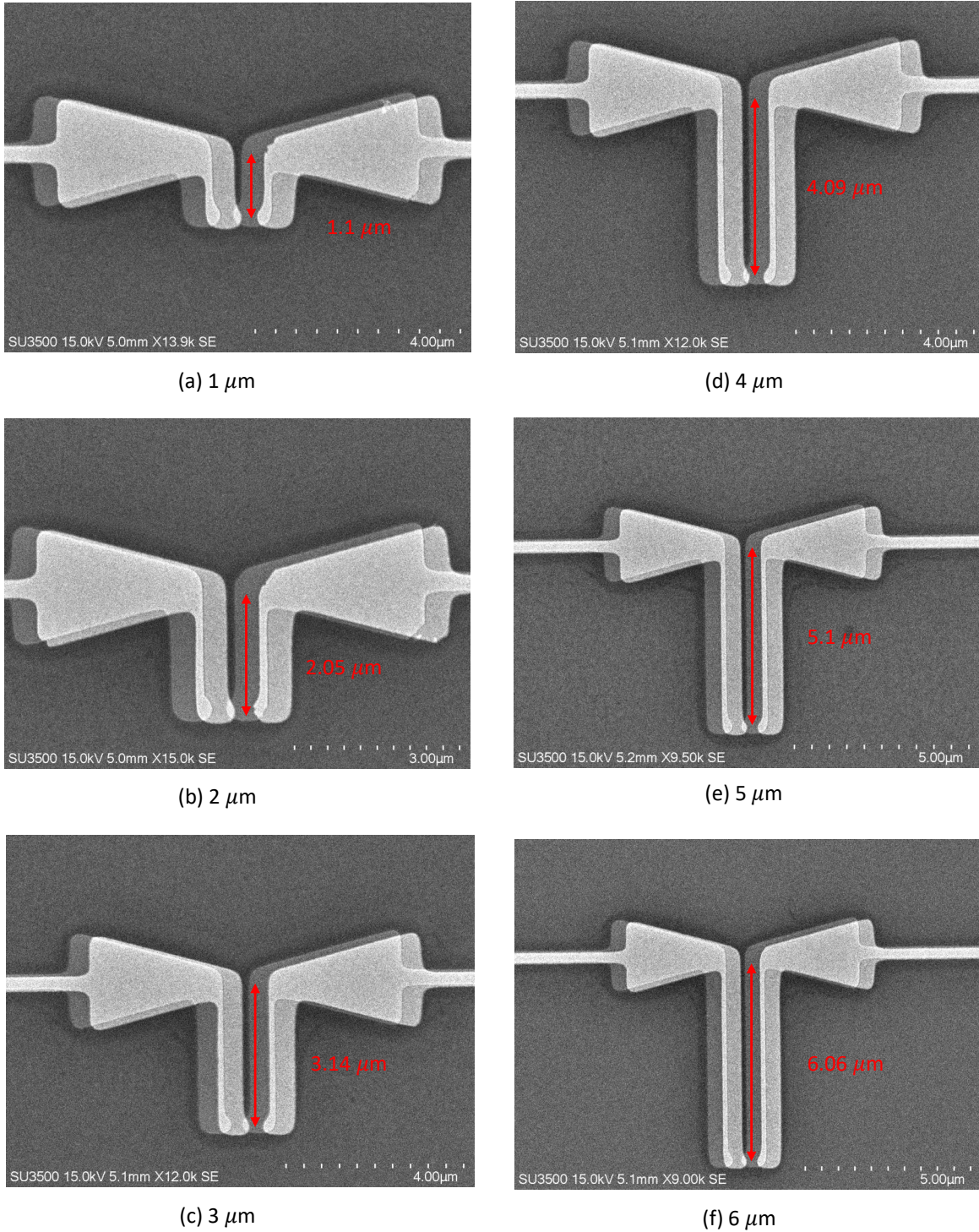


Figure 6.18: SEM images of different transmission line lengths of (a)  $1\ \mu\text{m}$  (b)  $2\ \mu\text{m}$  (c)  $3\ \mu\text{m}$  (d)  $4\ \mu\text{m}$  (e)  $5\ \mu\text{m}$  and (f)  $6\ \mu\text{m}$ . Fabricated lengths were 70 - 150 nm longer than designed due to over etched Ge, and a deeper undercut. Transmission line gaps varied between 70 and 90 nm.

While the analytical trend in Fig. 6.17 is in good agreement with measured data, certain diodes exhibited lower or higher efficiencies than expected. This can be explained with resistance and responsivity variations, as seen in Fig. 6.19 and summarized in Table 6.6. Because of oxide thickness non-uniformity across the wafer as well as small variations in diode overlap area, measured diode resistance values varied for this material set between 270 and 360  $\Omega$  and responsivity values varied between 0.35 and 0.45 A/W. Three analytical trends were generated for diodes with  $R_0 = 270, 300$  and  $340 \Omega$ , with responsivity values of  $\beta_0 = 0.35, 0.4$  and  $0.45$ , respectively and 0.2 nm thickness variation, as summarized in Table 6.6. Small deviations from these chosen diode characteristics results in efficiencies above or below the calculated analytical trend.

Table 6.6: Parameters used to calculate total efficiency of fabricated diodes due to thickness variation. Analytical trend generated using Eq. 6.3 and the waterfall diagram presented in Fig. 6.7. Diode area is kept constant at  $0.03 \mu\text{m}^2$ .

Material set	Thickness (nm)		Capacitance (fF)	$R_0$ ( $\Omega$ )	$\beta_0$ (A/W)
	NiO	$\text{Al}_2\text{O}_3$			
Ni/NiO/Cr/Au	2.8	-	0.37	350	0.35
	3	-	0.34	300	0.4
	3.2	-	0.32	350	0.45
Ni/NiO/ $\text{Al}_2\text{O}_3$ /Cr/Au	2.4	0.7	0.15	1600	0.3
	2.5	0.6	0.16	2200	0.3
	2.7	0.7	0.14	2200	0.45

Table 6.7 presents selected diodes with their measured optical characteristics and factors of improvement compared to no transmission line structures. The transmission line compensation structure has resulted in a maximum factor of 89 improvement in total conversion efficiency for the Ni/NiO/Cr/Au material set due to improvement in coupling efficiency. Figure 6.20 presents calculated total rectification efficiency as a function of length for a second material set, Ni/NiO/ $\text{Al}_2\text{O}_3$ /Cr/Au, plotted against three analytical trends using the resistance and responsivity variations summarized in 6.6. Similar enhancements are observed with transmission line length variations, where total conversion efficiency is enhanced by a maximum factor of 50, presented in Table 6.8.

Table 6.7: Measured optical characteristics and calculated efficiency of Ni/NiO/Cr/Au diodes for the no-compensation design and five transmission line lengths: 0  $\mu\text{m}$ , 1  $\mu\text{m}$ , 2  $\mu\text{m}$ , 4  $\mu\text{m}$ , 5  $\mu\text{m}$  and 6  $\mu\text{m}$ . Lengths reported in the tables are adjusted lengths measured using SEM images. The input power is calculated using measured laser intensity of  $1.6 \times 10^5 \text{ W/m}^2$ .  $R_0^{16}$  presents the measured zero-bias resistance of 16 elements in series. Efficiency is calculated as  $\eta = V_{oc}^2/R_0^{16}$ .

Transmission line length	TX ( $\mu\text{m}$ )	Devices					
		0	1.2	2.13	4.11	5.1	6.06
DC characteristics	$R_0^{16}$ (k $\Omega$ )	4.4	5.8	5.1	5.5	5.4	5.5
	Average $R_0^1$ ( $\Omega$ )	274	363	321	346	334	344
Measured optical characteristics	$V_{oc}$ ( $\mu\text{V}$ )	26	33	137	278	130	74
Input Power	$P_{in}$ ( $\mu\text{W}$ )	130	120				
Output Power	$P_{out}$ (fW)	28	31	625	2334	531	167
Total power conversion efficiency	$\eta$ ( $\times 10^{-11}$ )	2	3	50	187	43	13
Factor of improvement		-	1.2	23.9	89.1	20.3	6.4

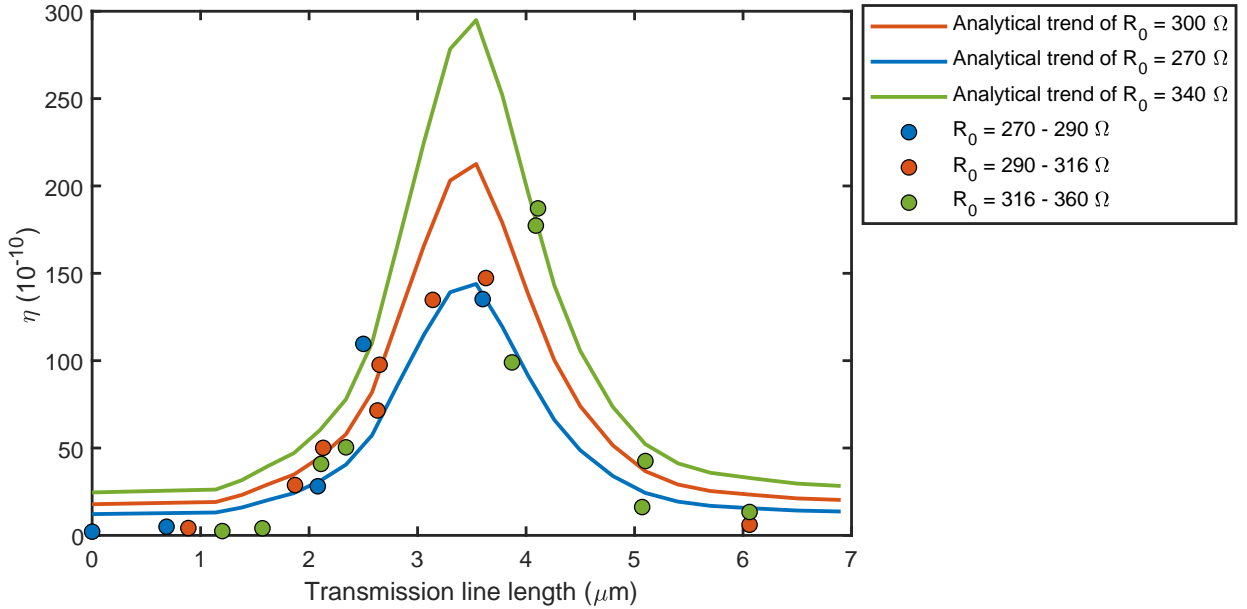


Figure 6.19: Efficiency versus transmission line length for different Ni/NiO/Cr/Au diode resistances. Because the diodes measured on this wafer vary in resistance from 270 to 360  $\Omega$ , three analytical trends were generated for diodes with  $R_0 = 270$ , 300 and 340  $\Omega$ , with responsivity values of  $\beta_0 = 0.35$ , 0.4 and 0.45, respectively. The analytical trend is in good agreement with the measured data, presented by the circles.

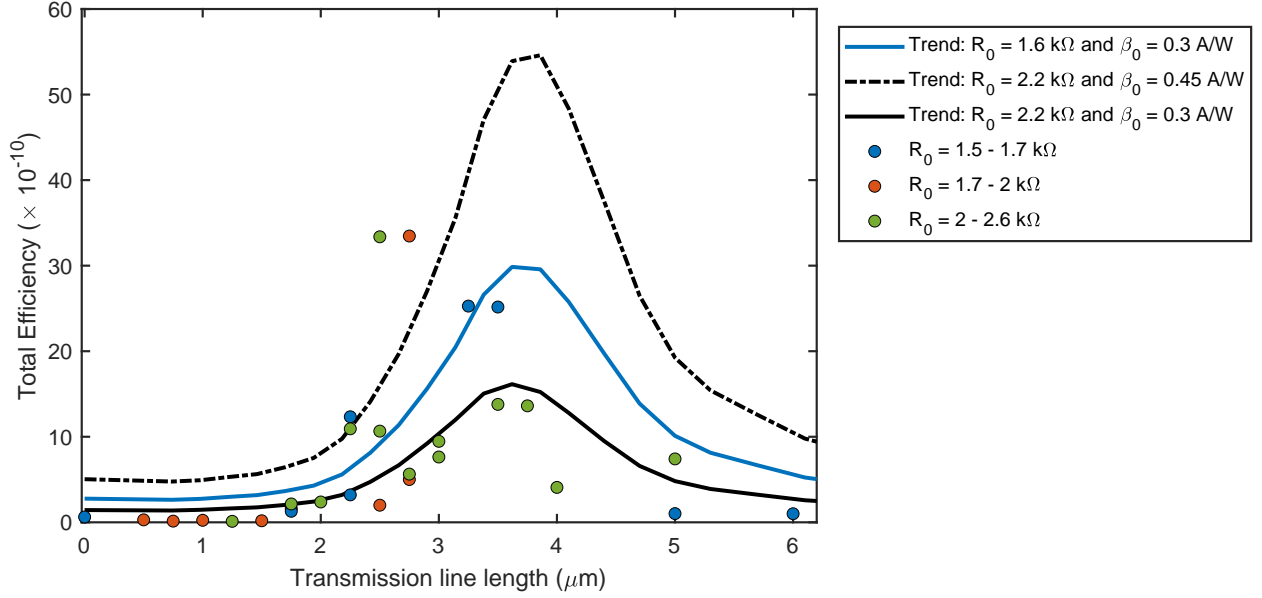


Figure 6.20: Efficiency versus transmission line length for different Ni/NiO/Al<sub>2</sub>O<sub>3</sub>/Cr/Au diode resistances. Because the diodes measured on this wafer vary in resistance from 1.5 to 2.6 k $\Omega$ , three analytical trends were generated for diodes with  $R_0 = 1.6$ , 2.2 and 2.2 k $\Omega$ , with responsivity values of  $\beta_0 = 0.35$ , 0.3 and 0.45, respectively. The analytical trend is in good agreement with the measured data, presented by the circles.

Table 6.8: Measured optical characteristics and calculated efficiency of Ni/NiO/Al<sub>2</sub>O<sub>3</sub>/Cr/Au diodes for the no compensation design and five transmission line lengths: 0  $\mu\text{m}$ , 2  $\mu\text{m}$ , 2.5  $\mu\text{m}$ , 3  $\mu\text{m}$ , 3.75  $\mu\text{m}$  and 5  $\mu\text{m}$ . The input power is calculated using measured laser intensity of  $1.6 \times 10^5$  W/m<sup>2</sup>.  $R_0^{16}$  presents the measured zero-bias resistance of 16 elements in series. Efficiency is calculated as  $\eta = V_{oc}^2/R_0^{16}$ .

		Devices					
Transmission line length	TX ( $\mu\text{m}$ )	0	2	2.5	3	3.4	5
DC characteristics	$R_0^{16}$ (k $\Omega$ )	25	26	31	32	34	34
	Average $R_0^1$ (k $\Omega$ )	1.5	2.2	2.6	2	2.1	2.1
Measured optical characteristics	$V_{oc}$ ( $\mu\text{V}$ )	40.4	92	378	175	175	160
Input Power	$P_{in}$ ( $\mu\text{W}$ )	130	120				
Output Power	$P_{out}$ (fW)	9	32	442	125	118	98
Total power conversion efficiency	$\eta$ ( $\times 10^{-11}$ )	1	3	36	10	9	8
Factor of improvement		-	4	51	14	13	11

## 6.8 Conclusion

Nearly two orders of magnitude improvement in total conversion efficiency were demonstrated using the transmission line compensation structure. In this chapter, I explored the effects of transmission line length on antenna impedance and coupling efficiency. The diode in a bowtie antenna configuration is moved from the feed-point using a transmission line. The transmission line length is varied between 0  $\mu\text{m}$  and 6  $\mu\text{m}$ , with real part of the impedance varying between 30 and 100  $\Omega$  and the imaginary part varying between capacitive and inductive. I experimentally demonstrate the effects of the transmission line compensation structure at a wavelength of 10.6  $\mu\text{m}$  using a Ni/NiO/Cr/Au MIM diode and a Ni/NiO/Al<sub>2</sub>O<sub>3</sub>/Cr/Au MI<sup>2</sup>M diode, where an improvement in total conversion efficiency is observed between transmission line lengths of 3 - 4  $\mu\text{m}$  due to the effective inductance created by the transmission line. Increasing the length of the transmission line beyond 4  $\mu\text{m}$  drops the coupling efficiency, and thus total conversion efficiency, as the antenna becomes capacitive again and no longer compensates for the diode capacitance.

## CHAPTER 7

# DEMONSTRATION OF AMBIENT HEAT HARVESTING USING OPTICAL RECTENNAS

### 7.1 Rectification through radiation

Terrestrial thermal radiation into space presents an attractive source of renewable nighttime power. The Earth's thermal radiation at ambient temperatures ( $\sim 210 - 310$  K) peaks around a wavelength of  $10 \mu\text{m}$ , as seen in Fig. 7.1. Conveniently, an atmospheric window exists between  $8$  and  $13 \mu\text{m}$  that allows radiation to pass through the atmosphere with minimal absorption and scattering. The first proposal of a system able to produce energy through Earth's thermal radiation to outer space was by Garret Moddel in 2013 (Moddel, 2017b). This radiating power converter would include an input side in thermal contact with the hot reservoir (Earth) and an output side in radiative thermal contact with the cold reservoir (outer space), as depicted in Fig. 7.2. In this manner, the Earth's ambient heat is used as an energy source which is converted to electric power using an infrared rectenna. In this chapter, I experimentally demonstrate the basic principle of thermal-to-electrical energy conversion using a Ni/NiO/Al<sub>2</sub>O<sub>3</sub>/Cr/Au MI<sup>2</sup>M diode-based optical rectenna array, with a  $2.5 \mu\text{m}$  transmission line compensation structure to enhance the coupling efficiency between antenna and diode at terahertz frequencies. I show that power can be generated from an MIM-based rectenna when the diode is maintained at room temperature and radiatively exposed to a surface colder than itself. I begin with a literature review on power generation with radiative cooling.

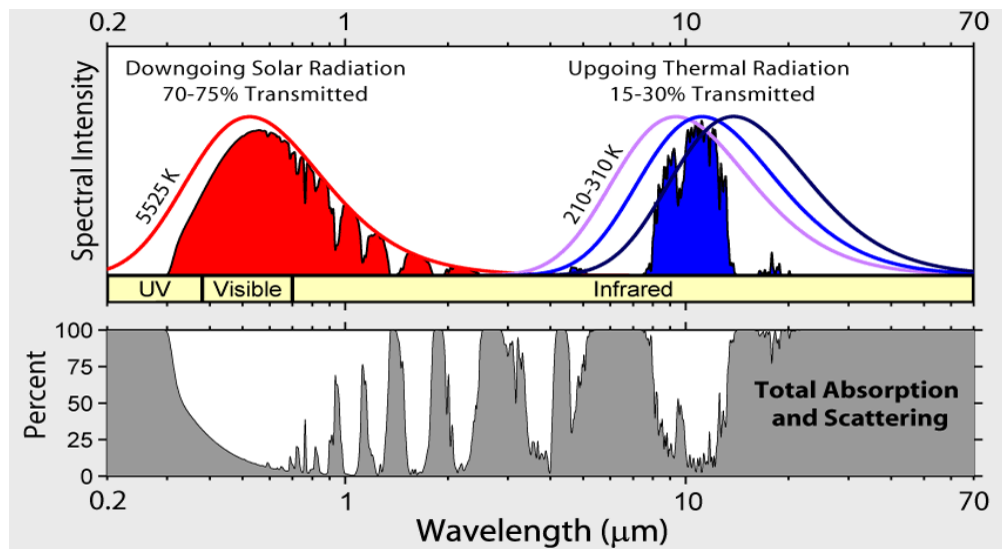


Figure 7.1: Radiation transmitted by the atmosphere, where the Earth's thermal radiation at ambient temperatures peaks around a wavelength of  $10 \mu\text{m}$  (Rohde, 2007, Rothman et al., 2005, Gordley et al., 1994). An atmospheric window exists between  $8$  and  $13 \mu\text{m}$  that allows radiation transmission with minimal absorption and scattering.

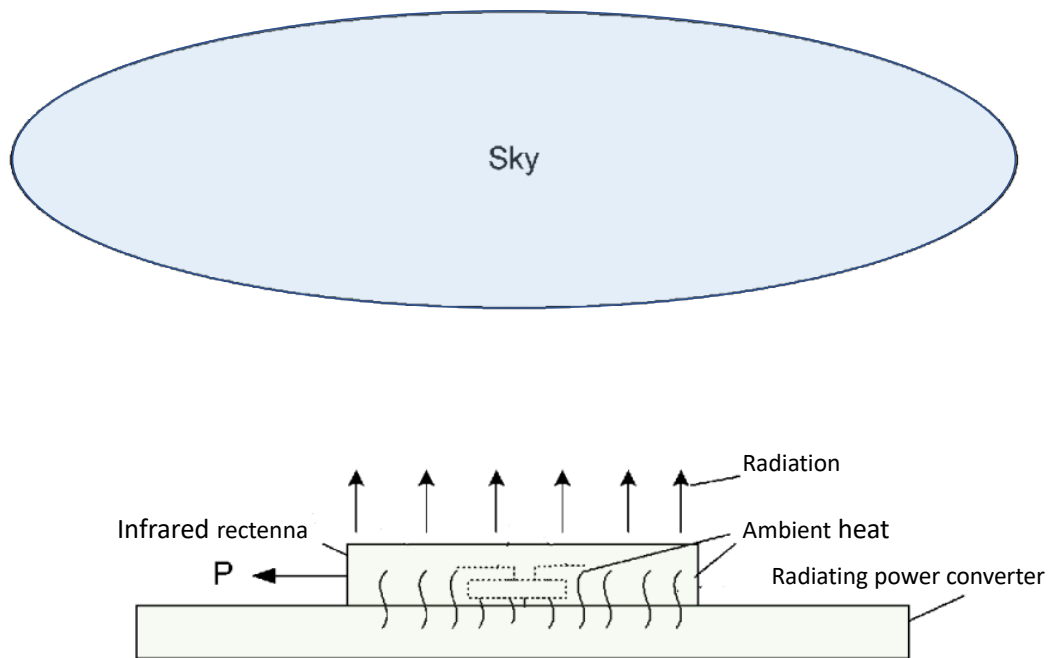


Figure 7.2: Radiating power converter patent (Moddel, 2017b). The earth provides ambient heat which is converted to power ( $P$ ) using an infrared antenna. Current fluctuations from ambient heat are converted into DC power using the rectenna diode. These fluctuations produce multi-terahertz currents that lead to radiation through the antenna.

## 7.2 Nighttime radiative cooling

Motivated by successful demonstrations of radiative cooling (Raman et al., 2014, Chen et al., 2016, Zhai et al., 2017), which used the 8 - 13  $\mu\text{m}$  atmospheric window to passively dump heat into outer space, a research group in Stanford led by Shanhui Fan has experimentally demonstrated generation of electrical power from outgoing thermal radiation using semiconductor photodiodes (Santhanam and Fan, 2016, Ono et al., 2019). In photovoltaics, the photodiode is illuminated with thermal radiation from a hot surface, and generates electrical power by absorbing incident photons and operating under the positive illumination condition, as shown in Fig. 7.3 (a). In 2016, Santhanam et al. investigated an alternative configuration where the photodiode operates under negative illumination conditions when radiatively exposed to a cold surface.

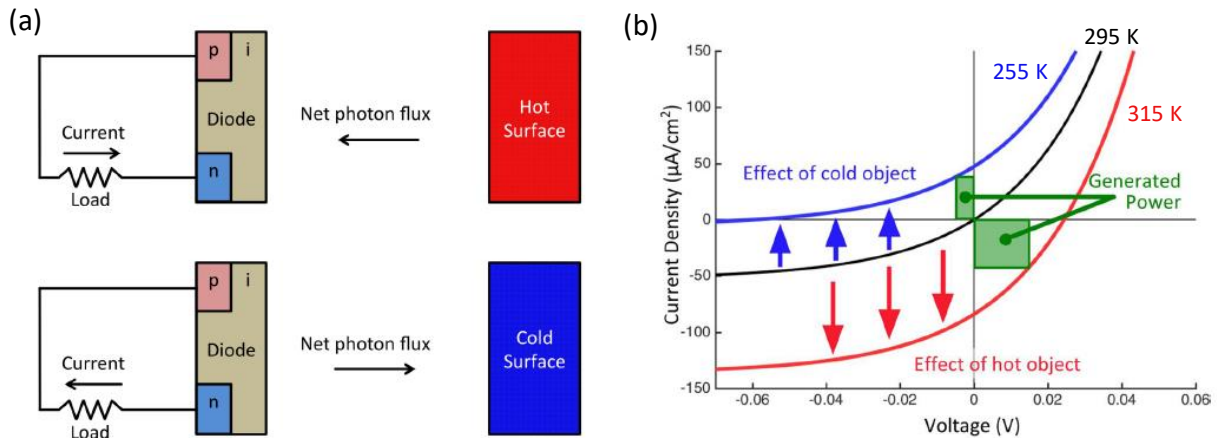


Figure 7.3: Photodiode under negative illumination condition (Santhanam and Fan, 2016). (a) Net flow of photons from a hot surface to a p-i-n diode results in a negative current, while net flow of photons from a p-i-n diode to a cold surface results in a positive current. (b)  $I(V)$  characteristics of a p-i-n photodiodes under positive (red) and negative (blue) illumination conditions.

Although the concept of using a diode on the hot side of a temperature difference has been previously proposed (Berdahl, 1985, Byrnes et al., 2014), no detailed analysis of its operation or efficiency limits appeared in literature before Santhanam et al.'s work. Fig. 7.3 (b) presents the current density of the photo diode calculated as the difference between outgoing and incoming photon fluxes at three different surface temperatures: 295 K (surface in thermal equilibrium with

the diode), 255 K (diode facing cold surface and under negative illumination) and 315 K (diode facing hot surface and under positive illumination). Both illumination conditions generate power, but in opposite quadrants, represented by the green boxes in Fig. 7.3 (b). The power conversion efficiency of such a diode under negative illumination approaches Carnot when the diode has a narrow-band emissivity (Santhanam and Fan, 2016). The maximum extractable power density from the Earth at ambient temperature ( $T = 300$  K) radiating to outer space (3 K) is estimated to be  $\sim 55$  W/m<sup>2</sup> (Buddhiraju et al., 2018). This number drops to 3.99 W/m<sup>2</sup> for an ideal photodiode

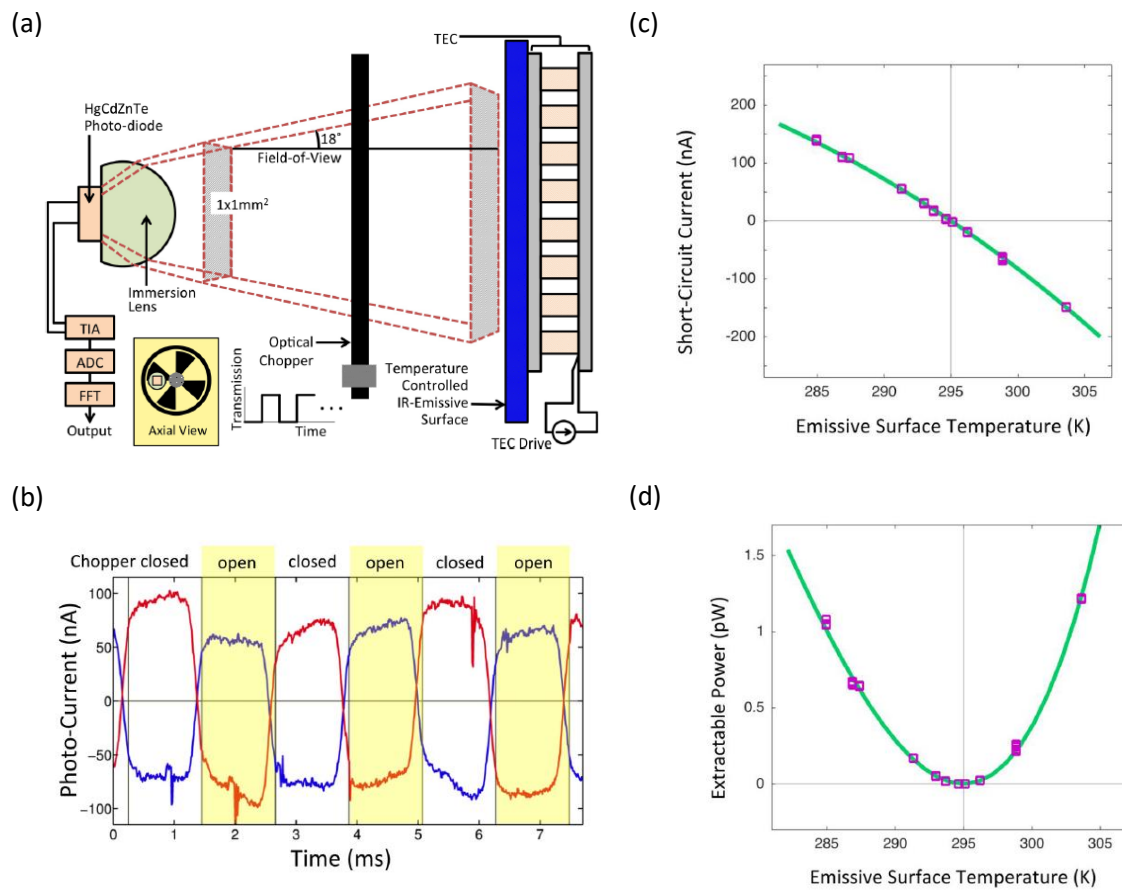


Figure 7.4: Experimental demonstration of power from negative illumination (Santhanam and Fan, 2016). (a) Experimental setup with a HgCdZnTe photodiode in an area of 1 mm<sup>2</sup> exposed to a high-emissivity surface of varying temperature. (b) Raw data of photocurrent measurements, where hot emissive surface (red) produces 150 nA and cold emissive surface produces 130 nA. (c) Short-circuit and (d) power measurements versus temperature of emissive surface. The solid line presents a theoretical model.

(with bandgap  $E_{gap}$  corresponding to  $13.2 \mu\text{m}$ ) once the effects of the atmosphere are taken into account (Ono et al., 2019).

Following their theoretical analysis, Santhanam et al. experimentally demonstrated power generated from a photodiode under negative illumination. Figure 7.4 presents the experimental setup, raw data from measurements, short-circuit current, and power versus temperature. They measure the photocurrent as a function of emissive surface temperature using a lock-in technique with an optical chopper at 415 Hz. The diode chosen for this experiment is a HgCdZnTe photodiode (Vigo's PVI-3TE-6) with a room-temperature band gap of 218 meV and a zero-bias resistance ( $R_0$ ) of  $220 \Omega$  in an area of  $1 \text{ mm}^2$ . When the emissive surface is colder than the diode, positive current is produced and when the emissive surface is hot, negative current is produced, as seen from Fig. 7.4 (b) and (c). Both configurations generate power, calculated as  $P = I_{sc}^2 R_0 / 4$ , presented in Fig. 7.4 (d). The same HgCdZnTe photodiode was later used in demonstrating extractable power from radiating to the sky directly instead of a cold emissive surface (Ono et al., 2019). For such a system, the maximum extractable power for a  $R_0 = 11.7 \text{ k}\Omega$  diode at  $T = 293 \text{ K}$  was  $P = 64 \text{ nW/m}^2$ , with an efficiency of  $\eta = 2.3 \times 10^{-5}\%$ . The input power here was calculated from the outgoing heat flux taking into account the atmospheric window transmission and the photodiode's cutoff wavelength. Table 7.1 provides a summary of theoretical limits and experimental results for energy harvesting using radiative cooling with a photodiode under negative illumination. Raman et al. recently demonstrated power generation of  $25 \text{ mW/m}^2$  using a thermoelectric device ( $ZT = 0.71$ ) facing the sky (Raman et al., 2019).

### 7.3 MIM-based rectenna for rectification through radiation

Metal-insulator-metal diodes tuned for 28.3 terahertz ( $10.6 \mu\text{m}$ ) rectification present good candidates for harvesting ambient heat generated from the Earth. In this section, I present a new approach to harvest thermal radiation using optical rectennas. Using an optical rectenna for rectification of ambient radiation requires a high rectification efficiency diode, a high coupling efficiency between the diode and antenna, and a large array of devices sufficient to produce mea-

surable power. I use the results developed in Ch. 5 and Ch. 6 to achieve sufficient rectenna performance and demonstrate rectenna rectification through radiation to a cold reservoir. I show that a Ni/NiO/Al<sub>2</sub>O<sub>3</sub>/Cr/Au MI<sup>2</sup>M diode-based optical rectenna with a 2.5  $\mu\text{m}$  transmission line compensation structure, and a staggered array design can produce power from a temperature difference. In particular, I measure power generation up to 0.5 nW/m<sup>2</sup> with a cold surface temperature  $T_c = 200$  K for a non-optimized device.

Table 7.1: Literature survey of radiative cooling energy harvesting with didoes (Santhanam and Fan, 2016, Buddhiraju et al., 2018, Ono et al., 2019).  $T_a$  and  $T_o$  are ambient and outer space temperatures, respectively.  $T_D$  and  $T_S$  present diode and emissive surface temperatures, respectively.

	Device	Assumption or setup	Temp	Output Power
Theory	Ideal photodiode	Shockley-Queisser limit $T_a = 300$ K $T_o = 3$ K	$T_D = 225.1$ K	$P = 54.8$ W/m <sup>2</sup>
		Atmospheric window		$P = 3.99$ W/m <sup>2</sup>
Experiment	HgCdZnTe photodiode	Diode facing temperature varying emissive surface $T_D = 295$ K	$T_S = 285$ K	$I = 130$ nA $P = 0.9$ $\mu\text{W}/\text{m}^2$
			$T_S = 304$ K	$I = -150$ nA $P = 1.2$ $\mu\text{W}/\text{m}^2$
		Diode facing sky	$T_D = 293$ K	$I = 0.15$ $\mu\text{A}$ $P = 64$ nW/m <sup>2</sup>

### 7.3.1 Diode staggered array design

For practical applications, MI<sup>2</sup>M diodes need to be connected in large arrays to produce useful power. Because of the extremely thin oxides (<5 nm) and sensitive nature of these diodes, individual diodes can easily be shorts or opens. Shorts occur if the thin oxide film is not uniform, thus compromising a pure parallel array connection, and opens occur when the oxide is damaged, thus rendering a pure series connection unmeasurable. One possible arraying technique for MI<sup>2</sup>M is a staggered design, a concept developed by Garret Moddel (Moddel, 2017a), presented in Fig. 7.5. The staggered design concept follows the principle that two rectennas feed into each node and

two rectennas feed out of each node, such that no two devices are in series or parallel.

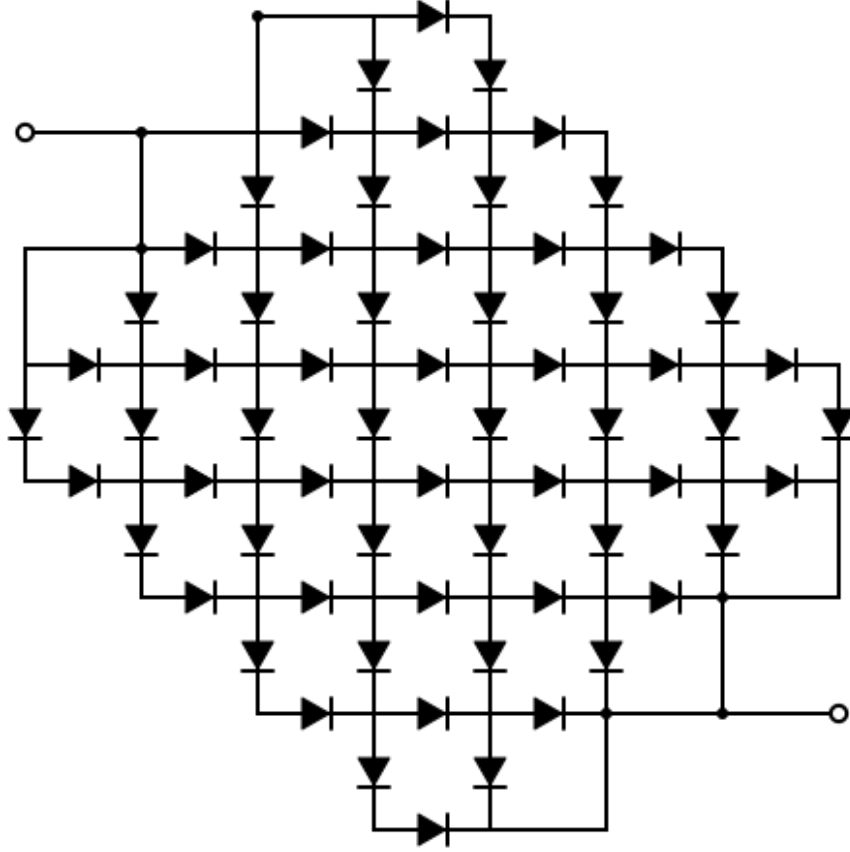


Figure 7.5: Staggered array design (Moddel, 2017a). The staggered design concept follows the principle that two rectennas feed into each node and two rectennas feed out of each node, such that no two devices are in series or parallel.

In a staggered design, the measured array  $I_A(V_A)$  characteristics can be written as (Pelz, 2019)

$$I_A(V_A) = N_p I_D \left( \frac{V_D}{N_s} \right) \quad (7.1)$$

where  $N_p$  is the number of diodes in parallel in a column,  $N_s$  is the number of diodes in series in a row,  $I_D$  and  $V_D$  are the current and voltage of a single element diode  $I_D(V_D)$ . The total current is the sum of current paths in parallel in a column and the measured applied voltage is the sum of voltage across elements in series in a row. The computed resistance and responsivity for arrays

requires the first and second derivative of current with respect to voltage where

$$I'_A = \frac{N_p}{N_s} I'_D \left( \frac{V_D}{N_s} \right) \quad (7.2)$$

$$I''_A = \frac{N_p}{N_s^2} I''_D \left( \frac{V_D}{N_s} \right). \quad (7.3)$$

Resistance and responsivity of the array system can then be defined as

$$R_A(V_A) = \frac{1}{I'_A(V_A)} = \frac{N_s}{N_p} \frac{1}{I'_D \left( \frac{V_D}{N_s} \right)} \quad (7.4)$$

$$\beta_A(V_A) = \frac{1}{2} \frac{I''(V)}{I'(V)} = \frac{1}{2} \frac{1}{N_s} \frac{I''_D \left( \frac{V_D}{N_s} \right)}{I'_D \left( \frac{V_D}{N_s} \right)}. \quad (7.5)$$

At zero bias, resistance and responsivity of a staggered array can be defined as a function of a single element resistance ( $R_0$ ) and responsivity ( $\beta_0$ ), where

$$R_A^0 = \frac{N_s}{N_p} \left( \frac{1}{I'_D(0)} \right) = \frac{N_p}{N_s} R_0 \quad (7.6)$$

$$\beta_A^0 = \frac{1}{N_s} \left( \frac{1}{2} \frac{I''_D(0)}{I'_D(0)} \right) = \frac{1}{N_s} \beta_0. \quad (7.7)$$

For a square array where  $N_s = N_p$ ,  $R_A^0 = R_0$ .

### 7.3.2 Fabrication process

I used the germanium shadow mask process to fabricate two different array sizes (4×4 and 6×6 elements) to verify the expected current-voltage relationship compared to a single diode, before extending the array size to 500×500 devices. All devices discussed in this section are Ni/NiO/Al<sub>2</sub>O<sub>3</sub>/Cu/Au diodes, fabricated with angles of  $\theta_{Ni} = \theta_{Cr/Au} = 39.5^\circ$  or  $\theta_{Ni} = \theta_{Cr/Au} = 35.9^\circ$ , with the same material set deposition conditions reported in Table 6.4 in Ch. 6. Fig. 7.6 presents SEM images of a staggered diode array with 4×4 and 6×6 devices. Fig. 7.7 presents measured  $I(V)$  characteristics and calculated responsivity and differential resistance curves as a function of voltage for three structures: a single element Ni/NiO/Al<sub>2</sub>O<sub>3</sub>/Cu/Au diode, the 16 element array in a 4×4 staggered design configuration and the 36 element array in a 6×6 staggered design configuration. Table 7.2 presents the measured zero-bias responsivity and resistance values

of the  $4 \times 4$  and  $6 \times 6$  arrays compared to their expected values from the single element zero-bias responsivity and resistance calculated using Eqs. 7.6 and 7.7. As can be seen, the measured values are in close agreement with the calculated values. Differences between measured and calculated values arise from dissimilar diodes within the array due to area differences and oxide thickness non-uniformity, as well as lead resistance.

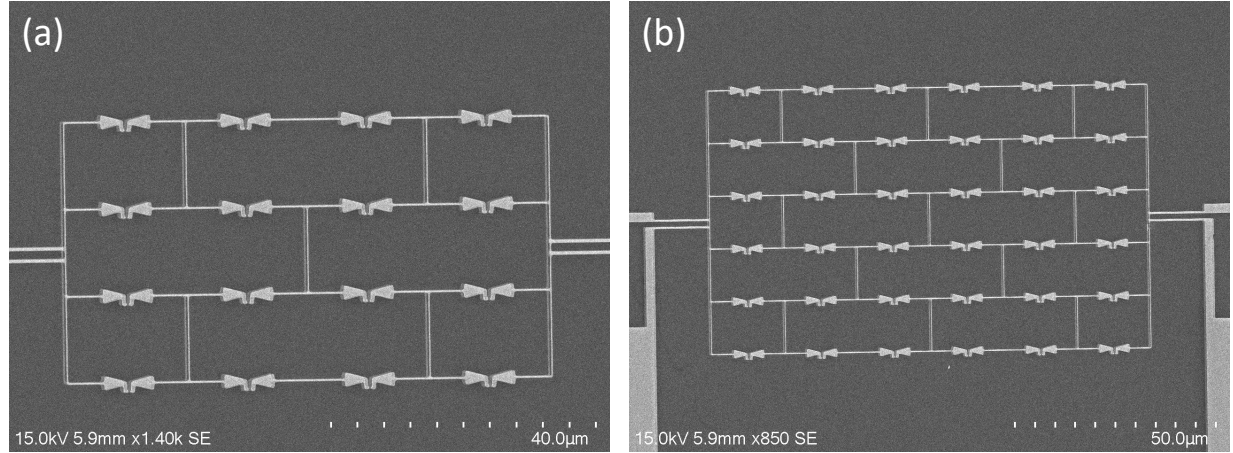


Figure 7.6: Staggered diode arrays with (a) 16 elements in a  $4 \times 4$  configuration and (b) 36 elements in a  $6 \times 6$  configuration.

Table 7.2: Responsivity and resistance of diode in a staggered design.

	Measured	Calculated ( $R_0^A = R_0$ )		Measured ( $\beta_0^A = \beta_0/N_s$ )	
	Single element	$4 \times 4$ array	$6 \times 6$ array	$4 \times 4$ array	$6 \times 6$ array
Resistance	2.56 k $\Omega$	2.56 k $\Omega$	2.56 k $\Omega$	2.97 k $\Omega$	2.65 k $\Omega$
Responsivity	0.49 A/W	0.12 A/W	0.08 A/W	0.093 A/W	0.049 A/W

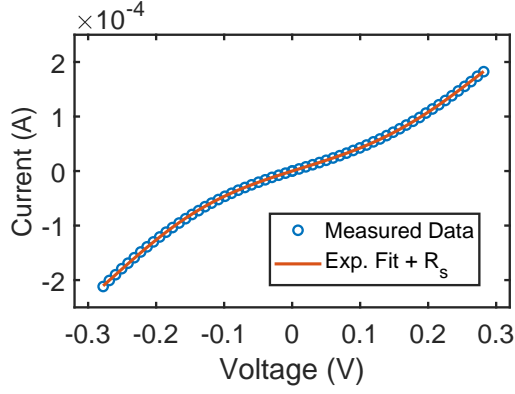
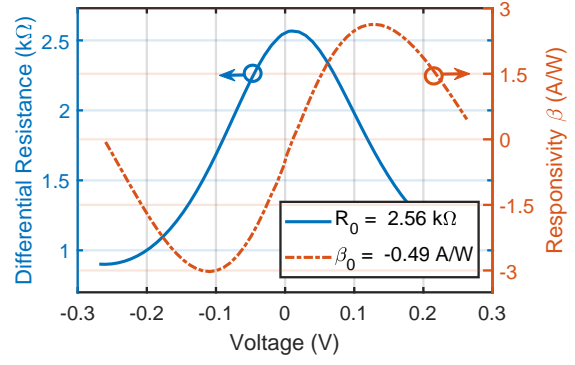
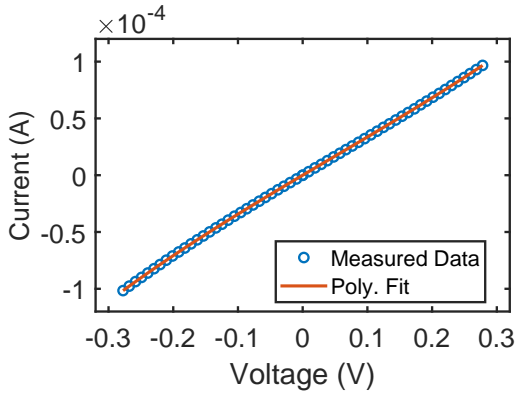
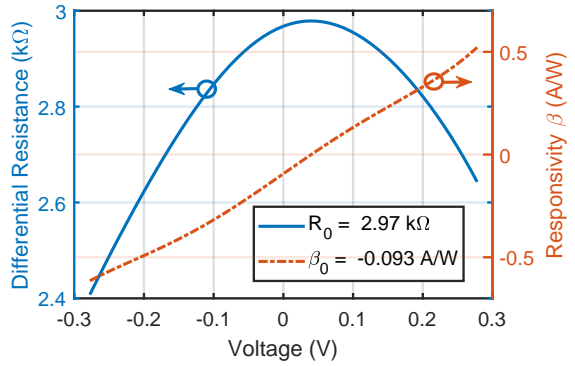
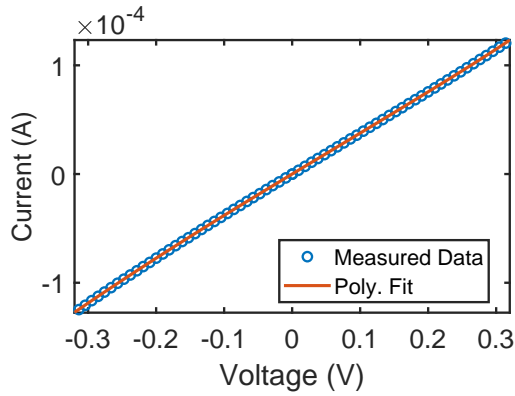
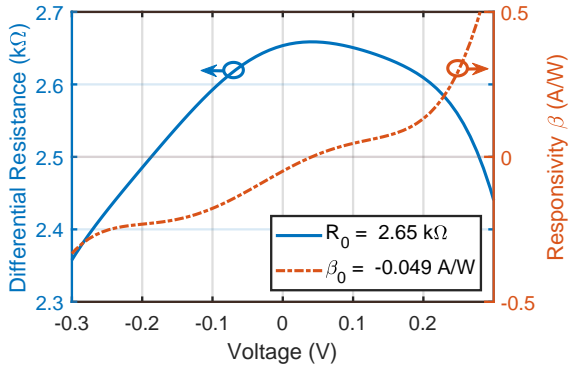
(a) Single diode  $I(V)$ (b) Single diode  $R_D(V)$  and  $\beta(V)$ (c)  $4 \times 4$  staggered array  $I(V)$ (d)  $4 \times 4$  staggered array  $R_D(V)$  and  $\beta(V)$ (e)  $6 \times 6$  staggered array  $I(V)$ (f)  $4 \times 4$  staggered array  $R_D(V)$  and  $\beta(V)$ 

Figure 7.7: Current-voltage characteristics of (a) single-element diode, (c) 16 elements in a  $4 \times 4$  configuration and (e) 36 elements in a  $6 \times 6$  configuration. Their corresponding differential resistance and responsivity curves with zero-bias resistance ( $R_0$ ) and zero-bias responsivity ( $\beta_0$ ) are presented in (b), (d) and (f), respectively. Here,  $R_0^A(4 \times 4) = R_0^A(6 \times 6) = R_0$ . Responsivity following Eq. 7.7 is  $\beta_0^A(4 \times 4) = \beta_0/4$  and  $\beta_0^A(6 \times 6) = \beta_0/6$ , as summarized in Table 7.2.

## 7.4 Experimental Setup

The experimental setup is depicted in Fig. 7.8 (a). A room-temperature Ni/NiO/Al<sub>2</sub>O<sub>3</sub>/Cr/Au rectenna array is set facing an aluminum reservoir (painted black) cooled through liquid nitrogen. The structures are arrayed in a 500 × 500 staggered array design, providing a total of 250 thousand diodes in an area of 60 mm<sup>2</sup>. Each rectenna includes a 2.5 μm transmission line compensation structure, as shown in the SEM image of the array in Fig. 7.8 (b). The temperature of the cold surface varied from ambient temperature (280 K) to a minimum temperature (180 K) as liquid nitrogen was added to the reservoir, while the diode was maintained at ambient temperature (290 K - 300 K). Thermocouples were used to monitor the temperature of both sides, and open-circuit voltage was measured using a high-impedance voltmeter. Figure 7.8 (c) presents raw data from

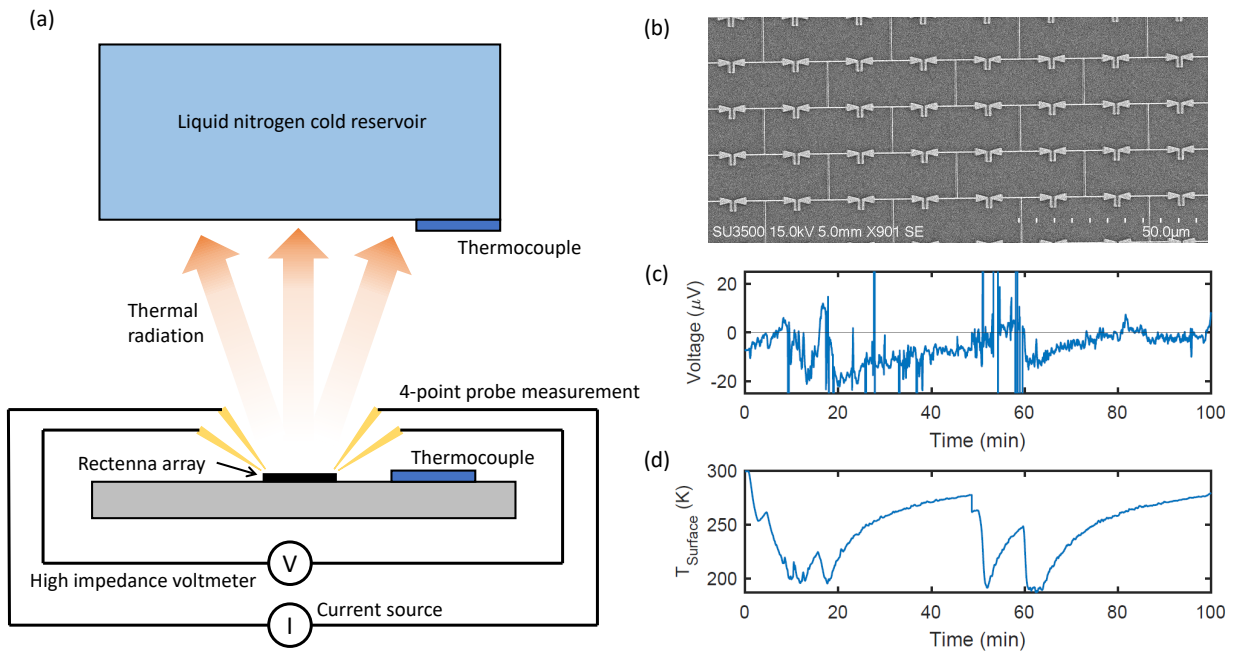


Figure 7.8: Diagram of the experimental setup. An array of diodes was exposed to a cold reservoir filled with liquid nitrogen. The MI<sup>2</sup>M diode array was maintained at temperature a constant temperature (between 290 and 300 K), while the cold reservoir's temperature varied between 180 and 280 K. Temperatures were monitored using thermocouples. (b) SEM image of a small area of the 500 × 500 staggered rectenna array. (c) Raw data from open-circuit voltage measurements. (d) Temperature of rectenna field of view. The temperature variation at  $t = 50$  min is due to adjustments to the thermocouple.

open-circuit voltage measurements and Fig. 7.8 (d) presents the temperature of the surface above the rectenna array. Rectenna temperature was maintained at  $T_{rectenna} = 290$  K and 300 K, between  $t = 0 - 50$  min and  $t = 50 - 100$  min, respectively. Liquid nitrogen was added into the reservoir set above the array at  $t = 0$  and  $t = 50$  min. As the liquid nitrogen evaporated, the reservoir temperature returned to room temperature. Noise spikes were observed when liquid nitrogen was added to the reservoir, causing the voltage probes to shake. Following the analysis for outgoing thermal radiation with an intermediate blackbody (Buddhiraju et al., 2018), the work extracted by a Carnot engine is  $W = \sigma(T_i^4 - T_c^4)(T_a/T_i - 1)$  where  $\sigma$  is the Stephan-Boltzmann constant. For the ambient temperature of  $T_a = 300$  K, a cold reservoir temperature of  $T_c = 148$  K and an intermediate temperature of  $T_i = 237$  K, the maximum power density this system can produce is  $40$  W/m<sup>2</sup>.

## 7.5 Results

Figure 7.9 presents raw data from open-circuit voltage and temperature measurements, as well as measured  $V_{oc}$  and calculated power ( $P = 0.25 \times V_{oc}^2/R_0$ ) versus temperature of the cold reservoir for  $T_{rectenna} = 290$  and 300 K. The raw data intervals were selected to highlight the exponential falloff as the temperature of the reservoir came to room temperature. MI<sup>2</sup>M diodes are operated in reverse self-bias under both positive and negative illumination conditions, and the diode  $I(V)$  is shifted up compared to equilibrium. Because of the low asymmetry of the diode near zero bias, it is a good assumption to use the zero-bias resistance to calculate output power. The zero-bias resistance of the rectenna array at room temperature was measured to be  $R_0^A = 4.0$  k $\Omega$  for a single diode zero-bias resistance of  $R_0 = 2.0$  k $\Omega$ . This indicates that the staggered array design is no longer a square array as  $N_p > N_s$  due to shorts in the system. A section of the array is shown in Fig. 7.8 (b). Using a Ni/NiO/Al<sub>2</sub>O<sub>3</sub>/Cr/Au diode rectenna with  $2.5$   $\mu$ m transmission line length, an output power of  $0.5$  nW/m<sup>2</sup> was measured with  $V_{oc} = 22$   $\mu$ V and  $I_{sc} = 5.5$  nA at a temperature gradients  $\Delta T = 100$  K. Also included in Fig. 7.9 are trends from the theoretical model discussed in Ch. 2, where open-circuit voltage has a linear relationship with temperature.

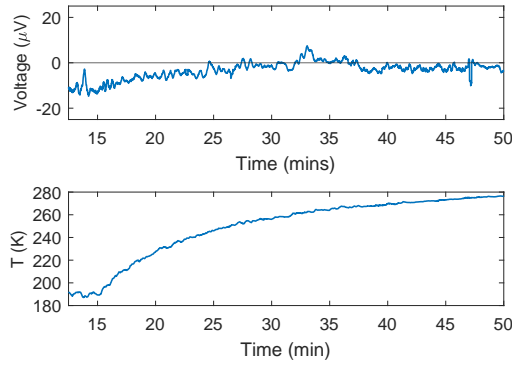
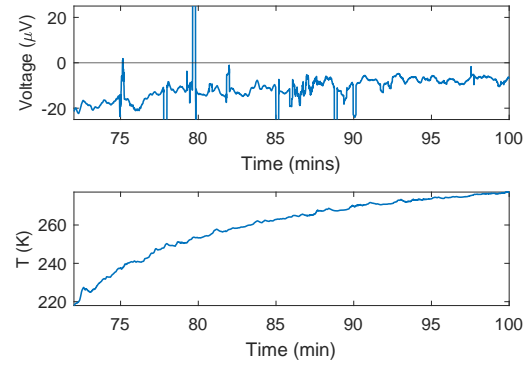
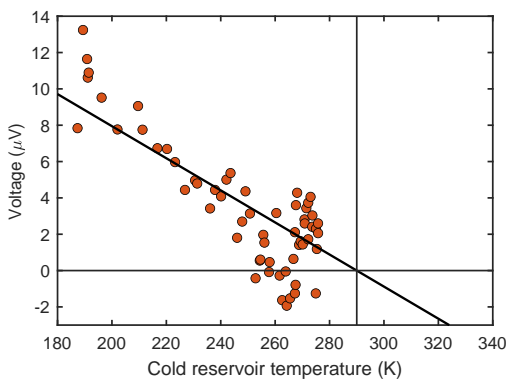
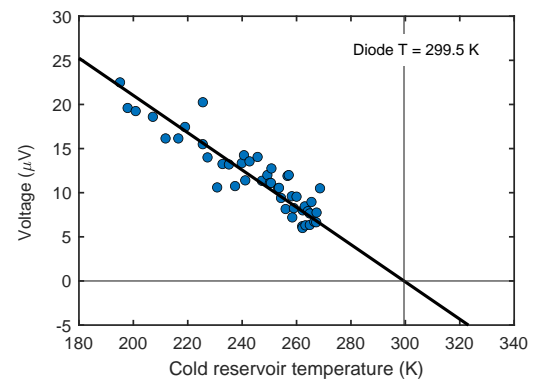
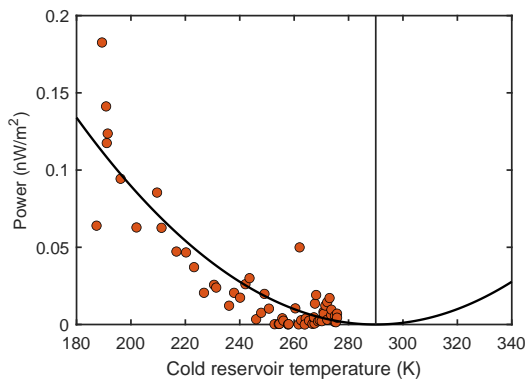
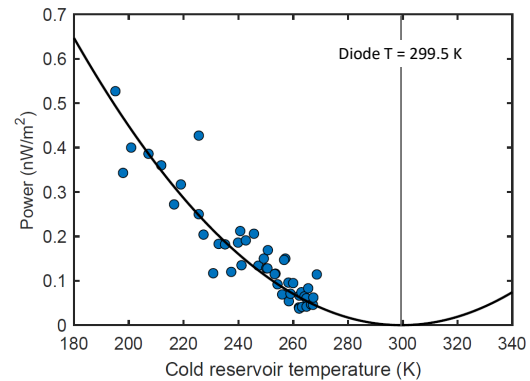
(a) The  $V_{oc}$  raw data for  $T_{rectenna} = 290$  K.(b) The  $V_{oc}$  raw data for  $T_{rectenna} = 299.5$  K.(c) The  $V_{oc}$  for  $T_{rectenna} = 290$  K.(d) The  $V_{oc}$  for  $T_{rectenna} = 299.5$  K.(e) The  $P$  for  $T_{rectenna} = 290$  K.(f) The  $P$  for  $T_{rectenna} = 299.5$  K.

Figure 7.9: Open-circuit voltage and power versus temperature of the cold reservoir for  $T_{rectenna} = 290$  and  $300$  K, respectively. (a) and (b) are intervals of Fig. 7.8 (c) and Fig. 7.8 (d). The discrete points represent measured data and the solid line represent the expected voltage/temperature and power/temperature relationships from simulations.

As the temperature of the reservoir got colder, a higher open-circuit voltage is measured and a higher power is generated.

The input power to the system can be calculated as the new heat flow through radiation between the hot and cold surfaces. At  $T = 300$  K, the maximum total power radiated is  $459$  W/m<sup>2</sup>. That corresponds to  $115$  nW of available input power per rectenna system. With an antenna efficiency of  $8.5\%$  (Fig. 6.3) and a coupling efficiency of  $2\%$  (Fig. 6.8), following the analysis in Ch. 6, the available power for rectification per diode is  $196$  pW, as shown in the power waterfall diagram in Fig. 7.10. For a much higher diode input power of  $10$  mW, the diodes self-biases at  $10$

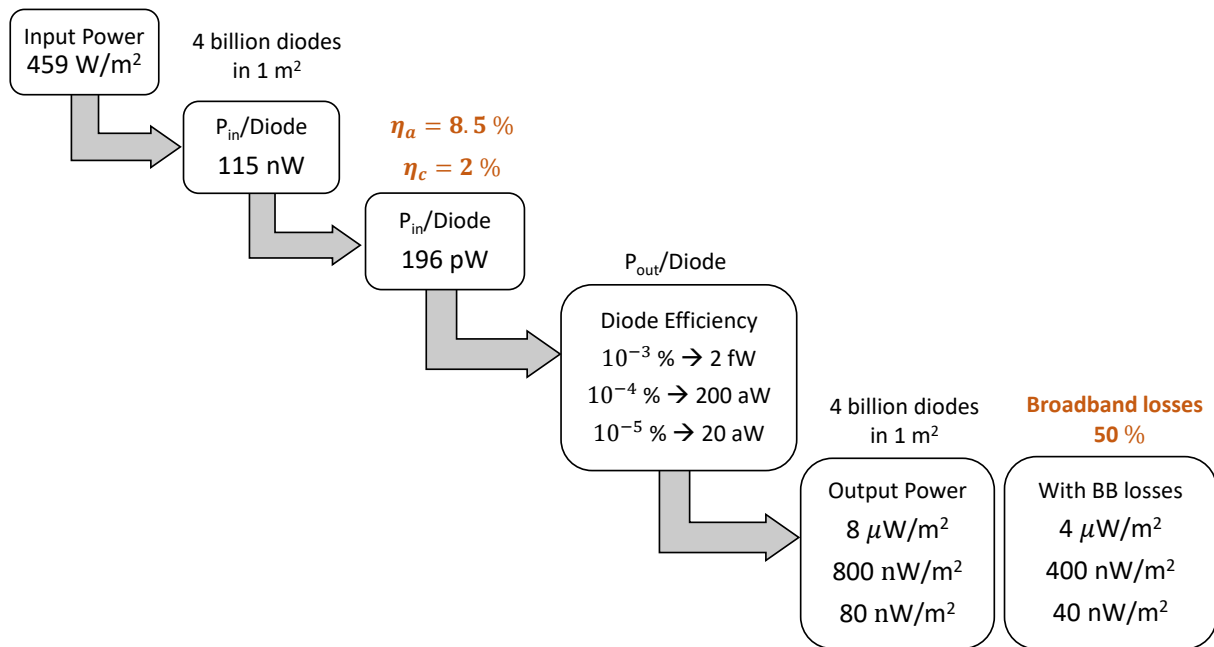


Figure 7.10: Radiating rectenna power waterfall diagram. At  $T = 300$  K, the total power radiated is  $459$  W/m<sup>2</sup>. With an antenna efficiency of  $8.5\%$  and a coupling efficiency of  $2\%$ , following the analysis in Ch. 6, the available power for rectification per diode is  $196$  pW. The low input power results in low rectification efficiencies.

$\mu$ V and has a rectification efficiency between  $10^{-2}\%$  and  $10^{-3}\%$  (Pelz, 2018, Jayaswal et al., 2018). Here, because of the low input power, the diode self biases at extremely low voltages ( $< 100$  nV) and results in low diode rectification efficiencies between  $10^{-4}\%$  and  $10^{-5}\%$ . Because the rectenna

system is designed to maximize performance at a single frequency, a 3 dB roll-off corresponds to at 50% losses which results in an output power between 40 and 400 nW/m<sup>2</sup>. Our measured value of 0.5 nW/m<sup>2</sup> agrees well with simplistic analysis. A more accurate value is expected once all system losses are taken into account.

## 7.6 Conclusion

In this chapter, I have analyzed a new approach for extracting electrical work from a hot body radiating into a cold reservoir using MI<sup>2</sup>M-based optical rectennas. The maximum extractable power for a hot surface of temperature  $T = 300$  K radiating to a cold reservoir of temperature  $T = 200$  K using a Ni/NiO/Al<sub>2</sub>O<sub>3</sub>/Cr/Au diodes with a 2.5  $\mu$ m transmission line compensation structure is 0.5 nW/m<sup>2</sup>. Such a demonstration of power generation using an MI<sup>2</sup>M-based optical rectennas has not been previously reported. The main limitations of the system are the low diode rectification efficiency due to the low input power and the low antenna and coupling efficiencies. These results pave the way towards using this technology and radiative cooling to extract power from the Earth radiation into outer space, where the diode temperature is either supplied from the Earth by conduction or from the ambient air by convection, enabling night-time power generation.

## CHAPTER 8

### CONCLUSIONS AND FUTURE WORK

I have explored the possibility of power generation using MI<sup>2</sup>M-based optical rectennas maintained at room temperature and radiatively exposed to a surface colder than itself. This work provides a first step in showing how this process can be realized with rectennas, potentially for applications such as nighttime power generation. Unlike the conventional operation of rectennas where power generation occurs through the absorption of radiation, rectennas in this configuration produce power through thermal radiation to a cold reservoir. I experimentally demonstrated the basic principle of thermal-to-electrical energy conversion from a hot surface of temperature  $T = 300$  K radiating to a cold reservoir of temperature  $T = 200$  K using an array of 250,000 rectennas. The measured power at a temperature difference of 100 K is  $0.5 \text{ nW/m}^2$ . This is achieved using a Ni/NiO/Al<sub>2</sub>O<sub>3</sub>/Cr/Au MI<sup>2</sup>M diode with a  $2.5 \text{ }\mu\text{m}$  transmission line compensation structure to modify the impedance of the antenna seen by the diode. This modification results in a coupling efficiency of 2%, nearly 50 times higher than the no-compensation design. The addition of a transmission line makes the bowtie antenna inductive, thus providing compensation to the inherently capacitive MI<sup>2</sup>M diodes.

Increasing the total efficiency and consequently the total power generated requires better understanding of MI<sup>2</sup>M diodes to achieve high asymmetries at low voltages. To do so, I have fabricated hundreds of MIM diodes of with different material sets and properties using the Ge shadow mask process. The  $I(V)$  characteristics of these diodes were measured and simulated using a quantum tunneling simulator. Parameters such as diode area and oxide thicknesses were measured

using SEM images and ellipsometry. I determined the barrier heights by adjusting material work functions and electron affinities to achieve a good fit with experiments. This process worked well for single-insulator MIM diodes where all the voltage is applied across a single oxide, but not for multi-insulator structures where voltage division across the oxides is dependent on both tunneling resistance and oxide capacitance. The misconception that the DC voltage drop across multi-insulator MIM diodes depends on capacitive voltage division has resulted in large errors between designed and fabricated diodes. The correct method of dividing the voltage across the two insulators layers in DC is through resistive voltage division. Even though tunneling in an MI<sup>2</sup>M diode goes through the entire structure and cannot be physically divided into two resistance values that sum to the total resistance, a fictitious resistance method can be used to achieve accurate fits of DC  $I(V)$  characteristics.

Resonant tunneling effects in Ni/NiO/Al<sub>2</sub>O<sub>3</sub>/Cr/Au MI<sup>2</sup>M diodes were analyzed and demonstrated, where the usual trend of increasing resistance with responsivity for diode thickness variations was reversed, and a reduction in resistance was observed with an increase in responsivity. Increasing the thickness of NiO in MI<sup>2</sup>M diodes allows for the modification of the  $I(V)$  characteristics by altering the depth and width of the quantum well formed between the two oxides. Deep wells are necessary to reach quasi-bound states at low voltages necessary for energy harvesting applications. Even though resonant tunneling in MIM diodes has drawn significant attention in recent years, there have been no experimental reports of resonant tunneling effects at the low voltages needed for high frequency rectenna applications. This is due to the difficulty of building low-barrier height diodes with wells deep and wide enough, and fabrication limitations such as sub-nanometer control of thickness. Resonant tunneling was observed in Ni/NiO/Al<sub>2</sub>O<sub>3</sub>/Cr/Au MI<sup>2</sup>M diodes due to the low diode barrier created between Ni and NiO ( $\sim 0.15$  eV) as well as the careful control of NiO and Al<sub>2</sub>O<sub>3</sub> thicknesses. The total energy conversion efficiency of these diode-based rectennas surpasses every reported value in literature, achieving over a factor of 100 improvement over state-of-the-art.

Several topics for future areas of research follow directly from the material presented throughout this thesis.

- (1) **Innovative antenna designs:** The simplest approach to improving diodes for optical rectification is to provide more power to the diodes. This means increasing the amount of optical power absorbed by the antenna ( $\eta_a$ ) and the amount of power delivered to the diode ( $\eta_c$ ). In current designs, incident radiation is not fully absorbed due to the high permittivity Si substrate, limiting  $\eta_a$  to 8.5%. Alternative substrates such as silica glass or sapphire wafers would improve antenna absorption but would require considerable modifications to the current fabrication process or a completely new one. The addition of a transmission line compensation structure has increased  $\eta_c$  to 2%. Achieving a 100% coupling efficiency requires an innovative antenna or compensation structure with low resistance to perfectly match the low series-equivalent resistance of the diode and an inductive reactance to compensate for the diode capacitance.
- (2) **Improved diodes:** The diode is and remains the most important and challenging part of the rectenna system. Diodes for efficient power conversion need high asymmetries and low resistance and capacitance values. High asymmetries near zero-bias correspond to high responsivity values, high rectification efficiencies and more power generation. In MIM diodes, the most common methods to increase asymmetry also increase resistance, forcing a trade-off between rectification and coupling efficiency enhancements. One solution proposed and demonstrated in this work is resonant tunneling, which increases responsivity while decreasing resistance, thus increasing both rectification and coupling efficiencies. Additional innovations are needed to improve MIM diode rectification efficiency beyond its current  $10^{-3}\%$  value. The improvements must extend to high frequencies where the diodes are operated for energy harvesting.

## BIBLIOGRAPHY

- Abdolkader, T. M., Shaker, A., and Alahmadi, A. (2018). Numerical simulation of tunneling through arbitrary potential barriers applied on MIM and MIIM rectenna diodes. European Journal of Physics, 39(4):045402.
- Alimardani, N. and Conley Jr, J. F. (2014). Enhancing metal-insulator-insulator-metal tunnel diodes via defect enhanced direct tunneling. Applied Physics Letters, 105(8):082902.
- Apell, S. and Penn, D. R. (1992). Photoinduced resonant tunneling treated by an extended transfer hamiltonian method. Physical Review B, 45(12):6757.
- Aranguren, P., Araiz, M., Astrain, D., and Martínez, A. (2017). Thermoelectric generators for waste heat harvesting: A computational and experimental approach. Energy Conversion and Management, 148:680–691.
- Arsoy, E. G., Inac, M., Shafique, A., Ozcan, M., and Gurbuz, Y. (2016). The metal-insulator-metal diodes for infrared energy harvesting and detection applications. In Infrared Technology and Applications XLII, volume 9819, page 98190F. International Society for Optics and Photonics.
- Auton, G., But, D. B., Zhang, J., Hill, E., Coquillat, D., Consejo, C., Nouvel, P., Knap, W., Varani, L., Teppe, F., et al. (2017). Terahertz detection and imaging using graphene ballistic rectifiers. Nano letters, 17(11):7015–7020.
- Bakshi, A. (2009). Transmission lines and waveguide. Technical Publications.
- Bareiß, M., Krenz, P. M., Szakmany, G. P., Tiwari, B. N., Kalblein, D., Orlov, A. O., Bernstein, G. H., Scarpa, G., Fabel, B., Zschieschang, U., and Klauk, H. (2013). Rectennas revisited. IEEE Transactions on Nanotechnology, 12(6):1144–1150.
- Bean, J. A., Tiwari, B., Bernstein, G. H., Fay, P., and Porod, W. (2009). Thermal infrared detection using dipole antenna-coupled metal-oxide-metal diodes. Journal of Vacuum Science & Technology B: Microelectronics and Nanometer Structures Processing, Measurement, and Phenomena, 27(1):11–14.
- Bean, J. A., Weeks, A., and Boreman, G. D. (2011). Performance optimization of antenna-coupled Al AlO Pt tunnel diode infrared detectors. IEEE Journal of Quantum Electronics, 47(1):126–135.
- Belenov, É. M., Kompanets, I., Popov, Y. M., Poluékto, I., Sagitov, S., Soboleva, E., Sobolev, A., Uskov, A. V., and Tsukanov, V. (1982). Amplification of surface plasma oscillations in complex metal–barrier–metal structures. Soviet Journal of Quantum Electronics, 12(7):930.

- Belkadi, A., Weerakkody, A., and Moddel, G. (2018). Large errors from assuming equivalent DC and high-frequency electrical characteristics in metal–multiple-insulator–metal diodes. ACS Photonics, 5(12):4776–4780.
- Bell, L. E. (2008). Cooling, heating, generating power, and recovering waste heat with thermoelectric systems. Science, 321(5895):1457–1461.
- Berdahl, P. (1985). Radiant refrigeration by semiconductor diodes. Journal of applied physics, 58(3):1369–1374.
- Bhatt, K., Kumar, S., and Tripathi, C. C. (2019). Highly sensitive al/al<sub>2</sub>o<sub>3</sub>/ag mim diode for energy harvesting applications. AEU-International Journal of Electronics and Communications, 111:152925.
- Boltzmann, L. and Brush, S. G. (1964). Lectures on Gas Theory. Translated by Stephen G. Brush. University of California Press.
- Brillouin, L. (1950). Can the rectifier become a thermodynamical demon? Physical Review, 78(5):627.
- Briones, E., Alda, J., and González, F. J. (2013). Conversion efficiency of broad-band rectennas for solar energy harvesting applications. Optics express, 21(103):A412–A418.
- Brown, W. C. (1984). Performance characteristics of the thin-film, etched-circuit rectenna. pages 365–367.
- Buddhiraju, S., Santhanam, P., and Fan, S. (2018). Thermodynamic limits of energy harvesting from outgoing thermal radiation. Proceedings of the National Academy of Sciences, 115(16):E3609–E3615.
- Byrnes, S. J., Blanchard, R., and Capasso, F. (2014). Harvesting renewable energy from earth’s mid-infrared emissions. Proceedings of the National Academy of Sciences, 111(11):3927–3932.
- Chen, Z., Zhu, L., Raman, A., and Fan, S. (2016). Radiative cooling to deep sub-freezing temperatures through a 24-h day–night cycle. Nature communications, 7:13729.
- Chu, S. and Majumdar, A. (2012). Opportunities and challenges for a sustainable energy future. nature, 488(7411):294.
- Cowell III, E. W., Alimardani, N., Knutson, C. C., Conley Jr, J. F., Keszler, D. A., Gibbons, B. J., and Wager, J. F. (2011). Advancing mim electronics: Amorphous metal electrodes. Advanced Materials, 23(1):74–78.
- Cowley, A. and Sorensen, H. (1966). Quantitative comparison of solid-state microwave detectors. IEEE Transactions on Microwave Theory and Techniques, 14(12):588–602.
- Dayem, A. and Martin, R. (1962). Quantum interaction of microwave radiation with tunneling between superconductors. Physical Review Letters, 8(6):246.
- Dees, J. (1966). Detection and harmonic generation in the submillimeter wavelength region(harmonic generation and detection in submillimeter wavelength region, emphasizing crystal point contact diode). Microwave Journal, 9:48–55.

- DiSalvo, F. J. (1999). Thermoelectric cooling and power generation. *Science*, 285(5428):703–706.
- Drury, D. and Ishii, T. (1980). A stimulated inelastic tunneling theory of negative differential resistance in metal-insulator-metal diodes. *IEEE Journal of Quantum Electronics*, 16(1):58–69.
- Eliasson, B. J. (2001). Metal-insulator-metal diodes for solar energy conversion. PhD thesis, University of Colorado.
- Eliasson, B. J. and Moddel, G. (2003). Metal-oxide electron tunneling device for solar energy conversion. US Patent 6,534,784.
- Fan, S., Zhao, J., Guo, J., Yan, Q., Ma, J., and Hng, H. H. (2010). p-type  $\text{b}_{0.4}\text{sb}_{1.6}\text{te}_3$  nanocomposites with enhanced figure of merit. *Applied Physics Letters*, 96(18):182104.
- Fumeaux, C., Herrmann, W., Kneubühl, F., and Rothuizen, H. (1998). Nanometer thin-film Ni–NiO–Ni diodes for detection and mixing of 30 THz radiation. *Infrared physics & technology*, 39(3):123–183.
- González, F. and Boreman, G. (2005). Comparison of dipole, bowtie, spiral and log-periodic ir antennas. *Infrared Physics & Technology*, 46(5):418–428.
- Gordley, L. L., Marshall, B. T., and Chu, D. A. (1994). Linepak: Algorithms for modeling spectral transmittance and radiance. *Journal of Quantitative Spectroscopy and Radiative Transfer*, 52(5):563–580.
- Green, M. A. (2012). Analytical treatment of trivich–flinn and shockley–queisser photovoltaic efficiency limits using polylogarithms. *Progress in Photovoltaics: Research and Applications*, 20(2):127–134.
- Grover, S. (2011). Diodes for optical rectennas. PhD thesis, University of Colorado Boulder.
- Grover, S., Joshi, S., and Moddel, G. (2013). Quantum theory of operation for rectenna solar cells. *Journal of Physics D: Applied Physics*, 46(13):135106.
- Grover, S. and Moddel, G. (2012). Engineering the current–voltage characteristics of metal–insulator–metal diodes using double-insulator tunnel barriers. *Solid-State Electronics*, 67(1):94–99.
- Grover, S. and Moddel, G. (2013). Metal single-insulator and multi-insulator diodes for rectenna solar cells. In *Rectenna Solar Cells*, pages 89–109. Springer.
- Hashem, I. E., Rafat, N. H., and Soliman, E. A. (2013). Theoretical study of metal-insulator-metal tunneling diode figures of merit. *IEEE Journal of Quantum Electronics*, 49(1):72–79.
- Hegy, B., Csurgay, Á., and Porod, W. (2007). Investigation of the nonlinearity properties of the DC IV characteristics of metal-insulator-metal (MIM) tunnel diodes with double-layer insulators. *Journal of Computational Electronics*, 6(1-3):159–162.
- Herner, S., Weerakkody, A., Belkadi, A., and Moddel, G. (2017). High performance MIIM diode based on cobalt oxide/titanium oxide. *Applied Physics Letters*, 110(22):223901.
- Herner, S. B., Belkadi, A., Weerakkody, A., Pelz, B., and Moddel, G. (2018). Responsivity–resistance relationship in MIIM diodes. *IEEE Journal of Photovoltaics*, 8(2):499–504.

- Hobbs, P. C., Laibowitz, R. B., and Libsch, F. R. (2005). Ni–NiO–Ni tunnel junctions for terahertz and infrared detection. Applied optics, 44(32):6813–6822.
- Hu, Y. and Stapleton, S. (1991). Quantum capacitance of resonant tunneling diodes. Applied physics letters, 58(2):167–169.
- Jayaswal, G., Belkadi, A., Meredov, A., Pelz, B., Moddel, G., and Shamim, A. (2018). Optical rectification through an Al<sub>2</sub>O<sub>3</sub> based mim passive rectenna at 28.3 thz. Materials Today Energy, 7:1–9.
- Joshi, S. (2015). Performance limits of optical rectennas. PhD thesis, University of Colorado at Boulder.
- Joshi, S. and Moddel, G. (2013). Efficiency limits of rectenna solar cells: Theory of broadband photon-assisted tunneling. Applied Physics Letters, 102(8):083901.
- Joshi, S. and Moddel, G. (2015). Private communication. University of Colorado - Boulder.
- Joshi, S. and Moddel, G. (2016). Optical rectenna operation: where maxwell meets einstein. Journal of Physics D: Applied Physics, 49(26):265602.
- Kale, B. M. (1985). Electron tunneling devices in optics. Optical Engineering, 24(2):242267.
- Karbasian, G., McConnell, M. S., George, H., Schneider, L. C., Filmer, M. J., Orlov, A. O., Nazarov, A. N., and Snider, G. L. (2017). Metal-insulator-metal single electron transistors with tunnel barriers prepared by atomic layer deposition. Applied Sciences, 7(3):246.
- Kim, H. S., Liu, W., Chen, G., Chu, C.-W., and Ren, Z. (2015). Relationship between thermoelectric figure of merit and energy conversion efficiency. Proceedings of the National Academy of Sciences, 112(27):8205–8210.
- Kischkat, J., Peters, S., Gruska, B., Semtsiv, M., Chashnikova, M., Klinkmüller, M., Fedosenko, O., Machulik, S., Aleksandrova, A., Monastyrskiy, G., and Flores, Y. (2012). Mid-infrared optical properties of thin films of aluminum oxide, titanium dioxide, silicon dioxide, aluminum nitride, and silicon nitride. Applied optics, 51(28):6789–6798.
- Ma, Y., Hao, Q., Poudel, B., Lan, Y., Yu, B., Wang, D., Chen, G., and Ren, Z. (2008). Enhanced thermoelectric figure-of-merit in p-type nanostructured bismuth antimony tellurium alloys made from elemental chunks. Nano Letters, 8(8):2580–2584.
- Magnasco, M. O. and Stolovitzky, G. (1998). Feynman’s ratchet and pawl. Journal of statistical physics, 93(3-4):615–632.
- Maraghechi, P., Foroughi-Abari, A., Cadien, K., and Elezzabi, A. Y. (2012). Observation of resonant tunneling phenomenon in metal-insulator-insulator-insulator-metal electron tunnel devices. Applied Physics Letters, 100(11):113503.
- Matsumoto, K. (1996). Room temperature operated single electron transistor made by STM/AFM nano-oxidation process. Physica B: Condensed Matter, 227(1-4):92–94.
- McSpadden, J. O. and Chang, K. (1994). A dual polarized circular patch rectifying antenna at 2.45 GHz for microwave power conversion and detection. In 1994 IEEE MTT-S International Microwave Symposium Digest (Cat. No. 94CH3389-4), pages 1749–1752. IEEE.

- Mendez, E. E. and von Klitzing, K. (2012). Physics and applications of quantum wells and superlattices, volume 170. Springer Science & Business Media.
- Mitrovic, I., Weerakkody, A., Sedghi, N., Ralph, J., Hall, S., Dhanak, V., Luo, Z., and Beeby, S. (2018). Controlled modification of resonant tunneling in metal-insulator-insulator-metal structures. Applied Physics Letters, 112(1):012902.
- Moddel, G. (2017a). Private communication.
- Moddel, G. (2017b). Radiating power converter and methods. US Patent 9,581,142.
- Moddel, G. and Grover, S. (2013). Rectenna solar cells, volume 4. Springer.
- Nagae, M. (1972). Response time of metal-insulator-metal tunnel junctions. Japanese Journal of Applied Physics, 11(11):1611.
- NASA (2010). The earth's radiation budget.
- Niu, G., Kim, H.-D., Roelofs, R., Perez, E., Schubert, M. A., Zaumseil, P., Costina, I., and Wenger, C. (2016). Material insights of HfO<sub>2</sub>-based integrated 1-transistor-1-resistor resistive random access memory devices processed by batch atomic layer deposition. Scientific reports, 6:28155.
- Nyquist, H. (1928). Thermal agitation of electric charge in conductors. Physical review, 32(1):110.
- Oliver, B. (1965). Thermal and quantum noise. Proceedings of the IEEE, 53(5):436–454.
- Ono, M., Santhanam, P., Li, W., Zhao, B., and Fan, S. (2019). Experimental demonstration of energy harvesting from the sky using the negative illumination effect of a semiconductor photodiode. Applied Physics Letters, 114(16):161102.
- Palik, E. D. (1998). Handbook of optical constants of solids, volume 3. Academic press.
- Pan, Y., Powell, C. V., Song, A. M., and Balocco, C. (2014). Micro rectennas: Brownian ratchets for thermal-energy harvesting. pages 185–188.
- Pandya, S., Velarde, G., Zhang, L., Wilbur, J. D., Smith, A., Hanrahan, B., Dames, C., and Martin, L. W. (2019). New approach to waste-heat energy harvesting: pyroelectric energy conversion. NPG Asia Materials, 11(1):26.
- Pelz, B. (2018). Traveling-Wave Metal-Insulator-Metal Diodes for Infrared Optical Rectennas. PhD thesis, University of Colorado.
- Pelz, B. (2019). Private communication. University of Colorado - Boulder.
- Pelz, B., Belkadi, A., and Moddel, G. (2018). Avoiding erroneous analysis of mim diode current-voltage characteristics through exponential fitting. Measurement, 120:28–33.
- Pelz, B. and Moddel, G. (2019). Demonstration of distributed capacitance compensation in a metal-insulator-metal infrared rectenna incorporating a traveling-wave diode. Journal of Applied Physics, 125(23):234502.
- Poudel, B., Hao, Q., Ma, Y., Lan, Y., Minnich, A., Yu, B., Yan, X., Wang, D., Muto, A., Vashaee, D., et al. (2008). High-thermoelectric performance of nanostructured bismuth antimony telluride bulk alloys. Science, 320(5876):634–638.

- Quickenden, T. and Mua, Y. (1995). A review of power generation in aqueous thermogalvanic cells. Journal of The Electrochemical Society, 142(11):3985–3994.
- Raman, A. P., Anoma, M. A., Zhu, L., Rephaeli, E., and Fan, S. (2014). Passive radiative cooling below ambient air temperature under direct sunlight. Nature, 515(7528):540.
- Raman, A. P., Li, W., and Fan, S. (2019). Generating light from darkness. Joule.
- Ratcliff, E. L., Meyer, J., Steirer, K. X., Garcia, A., Berry, J. J., Ginley, D. S., Olson, D. C., Kahn, A., and Armstrong, N. R. (2011). Evidence for near-surface NiOOH species in solution-processed NiO<sub>x</sub> selective interlayer materials: impact on energetics and the performance of polymer bulk heterojunction photovoltaics. Chemistry of Materials, 23(22):4988–5000.
- Rattner, A. S. and Garimella, S. (2011). Energy harvesting, reuse and upgrade to reduce primary energy usage in the USA. Energy, 36(10):6172–6183.
- Rohde, R. A. (2007). Image of radiation transmitted by atmosphere using linepak system of calculating absorption spectra from hitran2004 spectroscopic database.
- Rosi, F. (1968). Thermoelectricity and thermoelectric power generation. Solid-State Electronics, 11(9):833–868.
- Rothman, L. S., Jacquemart, D., Barbe, A., Benner, D. C., Birk, M., Brown, L., Carleer, M., Chackerian Jr, C., Chance, K., Coudert, L. e. a., et al. (2005). The hitran 2004 molecular spectroscopic database. Journal of quantitative spectroscopy and radiative transfer, 96(2):139–204.
- Sadakuni, K., Harianto, T., Akinaga, H., and Suemasu, T. (2009). Caf<sub>2</sub>/fe<sub>3</sub>si/caf<sub>2</sub> ferromagnetic resonant tunneling diodes on si (111) by molecular beam epitaxy. Applied Physics Express, 2(6):063006.
- Sanchez, A., Davis Jr, C., Liu, K., and Javan, A. (1978). The MOM tunneling diode: Theoretical estimate of its performance at microwave and infrared frequencies. Journal of Applied Physics, 49(10):5270–5277.
- Santhanam, P. and Fan, S. (2016). Thermal-to-electrical energy conversion by diodes under negative illumination. Physical Review B, 93(16):161410.
- Sarehraz, M., Buckle, K., Weller, T., Stefanakos, E., Bhansali, S., Goswami, Y., and Krishnan, S. (2005). Rectenna developments for solar energy collection. In Conference Record of the Thirty-first IEEE Photovoltaic Specialists Conference, 2005., pages 78–81. IEEE.
- Sherman, B., Heikes, R., and Ure Jr, R. (1960). Calculation of efficiency of thermoelectric devices. Journal of Applied Physics, 31(1):1–16.
- Shih, Y.-T., Su, C.-Y., Tsai, C.-W., and Pan, W. (2014). Thickness and ordering temperature of surface Nio/Ni systems. AIP Advances, 4(2):027117.
- Shockley, W. and Queisser, H. J. (1961). Detailed balance limit of efficiency of p-n junction solar cells. Journal of applied physics, 32(3):510–519.
- Simmons, J. G. (1963). Generalized formula for the electric tunnel effect between similar electrodes separated by a thin insulating film. Journal of applied physics, 34(6):1793–1803.

- Snyder, G. J. and Toberer, E. S. (2011). Complex thermoelectric materials. In materials for sustainable energy: a collection of peer-reviewed research and review articles from Nature Publishing Group, pages 101–110. World Scientific.
- Sokolov, I. (1998). On the energetics of a nonlinear system rectifying thermal fluctuations. EPL (Europhysics Letters), 44(3):278.
- Sumithra, S., Takas, N. J., Misra, D. K., Nolting, W. M., Poudeu, P., and Stokes, K. L. (2011). Enhancement in thermoelectric figure of merit in nanostructured  $\text{Bi}_2\text{Te}_3$  with semimetal nanoinclusions. Advanced Energy Materials, 1(6):1141–1147.
- Tannas, L. E. (1994). Evolution of flat-panel displays. Proceedings of the IEEE, 82(4):499–509.
- Tien, P. and Gordon, J. (1963). Multiphoton process observed in the interaction of microwave fields with the tunneling between superconductor films. Physical Review, 129(2):647.
- Tiwari, B., Bean, J. A., Szakmány, G., Bernstein, G. H., Fay, P., and Porod, W. (2009). Controlled etching and regrowth of tunnel oxide for antenna-coupled metal-oxide-metal diodes. Journal of Vacuum Science & Technology B: Microelectronics and Nanometer Structures Processing, Measurement, and Phenomena, 27(5):2153–2160.
- Trivich, D., Flinn, P., Daniels, F., and Duffie, J. (1955). Maximum efficiency of solar energy conversion by quantum processes.
- Tucker, J. (1979). Quantum limited detection in tunnel junction mixers. IEEE Journal of Quantum Electronics, 15(11):1234–1258.
- Vallée, C., Gonon, P., Jorel, C., El Kamel, F., Mougnot, M., and Jousseume, V. (2009). High  $\kappa$  for MIM and RRAM applications: Impact of the metallic electrode and oxygen vacancies. Microelectronic Engineering, 86(7-9):1774–1776.
- Wang, K., Hu, H., Lu, S., Guo, L., and He, T. (2015). Design of a sector bowtie nano-rectenna for optical power and infrared detection. Frontiers of Physics, 10(5):104101.
- Watanabe, M., Suemasu, T., Muratake, S., and Asada, M. (1993). Negative differential resistance of metal (cosi<sub>2</sub>)/insulator (caf<sub>2</sub>) triple-barrier resonant tunneling diode. Applied physics letters, 62(3):300–302.
- Weerakkody, A., Belkadi, A., and Moddel, G. (2019). Towards a practical  $\text{Al}_2\text{O}_3$ -based metal-insulator-metal infrared rectenna. Under preparation.
- Weerakkody, A., Sedghi, N., Mitrovic, I., Van Zalinge, H., Noureddine, I. N., Hall, S., Wrench, J., Chalker, P., Phillips, L., Treharne, R., and Durose, K. (2015). Enhanced low voltage non-linearity in resonant tunneling metal-insulator-insulator-metal nanostructures. Microelectronic Engineering, 147:298–301.
- Weerakkody, D. (2016). Engineered high-k oxides. PhD thesis, University of Liverpool.
- Weiss, M. D., Eliasson, B. J., and Moddel, G. (2004). Terahertz device integrated antenna for use in resonant and non-resonant modes and method. US Patent 6,835,949.
- Yoo, T.-W. and Chang, K. (1992). Theoretical and experimental development of 10 and 35 ghz rectennas. IEEE Transactions on Microwave Theory and Techniques, 40(6):1259–1266.

Zhai, Y., Ma, Y., David, S. N., Zhao, D., Lou, R., Tan, G., Yang, R., and Yin, X. (2017). Scalable-manufactured randomized glass-polymer hybrid metamaterial for daytime radiative cooling. Science, 355(6329):1062–1066.

Zhu, Z. J. (2014). Graphene geometric diodes for optical rectennas. PhD thesis, University of Colorado.

## APPENDIX A

### EXPONENTIAL FITTING AND SIMULATION PARAMETERS

#### A.1 MIM-1 Diode

For an exponential fit (Pelz et al., 2018),

$$I(V_D) = I_0(e^{bV_D} - e^{-dV_D}) \quad (\text{A.1})$$

the fitting parameters were determined to be  $I_0 = 2.12 \mu\text{A}$ ,  $b = 9.18 \text{ V}^{-1}$  and  $d = 10.2 \text{ V}^{-1}$ .

Table A.1: Parameters used for simulating the diode tunneling characteristics in DC.

Diode	Work function (eV) or electron Affinity (eV)	Thickness (nm)	Effective Mass of electrons
Ni	4.9	35	1
Cr/Au	4.91	3/37	1
NiO	4.78	6 (8 nm nominal thickness from VASE)	0.7

#### A.2 MI<sup>2</sup>M-1 Diode

For an exponential fit (Pelz et al., 2018),

$$I(V_B) = I_0(e^{b(V-I(V)R_s)} - e^{-d(V-I(V)R_s)}) \quad (\text{A.2})$$

the fitting parameters were  $I_0 = 3.63 \mu\text{A}$ ,  $b = 9.82 \text{ V}^{-1}$  and  $d = 10.62 \text{ V}^{-1}$ , where  $R_v(V) = R_s + \alpha V^2$  and  $\alpha = 8.7 \text{ k}\Omega/\text{V}^2$  and  $R_s = 275 \Omega$ .

Table A.2: Parameters used for simulating the diode tunneling characteristics at DC. Changes from the DC fit parameters for high frequency simulation are underlined.

Diode	Work function (eV) or electron affinity (eV)	Thickness (nm)	Effective mass of electrons	Dielectric constant 28 THz
Ni	4.9	35	1	–
Cr/Au	4.7	3/62	1	–
NiO	4.73	3.5 (3.9 nm nominal)	1/ <u>0.5</u>	<u>7</u>
Al <sub>2</sub> O <sub>3</sub>	4.2	0.73 (1.1 nm nominal)	1/ <u>0.5</u>	<u>3.85</u>

### A.3 MI<sup>2</sup>M-2 Diode

For the exponential fit following eq. A.1, the fitting parameters were  $I_0 = 4.05 \mu\text{A}$ ,  $b = 8.05 V^{-1}$  and  $d = 8.8 V^{-1}$ .

Table A.3: Parameters used for simulating the diode tunneling characteristics at DC.

Diode	Work function (eV) or electron affinity (eV)	Thickness (nm)	Effective mass of electrons
Ni	4.85	35	1
Cr/Au	4.7	3/62	1
NiO	4.7	4.1 (4 nm nominal)	0.91
Al <sub>2</sub> O <sub>3</sub>	4.3	1 (1.1 nm nominal)	0.65

### A.4 MI<sup>2</sup>M-3 Diode

For the exponential fit following eq. A.2, the fitting parameters were  $I_0 = 1.92 \mu\text{A}$ ,  $b = 7.45 V^{-1}$  and  $d = 8.16 V^{-1}$ ,  $\alpha = 14.8 \text{ k}\Omega/V^2$  and  $R_s = 1.32 \text{ k}\Omega$ .

### A.5 MI<sup>2</sup>M-4 Diode

For the exponential fit following eq. A.1, the fitting parameters were  $I_0 = 2.69 \mu\text{A}$ ,  $b = 9.07 V^{-1}$  and  $d = 9.56 V^{-1}$ .

### A.6 Cosine squared fitting parameters

The fitting parameters for the cosine squared relationship of  $V_{oc}$  against polarization angle ( $\theta$ ) defined as

$$V_{oc}(\theta) = A_{\parallel} \cos(\theta + \phi)^2 + A_{\perp} \sin(\phi)^2 \quad (\text{A.3})$$

for the diodes discussed in the paper are presented in Table A.4.

Table A.4: Parameters used for fitting fabricated diode's  $V_{oc}$  against polarization angle measured response.  $R^2$  indicates the quality of a fit.

Diode	Cos <sup>2</sup> amplitude ( $A_{\parallel}$ )	Angular shift ( $\phi$ ) ( $^{\circ}$ )	Sin <sup>2</sup> amplitude ( $A_{\perp}$ )	$R^2$
MIM-1	27.8 $\mu\text{V}$	-3.6 $^{\circ}$	522 $n\text{V}$	0.9988
MI <sup>2</sup> M-1	53.9 $\mu\text{V}$	-6.9 $^{\circ}$	1.28 $\mu\text{V}$	0.9972
MI <sup>2</sup> M-2	94.8 $\mu\text{V}$	-11 $^{\circ}$	1.25 $\mu\text{V}$	0.9985
MI <sup>2</sup> M-3	38.2 $\mu\text{V}$	-8.4 $^{\circ}$	653 $n\text{V}$	0.8471
MI <sup>2</sup> M-4	43.9 $\mu\text{V}$	2.3 $^{\circ}$	-203 $n\text{V}$	0.9992

## APPENDIX B

### PUBLICATIONS

- (1) Herner, S., Weerakkody, A., **Belkadi, A.**, and Moddel, G. (2017). High performance MIIM diode based on cobalt oxide/titanium oxide. *Applied Physics Letters*, 110(22):223901.
- (2) Herner, S. B., **Belkadi, A.**, Weerakkody, A., Pelz, B., and Moddel, G. (2018). Responsivity-resistance relationship in MIIM diodes. *IEEE Journal of Photovoltaics*, 8(2), 499-504.
- (3) Pelz, B., **Belkadi, A.**, and Moddel, G. (2018). Avoiding erroneous analysis of MIM diode current-voltage characteristics: Exponential fitting. *Measurement*, 120, 28-33.
- (4) **Belkadi, A.**, Weerakkody, A., and Moddel, G. (2018). Large errors from assuming equivalent dc and high-frequency electrical characteristics in metal-multiple-insulator-metal diodes. *ACS Photonics*, 5(12), 4776-4780.
- (5) Jayaswal, G., **Belkadi, A.**, Meredov, A., Pelz, B., Moddel, G., and Shamim, A. (2018, June). A Zero-Bias, Completely Passive 28 THz Rectenna for Energy Harvesting from Infrared (Waste Heat). In *2018 IEEE/MTT-S International Microwave Symposium-IMS* (pp. 355-358). IEEE.
- (6) Jayaswal, G., **Belkadi, A.**, Meredov, A., Pelz, B., Moddel, G., and Shamim, A. (2018). Optical rectification through an  $\text{Al}_2\text{O}_3$  based MIM passive rectenna at 28.3 THz. *Materials Today Energy*, 7, 1-9.
- (7) Weerakkody, A., **Belkadi, A.**, and Moddel, G. (2019). Towards a practical  $\text{Al}_2\text{O}_3$ -based metalinsulator-metal infrared rectenna. Ready for submission.
- (8) **Belkadi, A.**, Weerakkody, A., and Moddel, G. Demonstration of resonant tunneling effects in metal-double-insulator-metal ( $\text{MI}^2\text{M}$ ) diodes. Ready for submission.